Nano-structures and materials for wafer-scale solar cells

Amna Safdar

Doctor of Philosophy

University of York

Physics

April 2018

Abstract

This thesis addresses two of the main materials for solar cells, namely silicon and the family of halide perovskites. For silicon, light trapping structures are investigated for solar cell applications while perovskite materials are investigated as a gain material for optoelectronic applications. Light trapping allows the capture of photons that might otherwise be lost, especially at the red end of the spectrum where silicon is less absorptive. The key is to enhance the efficiency of silicon cells by thinning down the wafer and reducing the bulk recombination losses and to achieve a higher V_{oc} while maintaining strong light absorption (represented by a high short circuit current, J_{sc}) by applying efficient light trapping schemes. It is still an open question whether nanostructures are beneficial for real devices, especially since highly efficient solar cells employ >100 µm thick absorber materials and use wet etched micron-sized pyramids for light trapping. In this thesis, I conduct a study which compares nanostructures and pyramid microstructures on wafer-based silicon solar cells. This study is important because (1) most light trapping nanostructures are investigated only in the optical regime, while I realize them on silicon devices to analyze both their optical and their electrical character; (2) nanostructures perform better than microstructures in wafer based silicon solar cells, highlighting the effectivity of nanostructures even in wafer-based silicon. Here, the nanostructures comprise wet and dry-etched quasi-random structres and they are compared with pyramidal microstructures. A photocurrent as high as 38 mA/cm^2 for a dry etched quasirandom nanostructure is attained experimentally, which is 3.2 mA/cm^2 higher than wet etched pyramids fabricated in the same batch. The other material which is now becoming very popular in the solar cell community is the family of metal halide perovskite materials that are increasingly attracting the attention of optoelectronics researchers, both for solar cell and for light emission applications. The ultimate is in simplicity, however, is to observe lasing from a continuous thin film, which has not been aimed before. Here, I show perovskite random lasers; they are deposited at room temperature on unpatterned glass substrates and they exhibit a minimum threshold value of 10 $\mu J/cm^2$. A rather special feature is that some of the films exhibit single and dual mode lasing action, which is rarely observed in random lasers. This work fully exploits the simplicity of the solution-based process and thereby adds an important capability to the emerging field of perovskite-based light emitters.

Publications arising from this work

- Amna Safdar, Yue Wang and Thomas F. Krauss, “Random lasing from unstructured perovskite thin films,’’ The Semiconductor and Integrated Opto-Electronics (SIOE) Conference, Cardiff, April 2017 (Oral presentation)
- Amna Safdar, Yue Wang and Thomas F. Krauss “Random lasing in uniform perovskite thin films,’’ Optics Express, 26(7): 6623–6630, November 2017 (Journal Publication)
- Amna Safdar, Yue Wang, Juntao Li, Yujie Chen, Dingyong Zhong, Thomas F. Krauss, “Organic-Inorganic perovskite film fabrication and application in solar and laser devices’’. The 12th international symposium on Photonics and Electromagnetic Crystal Structures (PECS), York July 2015 (Poster)
- Amna Safdar, Thomas Krauss, “Solar cell fabrication with novel materials.’’ Department of Physics Postgraduate Conference, York August 2015 (Oral presentation & poster)
- Aman Safdar, Yue Wang, Christopher Reardon, Emiliano R. Martins, Juntao Li, and Thomas F. Krauss “Nanostructures outperform pyramids in 180 μm thick silicon solar cells’’ ACS nano (paper under review)
- Amna Safdar, Yue Wang, Christopher Reardon, Thomas F. Krauss, “Quasi-random light trapping structures fabrication and application to silicon solar devices’’. European Materials Research Society (EMRS) Fall meeting, Warsaw, Poland, September 2017 (Oral presentation)
- Amna Safdar, Photovoltaic systems summer school (PVSSS), Delft University of Technology (Delft, the Netherlands) attended, with presentation and practical given (July 2017)

Contents

Declaration of Authorship

I declare that this thesis titled, “Nano-structures and materials for wafer- scale solar cells’’

is a presentation of original work and I am the sole author.

I hereby declare that:

- I, Amna Safdar, hereby certify that this thesis, which is approximately 40000 words in length, has been written by me, that no part of this thesis is concurrently presented in candidature for any degree other than Doctor of Philosophy at the University of York.
- This work has not previously been presented for an award at this, or any other, University.
- The work presented in it are my own unless stated otherwise.
- I have acknowledged all sources as References.

Acknowledgements

Thomas, an inspiration to young researchers, thank you for your significant contribution to my journey of development both in *science* and *life*.

I would like to start with my gratitude to my supervisor Prof. Thomas F. Krauss for his constant support and guidance over the years. I feel blessed to have had him as my advisor and cannot put into words his constructive contribution to my PhD and in my development as an independent researcher. Never minding how busy he was in both his domestic and international travels for his scientific activities, he always found time for me for regular meetings. I deeply admire his in-time critical feedback, both verbal and written over the years. His enthusiastic loud behaviour always kept me motivated in my research hardships and the freedom he gave me to explore on my own. Also, I am thankful for his generosity in funding the unfunded period of my studies.

I would like to offer my sincere thanks to Prof. Matt Probert and Dr Andrew Pratt, Thesis Advisory Panel members for their guidance and review over all formal matters of this journey. I would also like to thank Dr Vlado Lazarov and Dr Emiliano Martins for their time and consideration on reviewing my dissertation. I would also like to thank Dr. Olindo Isabella for his brief but precise suggestions in Delft, Netherlands.

I would like to acknowledge the prestigious National university of sciences and technology (NUST), Pakistan; my 1st sponsor, for the studentship award under the grant of FDP, 2014 program. I would like to thank my current Department of Physics, University of York for the studentship award and of course, to my supervisor who generously funded the extended six months.

I would like to thank the Photonics group members for always being helpful and supportive. A sincere thanks to Dr Yue Wang for her significant and consistent support of my experiments. I have truly been benefited by your experience and expertise. Many thanks to Dr

Christopher Reardon for his all assistance regarding equipment and facilities in particular. Thanks to Dr Kezheng Li for his help in many ways. A special thanks to Dr Annett Klemm and Dr Matthias Fischer, both past group members of the Photonics group for their support when I first arrived in York. I am grateful to the technical team members Charan Panesar and Jonathan Cremer from supporting the measurements lab Z011 in the Electronics Engineering Department; for their welcoming attitude to my use of their equipment. Many thanks to Dr Emiliano Martins and Dr Juntao Li for their productive collaborations in the course of my study. Thanks to Dr Sarah Farrukh for her support which made it that much easier for me to initiate this journey.

A special thanks to M. A, for the precious positive energy unknowingly you provided not only in PhD duration but since the beginning. The most important thing we had in common; we both wanted to see a "stronger me", thanks for the never ending encouraging words.

I am grateful to my family for their contribution over the years of my studies. Most of all, I would like to take this opportunity to express my deepest and most heartfelt thanks to my mother who has been my motivation to become an independent individual. Her unconditional effort and support throughout the years of her life, for her unfailing love. Words are not enough to express my thanks to you, I love you Ami jan. Thanks, to her with pride.

Many Thanks to all of you.

For my love, my mother, *Jamila Parveen*.

1 Chapter 1: Basics of solar cells

Why PV technology?

Over the past decades, an extensive growth has occurred in the demand for energy. The main reason for this development has been the urbanization of mankind which has led to improved living standards with industrial infrastructures, high electricity demand and increased transport. These technologies all impact on the environment, with global warming based on increased carbon emissions being a key concern. To minimise the impact of global warming, clean energy generation is a key requirement that drives the expansion of research in the field of photovoltaic technology which converts solar energy into electricity.

Using Photovoltaic (PV) technology is arguably the most promising way to harvest solar energy and to satisfy current and future clean energy demands without generating carbon dioxide emissions. The main building block of any photovoltaic technology is a solar cell. Many cells are connected together to form a panel. Solar panels can be installed onto the roofs to produce energy for individuals for their personal needs. Zero energy buildings can be built that operate independent by the electricity market by using decentralized solar panels. Many panels can put together forming solar thermal parks and solar farms on a large scale.

How does PV compare to the other renewable energy sources e.g. nuclear, hydro and wind?
To answer this, we note that the growth of solar energy installations can be much faster compared to nuclear and hydro, as these require larger scale centralized technologies; big dams and power plants are needed which require significant investments, while PV can be installed as decentralized roof technology. An additional argument is that the sun is the primary energy source on earth and is available in abundance. Hydro and wind are secondary sources produced by the temperature differences on earth, but ultimately driven by the sun.

In the following chapter, the physics of solar cells is discussed in detail. First, I introduce semiconductor materials that form the building block of a solar cell based on their energy band structure. The fundamentals of energy band alignment and charge carrier transport mechanism is discussed using the example of a silicon pn-diode. The silicon solar cell has characteristic response to the solar spectrum in terms of photon absorption, charge carrier generation and recombination processes. The IV- characteristic curve under illumination is discussed the figures of merit of a solar cell, that is, the open-circuit voltage, the short-circuit current density, the fill factor, the power conversion efficiency and the internal and external collection efficiency. Efficiency limiting factors, such as the recombination rate and parasitic resistance effects are also briefly discussed.

1.1 Material classification

Semiconductors are the most common materials used to make solar devices. A key characteristic of semiconductor materials is the fact that the energy levels of their valence electrons and their conduction electrons are separated by an energy band-gap, typically of order 1 eV for solar cell materials. In contrast to semiconductors, highly conductive materials do not exhibit such a bandgap and as such, do not require the addition of energy to move from the valence band (VB) to the conduction band (CB), so they always have free electrons available for electrical conduction. Thirdly, insulators are characterised by very large bandgaps (typically several eV), which means that there are very few conduction electrons available at room temperature. The energy band diagram for three types of materials is described in Figure 1.1 where Fermi level indicates that all the available states above it are empty and all the states below are occupied at absolute zero temperature.

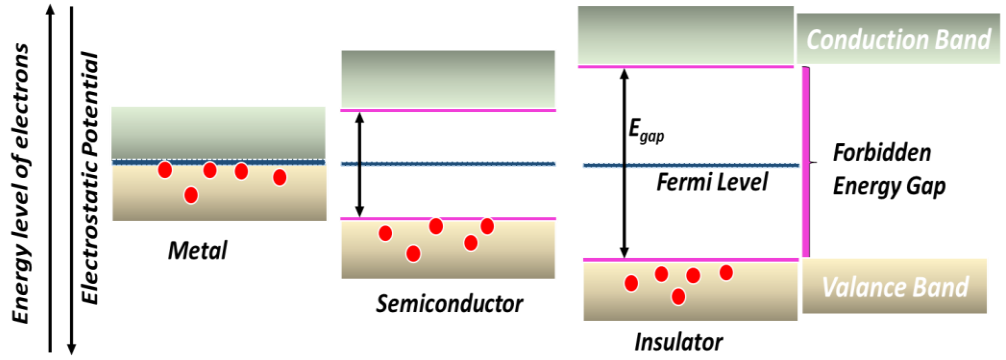

Figure 1.1. Classification of materials based on band-gap energy. Physics behind the realization of solar cell.

In semiconductor materials, because of their moderate bandgap energy, electrons can be excited into the conduction band by applying thermal or optical energy. When a photon of an energy greater than the bandgap is absorbed, the electron is promoted to the conduction band and an electron-hole pair is generated. This e-h hole pair is then collected to generate electricity. The most commonly used semiconductor material in solar cells is silicon because of its stability, abundance, and favourable bandgap energy of 1.12 eV (the discussion of the Shockley-Queisser limit in section 1.5 explains why this bandgap is favourable). The generation of an electrical voltage under illumination of a silicon rod was first noticed by Russel Ohl [1939][1] in a purifying process of silicon where n and p-type impurities solidify during recrystallization within multi-silicon ingots and formed localized junction points. Details can be found in the patent reference filed by Ohl. (US Patent 2402662) [2] After the advances in transistor devices invented in 1940, the Bell laboratory also has the credit to the first commercial use of this effect in solar technology, in 1954 for the space applications. [3] Chapin, Pearson and Fuller, three scientists from Bell Laboratories, published 1st formal PV device with 6% efficiency in the Journal of Applied Physics and this device was the extension of Ohl's device with 1%.[4]

Silicon is a group IV element and with a bandgap of 1.12 eV. The upper band is typically referred to as the conduction band (CB) and the lower as the valence band (VB). Intrinsic

silicon behaves as an insulator at room temperature, because the thermal energy is not sufficient to promote electrons into the CB. In general, the free charge carrier density obeys the equality

$$n_\circ = p_\circ = n_i \tag{1.1}$$

hereby n_o is the electron carrier concentration, p_o is the hole carrier concentration and n_i is the intrinsic carrier concentration. The product of n_o and p_o is given by:

$$n_\circ . p_\circ = n_i^2 \tag{1.2}$$

The probability of these states to be occupied by a free carrier is determined by the Fermi-Dirac distribution.

$$f(E) = \frac{1}{1 + e^{\frac{(E - E_f)}{k_B T}}} \tag{1.3}$$

where E_f represents the Fermi level, T (K) is the temperature and k_B is the Boltzmann constant. At T= 0, the Fermi function is a step-like function, indicating that all the states above the Fermi level are empty and all the states below it is occupied. At higher temperatures (T > 0 K), some of the carriers are thermally excited and can occupy higher energy states. The carrier concentration at equilibrium is given

$$n_\circ = N_C e^{\frac{(E_f - E_C)}{k_B T}} \tag{1.4}$$

$$p_\circ = N_V e^{\frac{(E_V - E_F)}{k_B T}} \tag{1.5}$$

$$p_\circ n_\circ = N_C N_V e^{\frac{-E_G}{2 k_B T}} \tag{1.6}$$

The product in equation 1.6, depends only on the bandgap and temperature.

The free carrier concentration in crystalline silicon can be modified by intentionally introducing impurities. For example, by introducing a group V donor element, additional energy levels are introduced below the CB, which are ionised at room temperature, thereby

increasing the free electron concentration (n-type) doping. Conversely, a group III acceptor impurity introduce energy levels just above the VB and increases the hole concentration (p-type).

Assuming that all the dopant impurities are ionized, for n-type $n_o \approx N_D$ and using the equality equation $n_i^2 = p_o n_o$, we can write following expression to determine the minority carrier concentration (holes) as $p_o = \frac{n_i^2}{N_D}$. In thermal equilibrium, by taking the ionized donor N_A and N_D acceptor impurities into account, the free carrier density can be determined via the Fermi function and we can express the Fermi energy as follows:

For n-type:

$$E_f = E_i + k_B T \ln\left(\frac{N_D}{n_i}\right) \tag{1.7}$$

For p-type:

$$E_f = E_i - k_B T \ln\left(\frac{N_A}{n_i}\right) \tag{1.8}$$

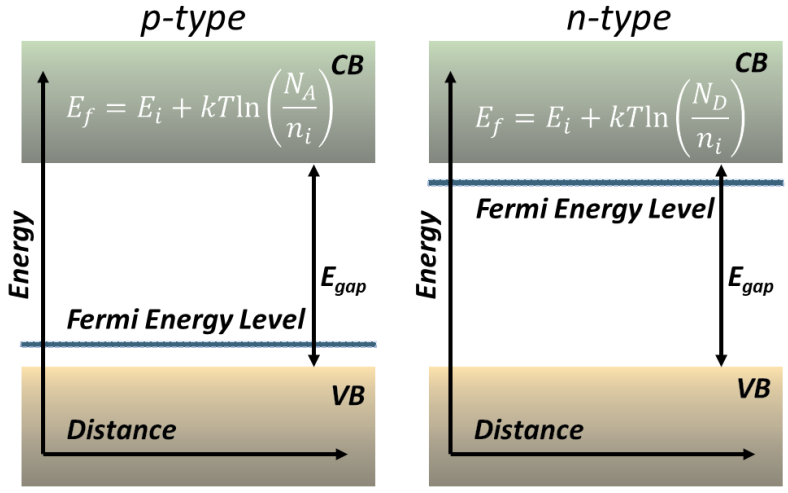

Figure 1.2. Band diagram for p- and n-type silicon together with the illustration of the Fermi energy level positioning.

According to these equations, the Fermi energy level positions are close to the VB edge in p-type and close to CB edge in the n-type semiconductor material. The band diagram for n-type and p-type silicon together with the E_f position dependence is shown in Figure 1.2.

1.1.1 Energy band alignment for the formation of a silicon diode structure

The silicon solar cell is a two-terminal device, i.e. a diode that generates voltage via the photovoltaic effect when illuminated. The device is a basic semiconductor diode which conducts current preferentially in one direction when an external voltage is applied. A diode is a p-n junction is made by creating p-type and n-type doped regions in the silicon. In thermal equilibrium, the pn- junction potential is constant and hence the Fermi level is aligned across the junction. The resulting band diagram and charge distributions are shown as a function of distance across the metallurgically formed junction in Figure 1.3 (a). The junction potential, also referred to as the "in-built" voltage V_{bi}, is created by the concentration gradient between the p- and n-type regions. This concentration gradient drives a diffusion flow of electrons to the p-doped region and holes to the n-doped region, thus establishing an equal and opposite charge on either side of the junction and creating a space-charge region in the device. This charge density (ρ) creates an electric field which is shown in Figure 1.3 (b), (c). This built-in electric field opposes the diffusion flow and stops it in equilibrium.

The potential difference across the junction V_{bi} is the difference between the Fermi energies in the doped regions. We can write an expression for the built-in potential as follow:

$$eV_{bi} = E_f^n - E_f^p = E_g - k_B T \ln\left(\frac{N_C}{n_\circ}\right) - k_B T \ln\left(\frac{N_V}{p_\circ}\right) \tag{1.9}$$

$$eV_{bi} \approx k_B T \ln\left(\frac{N_A N_D}{n_i^2}\right) \tag{1.10}$$

The above equation determines the built-in potential of a pn- junction formed in a semiconductor, by knowing the dopant concentration and the intrinsic carrier concentration.

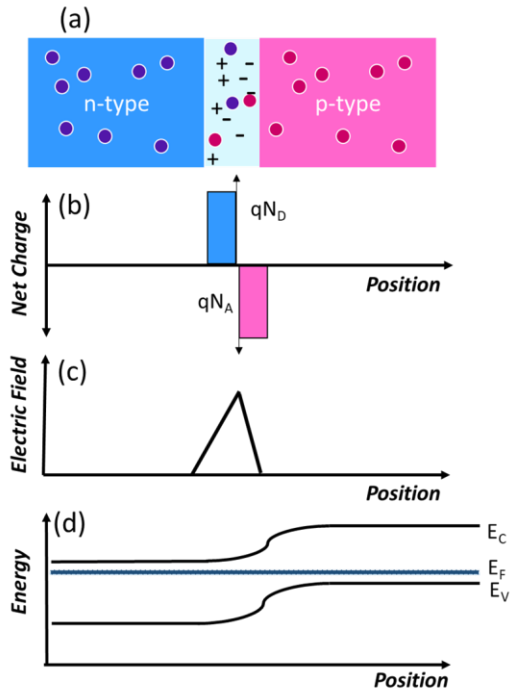

Figure 1.3. Diagram represents (a) A metallurgical junction formed by combining n- and p-type silicon. (b) Abrupt doping density distribution across the junction. (c) the electric field formation in the depletion region. (d) pn- junction band alignment diagram.

For example, silicon wafer is doped with a background acceptor concentration (p-type) of 10^{16} cm^{-3} and I doped it with a donor concentration (n-type) of 10^{19} cm^{-3} at the front surface to form an emitter layer of thickness 1 µm. Typically, for Si at 300 K, the intrinsic carrier concentration is $1.5x10^{10}$ cm^{-3}. By assuming that the formed junction is abrupt (step like) and all the doped atoms are ionized; equation 1.10 allows us to calculate the built-in voltage across the junction, for the material doping concentrations, V_{bi}=0.81 V. More details about equation 1.11 can be found in reference [5].

1.1.2 Carriers transport mechanisms under biased condition

When an external voltage is applied across the p-n junction, the junction exhibits a rectifying behaviour. Under reverse bias, when the positive terminal connects at the n-side and the negative terminal connects at the p-side, a small drift current flows. This drift current occurs because the applied bias disturbs the diffusion equilibrium and charge carriers are attracted towards the opposite terminal polarities. The drift current density is described as follows:

For hole charge carriers:

$$J_h^{drift} = q\mu_h \rho \xi \tag{1.11}$$

For electron charge carriers:

$$J_e^{drift} = -q\mu_e \rho \xi \tag{1.12}$$

μ is the charge carrier mobility parameter and ξ the magnitude of the electric field. The drift current density J_e^{drift} is therefore given by the product of charge carrier density (ρ), the mobility, the electric field and the charge.

As these carriers leave ionized atoms behind, the space charge region gets wider. The effect of reverse bias on the space charge region is shown in Figure 1.4 (b). Under reverse bias, a small drift current flows. Conversely, under forward bias in Figure 1.4 (c), charge carriers start to flow into the space charge region. Initially, the size of the space-charge region reduces; when the applied voltage approaches the built-in voltage, a large diffusion current is built-up. The characteristic current-voltage (I-V) curve can easily be calculated under dark condition and is known as the Shockley equation. The derivation assumes that generation and recombination rates are negligible in the space charge region and that the depletion region is abrupt with boundaries x_n and x_p, as shown in the charge distribution Figure 1.3 (b).

Hence, we can select the boundaries of the space-charge region to calculate a current. In the space-charge, only the diffusive flow of minority carriers (say electrons) is considered in the majority charge (p-type) region. The resulting diffusion current density is then described as follows:

$$J_e(x) = (-e) D \frac{dn}{dx} \tag{1.13}$$

Similarly, for holes as minority carriers, the diffusion current in the n-type region is given by:

$$J_h(x) = (+e) D \frac{dp}{dx} \tag{1.14}$$

The sum of electron diffusion into the p-region and hole diffusion into the n-region delivers the Shockley equation (also called, diode equation):

$$J = J_h + J_e = J_\circ \left(e^{\frac{qV}{k_B T}} - 1 \right) \tag{1.15}$$

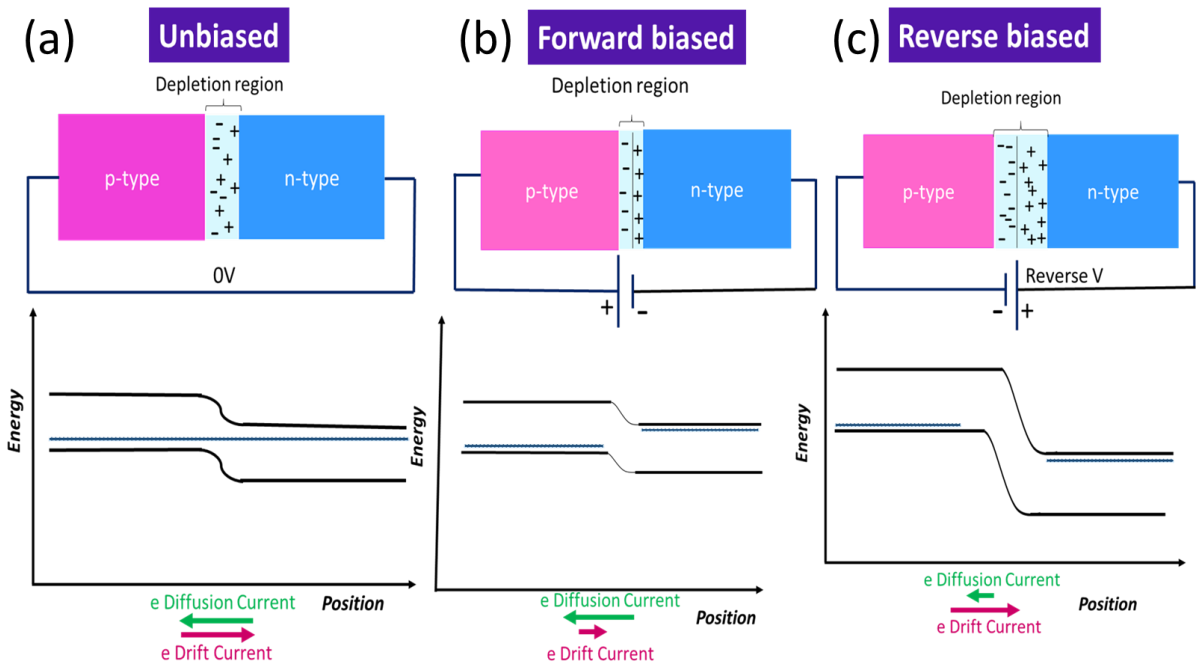

Figure 1.4. pn- junction under unbiased, reverse biased and forward biased conditions, representing the effect on depletion region depth and the alignment of energy bands.

Here, J_o is the reverse saturation current density of the diode due to the drift current from minority charge carriers and V is the applied potential across the device, with k_B the Boltzmann constant and T the temperature.

1.2 Solar spectrum

Photovoltaic technology can harvest sunlight by converting the sun's energy directly into electricity. An alternative way to capture sunlight would be to rely on plants, who use chlorophyll to capture the sunlight and convert it into chemical energy. In the process, plants also consume CO_2 and emit O_2, thereby counteracting the imbalance created by the human

consumption of fossil fuels. In fact, the fossil fuel energy sources that currently meet our daily energy demands were formed by the growth and decay of plants which are driven by the sun. Solar energy is clearly the key factor for our survival on earth.

The sun's energy is commonly represented as a function of the wavelength of light. The solar spectrum of energy is well approximated by assuming it as a perfect black body. A black body is defined as an ideal body that completely absorbs incident light at every wavelength with zero reflection or transmittance losses, i.e. $\alpha(\lambda)= 1$ at every wavelength. A black body can be considered as a black box with a small hole in it that is non-reflecting. The emission spectrum is temperature dependent and it obeys Planck's radiation law. The emission spectrum from the sun is characterized as a black body of temperature 6000 K. As the sunlight reaches the surface of the earth, it has to pass through the earth's atmosphere; sunlight, except at the equator, is also collected from an inclined surface. These effects are included in "air mass". For example, the solar spectrum at the outer boundary of the earth's atmosphere is referred to as an ''air mass zero'', or AM0 spectrum. The integrated power density of this spectrum is 1366.1 W/m^2.

The air mass (AM) is then defined as:

$$AM = \frac{1}{\cos\theta} \tag{1.16}$$

where θ is the angle of incidence, measured to the vertical, so the inclination. In this context, AM is described as a ratio of the actual path length of a sun ray through the earth atmosphere to the path length of perpendicularly incident light. Hence, the spectrum of sunray incident directly perpendicular to the earth's outer boundary and crossed through the atmosphere is defined as AM1 whereas AM0 is the spectrum of sunray perpendicular to the earth's surface but at the entry point of the atmosphere without crossing through to the earth's outer boundary. For a solar device characterization, the standard spectrum used is AM1.5, at an incident angle of 48^o. The integrated power density over this spectrum is 1000 W/m^2=100

mW/cm^2. This number describes the maximum available irradiance. Clearly, for power generation purposes, we need to average over the daily and the yearly cycles, which yields much lower numbers. For example, in Germany, an average power density of approximately 1700 kWh/m^2 per annum is available [6]. In a very sunny desert area, however, such as in Saudi Arabia, this value almost doubles to [2200 kWh/m^2].[7] The average power density at Bisha in Saudi Arabia is ~ 8.004 kWh/m^2/day, which gives 2920 kWh/m^2 per annum [8] whereas in death valley, California, this number is 7.80 kWh/m^2/day) [2840 kWh/m^2 per annum].[9] The AM1.5 spectrum can be further classified into AM1.5G (1000 W/m^2) and AM1.5D (900 W/m^2), whereby AM 1.5G is relevant for solar panel devices and includes both direct and diffused light, while AM1.5D describes only the direct sunlight relevant for concentrated solar devices. All three spectra are shown in Figure 1.5.[10][11]

These spectra show additional minima, particularly in the infrared wavelength range, due to absorption by different gas molecules in the atmosphere, particularly water vapour. Also, the ultraviolet part of the spectrum is filtered out by the ozone layer which acts as a shield for high-energy photons.

1.3 Steps in utilization of the solar spectrum by the solar cell

The conversion of solar energy into electrical energy by a photovoltaic device can be described by the following steps:

(a) Photon absorption by the active material layer

(b) Absorbed photon generates charge carriers, i.e. electron-hole pairs.

(c) Charge carriers diffuse to the junction.

(d) Separation of charge carriers at the junction by drift current

(e) The collection at the respective contacts., i.e. holes at the anode and electrons at the cathode. These steps are shown in Figure 1.6.

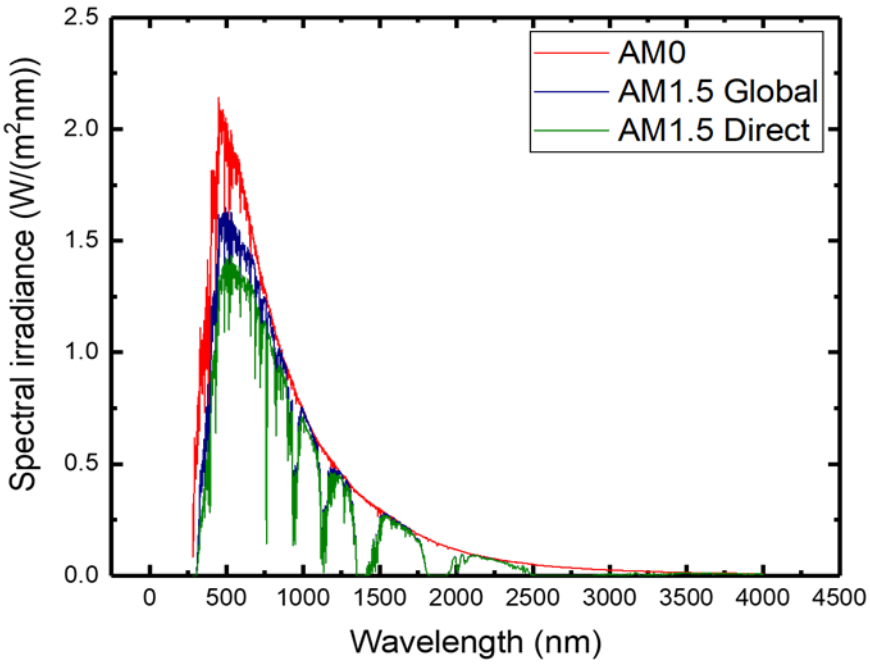

Figure 1.5. Reference solar irradiance spectrum.[12]

1.3.1 Absorption and carrier generation

Sunlight is an electromagnetic radiation which consists of wave packets called photons that carry energy. The particle character of photons related to their wavelength is described by the following simple equation, which states the wave-particle duality of sunlight:

$$E_{\lambda} = \frac{hc}{\lambda} \tag{1.17}$$

where h is Planck's constant c is the speed of light in vacuum.

As the light is absorbed as it penetrates into the material, its intensity decreases as a function of the thickness x, as shown in Figure 1.7 (a) described by the Beer-Lambert law:

$$I(x) = I_{\circ}.e^{-\alpha x} \tag{1.18}$$

I_o is the incident intensity of light and α the absorption coefficient.

The absorption coefficient depends on wavelength and is very specific for each material. The absorption coefficient[13] for silicon is shown in Figure 1.7 (b). The absorption coefficient as a function of wavelength for a given photon energy, $h\nu$, is proportional to the product of the

transition probability, P_{12}, of an electron from an initial energy level E_1 to the final energy level E_2 and the available density of states.

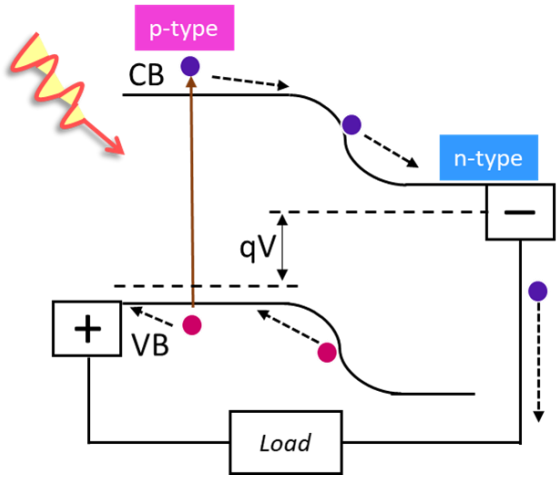

Figure 1.6. A solar cell energy band diagram represents the utilization of sunlight by absorption, charge- carrier generation and collection mechanisms.

Assuming that all the valence-band states are full and all the conduction-band states are empty, the absorption coefficient is given by a sum over all the possible transitions between the available density states if $E_2 - E_1 \geq h\nu$,

$$\alpha(h\nu) \propto P_{12} g_V(E_1) g_C(E_2) \tag{1.19}$$

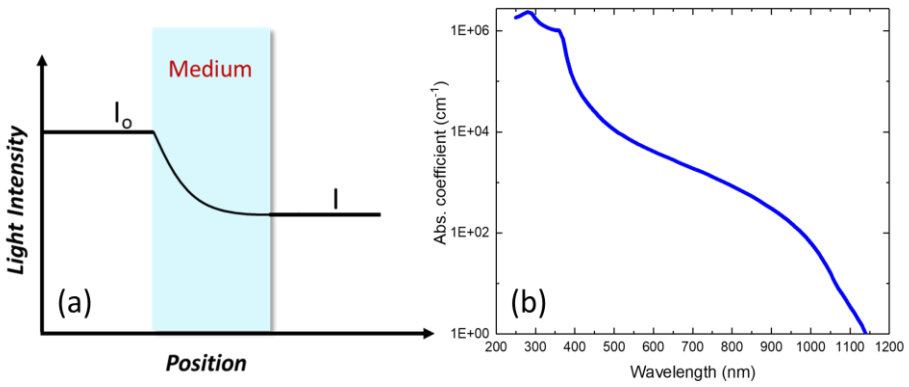

Figure 1.7. Photon absorption through a medium as a function of thickness following the Beer-lambert law (b)The absorption coefficient spectrum for indirect energy bandgap of silicon (cm-1) as a function of wavelength.

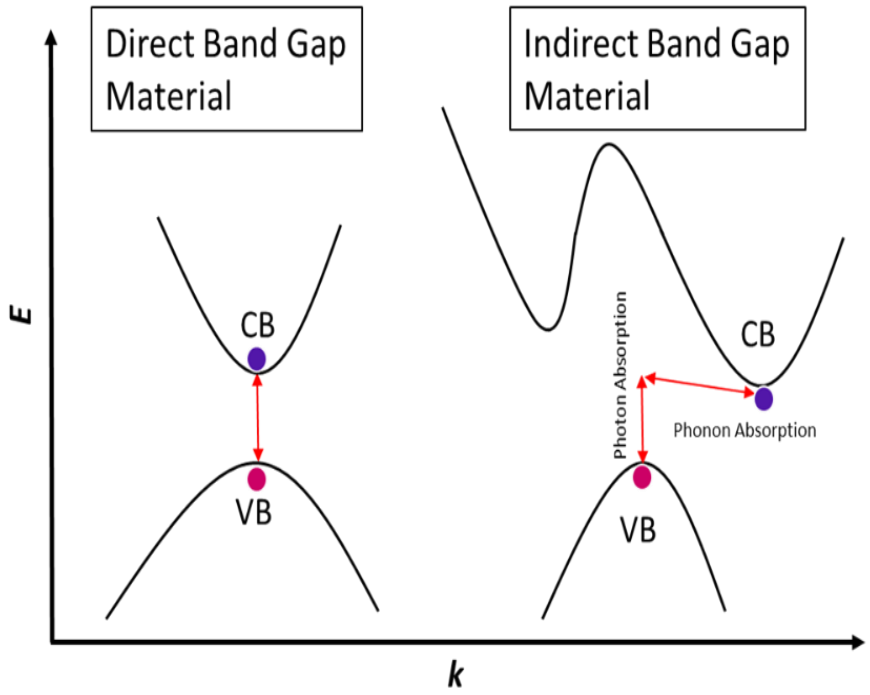

Figure 1.8. An electron transition from VB to CB is shown in Direct and Indirect band gap semiconductor materials.

In the fundamental absorption process, both momentum and energy must be conserved. For example, in Figure 1.8, electron transition from VB to CB is illustrated in both direct band gap and indirect band gap semiconductors. In a direct bandgap semiconductor such as GaAs, the crystal momentum of the initial state is the same as the final state, $P_1 \approx P_2 = P$ In indirect bandgap semiconductor such as Si, the conduction-band minimum and valence band maximum occur at a different crystal momentum, so additional momentum is required to facilitate the transition.

Because photons have very little momentum, momentum conservation necessitates involving another particle, typically a phonon. A phonon is a quantum of crystal lattice vibration; it has low energy but large momentum and must be emitted or absorbed to conserve momentum in the absorption process. The need for involving both a phonon and a photon in the indirect transition is the reason that the absorption coefficient of indirect band gap materials increases slowly as the wavelength gets lower. than that of direct bandgap semiconductor materials as

illustrated in Figure 1.8. It is important to note that absorption in indirect bandgap semiconductor materials can also take place without phonon assistance but only if the photon energy is high enough (in Si, 3.3 eV) to excite an electron carrier directly.

Once the light has been absorbed and the electron-hole pairs have been created, they may either diffuse to the depletion region and get separated under the influence of the built-in field and generate the desired photo-generated current flow, or they may recombine in the material or at a surface and generate heat.

1.3.2 Recombination Processes

Once a photon has been absorbed and created an electron-hole pair, the thermal equilibrium is disturbed and so the $n_o.p_o = n_i^2$ relationship is no longer valid. Instead it is replaced by the $n.p > n_i^2$ inequality. When the photon flux stops, the excess carriers recombine to recover the equilibrium state again.[14] These recombination processes depend on the type of material and strongly determine the output performance of solar cell. Three fundamental processes are responsible for recombination in solar devices and are schematically shown in Figure 1.9. Recombination losses are typically measured in terms of minority carrier lifetime and are defined as the amount of time that a photo-generated charge carrier can survive in its excited state before recombining. The lifetime is expressed as follows:

$$\tau = \frac{\triangle n}{R} = \frac{excess\ minority\ carrier\ concentration}{Volumetric\ recombination\ rate\ (U)} \qquad (1.20)$$

where ''U'' volumetric recombination rate ($sec^{-1}.\ cm^{-3}$) accounts for all type of losses in a solar cell. Δn (cm^{-3}) accounts for both hole and electron charge carrier densities under the assumption that Δn ≈ Δp in quasi-neutral regions.

The lifetime of a minority carrier τ can also be expressed in terms of all recombination mechanisms as follows:[15]

$$R_{Total} = R_{Radiative} + R_{SRH} + R_{Auger}$$

$$\frac{1}{\tau_{Total}} = \frac{1}{\tau_{radiative}} + \frac{1}{\tau_{SRH}} + \frac{1}{\tau_{Auger}} \quad (1.21)$$

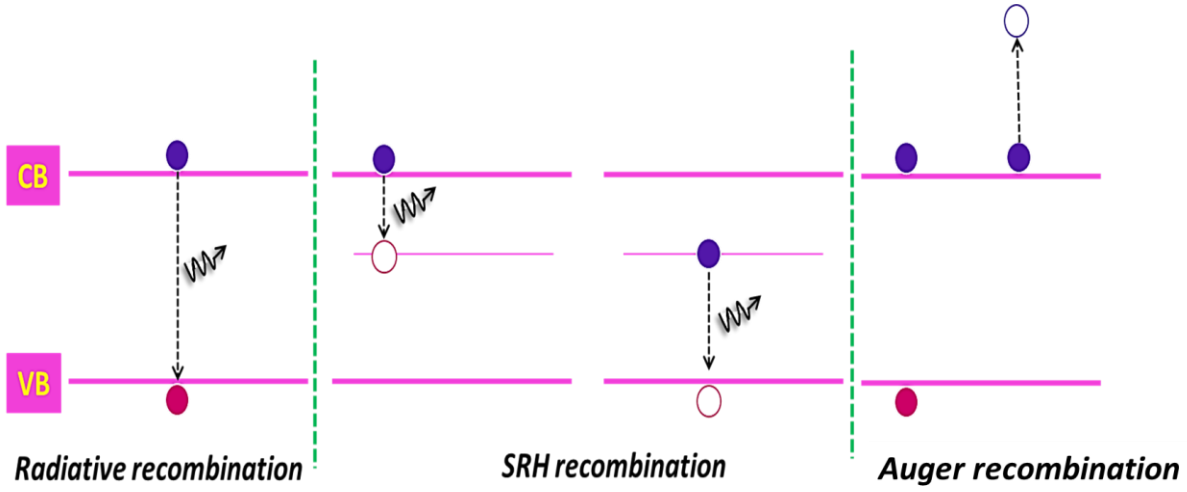

Figure 1.9. Schematic representation of recombination mechanisms occurs in silicon solar cell. Left: Radiative recombination is an inverse process of absorption, commonly occur indirect bandgap semiconductor material. Centre: SRH recombination mechanism happens when defect densities lie between the bandgap energy.

where, $\tau_{radiative}$, τ_{SRH} and τ_{Auger} are the minority carrier lifetime associated to the radiative, Shockley-Read-Hall (SRH) and Auger recombination mechanisms respectively. Here, two recombination processes (bulk) are intrinsic while SRH (extrinsic) dominates when the bulk recombination losses are reduced by using thin high-quality material substrates. SRH relates to the defect density associated to the surface.

These recombination mechanisms are now briefly discussed:

1.3.2.1 Radiative (Direct) recombination

This process mainly occurs in direct band-gap materials as it is a band-to-band process. It describes the relaxation of an excited electron from the conduction band the valence band with the emission of a photon. As silicon is an indirect bandgap material, the probability of direct recombination is very low. The radiative recombination rate is expressed as follows[15]:

$$R_{radiative} = C(np - n_{\circ} p_{\circ}) \quad (1.22)$$

where C (cm^3s^{-1}) is the radiative recombination coefficient and np is the volumetric concentration of charge carrier densities. For silicon, C value is determined by different groups as minimum as 0.95 x 10^{-15} cm^3s^{-1} and maximum as 6 x 10^{-15} cm^3s^{-1}. [16] Dependence of C as a function of temperature is determined varying from 3.7 x 10^{-14} cm^3s^{-1} (T=90 K) to 4.7 x 10^{-15} cm^3s^{-1} (T=300 K).[17] These determined values are lower in silicon due to its intrinsic indirect band gap nature compared to the iii-V semiconductors (10^{-11} -10^{-9}). [18]

For n-type, under the low injection condition where, we can write an expression for $\tau_{radiative}$ as follow:

$$R_{radiative} = Cn_{\circ}(p - p_{\circ}) \quad (1.23)$$

$$T_{ptype,radiative} = \frac{1}{Cn_{\circ}}$$

$$T_{ntype,radiative} = \frac{1}{Cp_{\circ}}$$

In p-type Si, with a given hole density $n_{\circ}$ = 10^{16} cm^{-3}, the lifetime of minority carriers (electrons) can be calculated as 0.03 sec where C= 3x10^{-15} cm^3s^{-1}.

1.3.2.2 Auger recombination

This loss mechanism involves three particles, in contrast to the previously described recombination mechanisms, where only two particles are involved. In Auger recombination, the energy of the recombining carriers is transferred to a third particle rather than emitting a photon. If the third particle is an electron, this electron is excited to a higher level in the conduction band and then relaxes back to the band edge by thermalising its energy. Similar is the case for hole, which is excited to the deep level in the valence band and relax back to the band edge by transferring energy to the lattice vibration which is dissipated in form of heat. Auger recombination depends on the doping concentration and is the dominant recombination mechanism in high-quality silicon.[19][20]

For electron-electron-hole (eeh) 3-particle case, the recombination rate is given by[15]:

$$R_{eeh} = C_n n^2 p \tag{1.24}$$

For hole-hole-electron (hhe) 3-particle case

$$R_{hhe} = C_p n p^2 \tag{1.25}$$

By adding these together:

$$R_{Auger} = C_n n^2 p + C_p n p^2 \tag{1.26}$$

(a) Under the assumption of **low-injection** ($\Delta n << n$) and strongly doped n-type silicon, we can approximate n to N_{donor} (and similarly in the case of p-type silicon) with a dopant concentration $N_{acceptor}$. In this case, we can write:

$$R_{n,Auger} = C_n N_{Donor}^2 p \tag{1.27}$$
$$R_{p,Augur} = C_p n N_{Acceptor}^2$$

and therefore:

$$\tau_{n,Auger} = \frac{1}{C_n N_{Donor}^2} \tag{1.28}$$
$$\tau_{p,Augur} = \frac{1}{C_p N_{Acceptor}^2}$$

The Auger recombination rate is proportional to the square of the doping concentration. As the Auger recombination rate is strongly depends on the doping concentration, so Auger recombination is unavoidable in doped silicon (highly doped emitter).

(b) Under **high injection** condition $(\Delta n = n - n_o = p - p_o)$

We can write,

$$\tau_{n,Auger} = \frac{1}{(C_n + C_h)\Delta n^2} \tag{1.29}$$

In silicon, $C_e \approx C_n \approx$ 1x10^{-30} cm^6/sec. For a given $\Delta n = 10^{18}$ cm^{-3} and $\Delta n = 10^{16}$ cm^{-3} concentrations, the lifetime under Auger recombination is 1 μs and 10 ms respectively.

1.3.2.3 Shockley-Read-Hall recombination

This recombination process occurs via defects that generate states in the band gap of the material. These states provide an alternative route for the relaxation of excited carriers. In amorphous or multi-crystalline material, but also in low quality crystalline material, this effect may be the dominant recombination process The process was first explained by William Shockley, Robert Hall and William Read in 1952. [21,22]

1.3.2.4 Surface recombination

The above mechanisms are all related to bulk losses, which happen inside the material. Additionally, surface recombination losses also play a role. Surface recombination is an extension of SRH recombination where the intermediate band gap defects occur at the device surfaces. Any interruption of the periodic crystal structure at the surfaces leads to dangling bonds known as defect states. The surface recombination mechanism is very relevant in the context of light trapping, as this mechanism is crucial to textured surfaces in terms of increased surface area and the surface damage caused by the etching method used for texturing the surface.

The surface velocity is an important parameter which is defined as the velocity with which the charge carriers recombine at the surface. The surface recombination velocity clearly impacts on the carrier lifetime and the more recombination mechanisms are present, the shorter is the carrier lifetime. If, however, the device is well passivated and has low surface and Auger recombination losses, then the overall recombination is dominated by the bulk. Therefore, thinner substrates are now being used, e.g. substrates of ~180 μm thickness, which have lower bulk recombination rates.

In n-type semiconductor material, the surface recombination $R_{surface}$ is an important process and which is described[15]

$$R_{surface} \approx S_{sr}\,(p_{surface} - p_{\circ}) \qquad (1.30)$$

where $p_{surface}$ and $p_{\circ}$ are the hole concentration at the surface and the equilibrium hole concentration, respectively. S_{sr} is the surface velocity of minority charge carriers, which is the speed with which the carriers can recombine at the surface via (Shockley-Read-Hall recombination) SRH recombination. S_{sr} is the parameter of measure in determining the surface recombination and is given as a product of $v_{th}\sigma_p N_{STD}$ where is the v_{th} thermal velocity (cm/sec), σ_p is surface trap density (cm^{-3}) and N_{STD} is the capture cross-section per cubic cm. Therefore, the surface velocity of the minority charge carriers is crucial for controlling the surface recombination. Commonly, two complementary approaches are used; one way is to reduce the trap density at the surface by passivating these recombination centres. Typically, silicon oxide[23], silicon nitride or aluminium oxide [19] are deposited, which have the additional benefit of antireflection coating (ARC)[24]. Good passivation surface can be prepared with $N_{STD} < 10^{10}/cm^2$ eV and is achieved an interface of Si/SiO_2 where typically $S_{sr} \leq 10$ cm/sec.

Another way is to reduce the excess minority charge carrier concentration ($p_{surface}$ or $n_{surface}$) by introducing a high doping concentration that acts as a barrier for minority carriers at the surface. This method is called surface field passivation and is significantly applicable to the back surface of FB device to create a lower defect density at the metal / Si interface. Lifetime of charge carriers in terms of S_{sr} can be given as follow:

$$\tau = \frac{1}{\sigma_e S_{sr} n_{h,impurity}} \tag{1.31}$$

1.3.2.5 Surface damage losses and their impact on the V_{oc}

The maximum V_{oc} that can be achieved with a solar cell is limited by recombination currents, since the V_{oc} of a solar cell is determined by the splitting of the quasi-fermi levels, which, in turn, is limited by the recombination losses. The open-circuit voltage can be expressed in

terms of the $G_{photonflux}$ (generation rate of charge carriers per unit volume), the carrier lifetime τ and the intrinsic carrier density n_i. Assuming that the generation rate is uniform across the pn-junction, we can write[25]:

$$V_{OC} \approx \frac{2k_B T}{q} \ln\left(\frac{G_{photoflux}\tau_\circ}{n_i}\right) \tag{1.32}$$

n_i intrinsic carrier density in silicon, with a typical value of 1.5×10^{10} cm^{-3} at 300 K where T becomes more relevant parameter.

According to this equation 1.33, if the solar cell irradiance goes up (which increases the charge carrier generation rate, hence V_{oc} is also increased).

V_{OC} directly scales with $G_{photonflux}$ which is an effect also utilized in concentrator cells [25]

Defects clearly reduce the V_{oc} as they reduce the lifetime of minority charge carriers. As explained in equation 1.22, lifetime of the carriers, goes down with increased recombination losses. So, V_{oc} can be used as a direct indicator of the recombination losses in a solar cell.

1.4 Conventional solar device characterization parameters

When a diode is externally connected to a biased voltage, the current flow is given by the Shockley equation:

$$J_{Diode} = J_o \left\{\exp\left(\frac{eV}{k_B T}\right) - 1\right\} \tag{1.33}$$

As discussed before, a photocurrent flows when the absorbed photons produce charge carriers and are collected at the contacts. These charge carriers diffuse to the junction due to the concentration gradient and are separated across the junction via drift flow to produce the photo-current. Now there are two currents in the equivalent circuit, i.e. the diode current and the photocurrent as shown in Figure 1.10. The total current that flows in the equivalent circuit is given as follow:

$$J_{Total} = J_{Diode} - J_{Photocurrent} \tag{1.34}$$

$$J_{Total} = J_{\circ}\left(e^{\frac{eV}{k_B T}} - 1\right) - J_{Photocurrent} \tag{1.35}$$

where the current densities J represents the current per unit area. To understand the current flow mechanism, assume we operate between point A to B where a small forward biased voltage is applied. In this case J_{Diode} is negligible because the applied voltage is kept below the diode threshold. The total current in the circuit is given by the photocurrent current density $J_{photocurrent}$ which is represented in the 3rd quadrant for its opposite polarity compared to diode current. This current is called the short circuit current density (J_{sc}) which is the maximum current that can flow in the equivalent circuit at point A where it is a short- circuit condition. Now, once the forward biased voltage is increased say reaches at point C, the diode current starts flowing in the opposite direction to the photocurrent and so the total device current goes down.

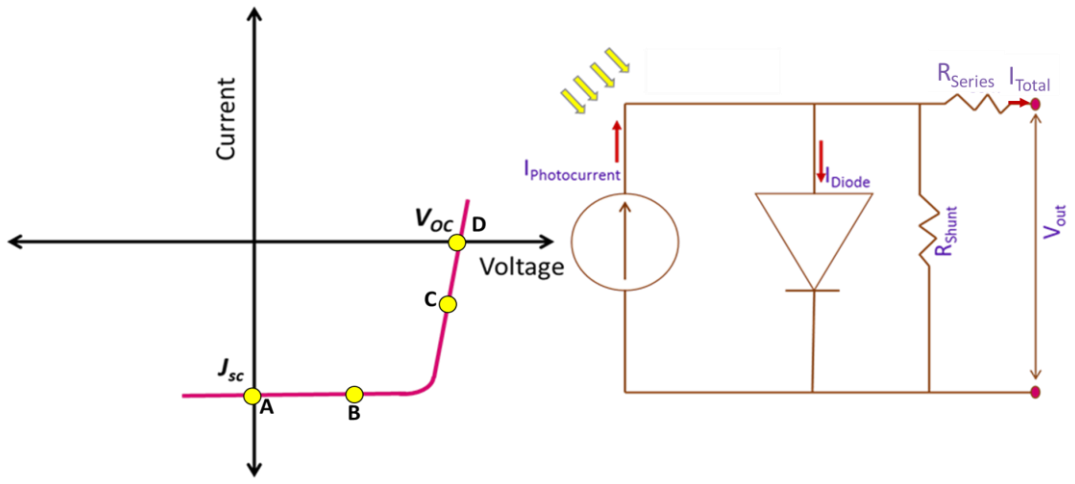

Figure 1.10. Left: An equivalent circuit for an ideal solar cell under illumination condition. Right: Graphical representation of an IV- characteristic curve under illumination condition where short-circuit and open-circuit two operational modes are shown by J_{sc} an V_{oc}.

At point D, the open circuit voltage (V_{oc}) refers to the voltage where the total current flow through the external circuit becomes zero. Mathematically, when J_{Total} is set zero in equation

1.36, $J_{photocurrent}$ becomes equal to J_{diode} and we can write an expression for the open circuit voltage as follow:

$$V_{OC} = \frac{k_B T}{q} \ln \frac{\left(J_{photocurrent} + J_{\circ} \right)}{J_{\circ}} \tag{1.36}$$

As $J_{photocurrent} \gg J_o$, so approximation in equation 1.38 is well justified.

$$V_{OC} \approx \frac{k_B T}{q} \ln \frac{\left(J_{photocurrent} \right)}{J_{\circ}} \tag{1.37}$$

whereby $\frac{k_B T}{q}$ is the thermal voltage.

Typically, $J_{photocurrent}$ has small variation but J_o can vary in significant order of magnitude so is the key factor of consideration. As recombination losses occur in the internal circuit of the solar cell, they directly impact on J_0 and thereby on the V_{oc}; hence we can interpret a variation of the V_{oc} as a signature of recombination losses. [15]

In real solar devices, due to electrical losses, non-ideal diode behaviour is introduced using a non-ideality factor as follow:

$$J_{Diode} = J_o \left\{ \exp\left(\frac{eV}{nk_B T} \right) - 1 \right\} \tag{1.38}$$

Practically, resistive losses lead to lower FF, which are indicated by n>1 and can vary up to a value of 2. n not only lowers the FF but also accounts for a high recombination loss in device. As we have discussed before that Voc indicates recombination losses, so we can rewrite equation in terms of ideality factor:

$$V_{OC} \approx \frac{nk_B T}{q} \ln \frac{\left(J_{photocurrent} \right)}{J_{\circ}} \tag{1.39}$$

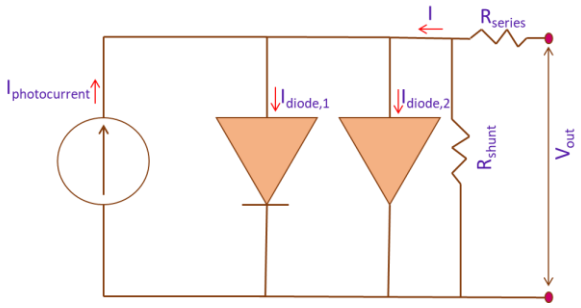

Figure 1.11. An equivalent circuit diagram representation for a real solar cell as a two-diode model where diode 1 has an ideality factor=1 and diode 2 an ideality factor >1.

In real devices, n>1 and the mathematical description considers a two-diode model, as shown in Figure 1.11. Diode 1 represents the ideal behaviour (n=1) and Diode 2 the non-ideal behaviour (n>1). Mathematically, this can be described as:

$$J_{Total} = J_{\circ 1}\left(e^{\frac{eV}{n_1 k_B T}} - 1\right) + J_{\circ 2}\left(e^{\frac{eV}{n_2 k_B T}} - 1\right) - J_{Photocurrent} \tag{1.40}$$

The operating region of a solar cell where it can generate useful output power, is between $V=0$ to $V=V_{oc}$. The power generated is calculated in the fourth quadrant of the I-V curve by multiplying I and V. The most important point on the I-V curve is the one where the product of voltage and current is maximum, also referred to as the maximum power point P_{MPP},

$$P_{MPP} = V_{MP}.I_{MP} \tag{1.41}$$

As shown in Figure 1.12 this point defines the maximum area of the rectangle that can be fitted into the IV curve. Similarly, another rectangle is defined at the (V_{oc}, I_{sc}) point. Together, the ratio of both products defines the fill factor (FF) of a solar cell.

$$FF = \frac{P_{MP}}{V_{OC}.I_{SC}} = \frac{V_{MP}.V_{MP}}{V_{OC}.I_{SC}} \tag{1.42}$$

The most important figure of merit for a solar cell is the output power conversion efficiency (PCE), η, which is defined as

$$\eta = \frac{P_{MP}}{P_{incident}} = \frac{FF.V_{OC}.I_{SC}}{P_{incident}} \tag{1.43}$$

with $P_{inc.}$, the incident power. The product of the *FF*, V_{oc} *and* J_{sc} describes the maximum output power of the device, and the ratio of this maximum output power against the input power determines the rated solar cell efficiency. Typically, standard test conditions assess the efficiency with an AM1.5G spectrum at an integrated power of 100 mW/cm^2 at 25 ºC.

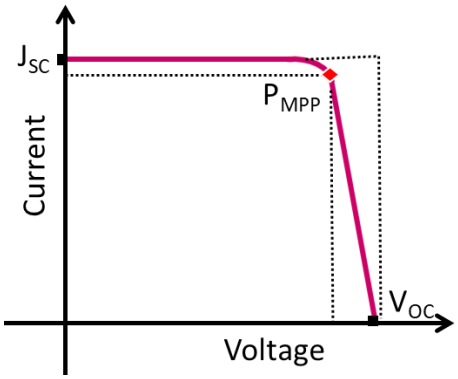

Figure 1.12. Graphical representation of power output rectangles represented at P_{MPP}, V_{OC} and I_{SC} points, are used to calculate the FF of a solar cell. For simplicity, the power output is displayed in the first quadrangle.

Another parameter that is closely related to the power efficiency is the external quantum efficiency (EQE). The EQE depends on both optical and electrical losses in the solar device. The EQE is assessed at the short circuit condition, under illumination. The corresponding photocurrent ($I_{photocurrent}$) that is generated is a function of the wavelength and is defined as follows:[26]

$$EQE = \frac{number\ of\ charge\ carriers\ collected}{number\ of\ incident\ photons}$$

$I_{photocurrent}$ is the maximum possible photocurrent that results if all the incident photons with E > E_G create e-h pairs and are collected. Since the EQE is measured in short circuit mode (*V=0*), the J_{sc} can be calculated by integrating the EQE over the full wavelength range, which, for silicon, is typically 400-1100 nm[26].

$$J_{sc} = \int_{\lambda_1}^{\lambda_2} EQE(\lambda).\phi_{incident}(\lambda)d\lambda \qquad (1.44)$$

where $\phi_{incident}(\lambda)$ corresponds to the standard spectrum of AM 1.5.

1.4.1 Parasitic Effects and Two Diode Equivalent Circuit of a Solar Cell

Many factors can influence the ideality factor of a solar cell. Major factors are the series resistance and the shunt resistance, which significantly affect the external current flow in the circuit. The series resistance arises from the ohmic losses and it needs to be balanced against the optical shading effect; so while the front contact grid should be as large as possible to reduce the contact resistance, it should be as small as possible to shade the least light; a typical compromise is 10%.[27] The diode equation for an equivalent circuit including series and shunt resistance can be written as follows;

$$J = J_{\circ 1}\left(e^{\frac{eV - JR_{series}}{n_1 k_B T}} - 1\right) + J_{\circ 2}\left(e^{\frac{eV - JR_{series}}{n_2 k_B T}} - 1\right) + \frac{V - JR_{series}}{R_{Shunt}} - J_{Photocurrent} \qquad (1.45)$$

The charge carriers flow to the respective contacts and the resistance to this flow is measured in terms of series resistance of the solar cell. The shunt resistance accounts for all possible current leakage paths across the pn-junction. Both resistance losses lead to a lower FF of the solar cell and their respective effect is depicted in Figure 1.13 (a). In case of shunt resistance, as shown in Figure 1.13 (b), as the value goes down, the FF is lowered down but at a certain R_{shunt} value (10 ohm.cm^2), circuit becomes short circuited so V_{oc} (at open circuit mode) cannot be determined as intersected voltage value along horizontal axis.

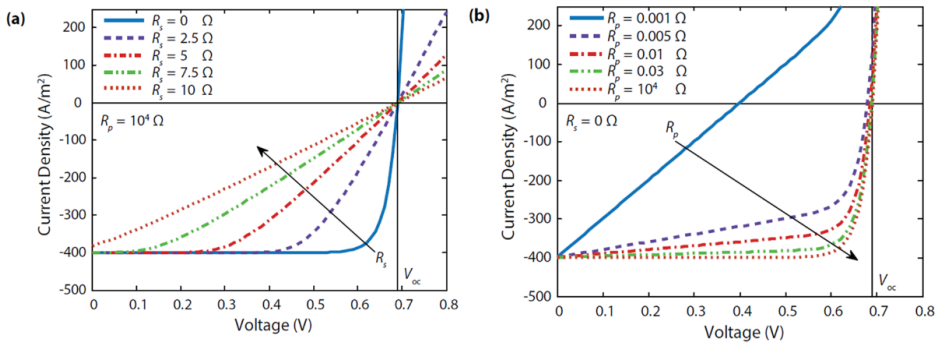

Figure 1.13. Effect of (a) Series resistance and (b) Shunt (parallel in equivalent circuit) resistance on solar cell IV- curve in terms of lowering of FF. [26]

1.5 Shockley-Queisser limit - Ultimate efficiency limit

Thermodynamics limit provides an upper limit on a classical engine which can be achieved by converting heat to work. To determine this limit, we can consider the solar cell as an engine which absorbs energy from a hot reservoir. The heat engine (solar cell) operated between absorber and surroundings with temperatures, T_A and T_C= 300 K. As heat is absorbed into absorber and stored as chemical energy (stored in e-h pairs), the solar cell converts this chemical energy to the electrical energy. Here it is assumed that this conversion is lossless with efficiency of 1. In thermodynamics, a Carnot engine is the ideal with an efficiency limit given as [15]

$$\eta_{Carnot} = 1 - \frac{T_{Cold}}{T_{Hot}} \tag{1.46}$$

Comparing it to the solar cell as an engine, we can write

$$\eta_{TD} = 1 - \frac{T_C(T_{Cold})}{T_A(T_{Hot})} \tag{1.47}$$

Here, an absorber is considered as a blackbody, absorbing all incident radiation. The maximum absorber efficiency can be achieved under maximal concentration given as

$$\eta_{Abs}^{\max} = 1 - \frac{T_A^4}{T_S^4} \tag{1.48}$$

where T_A is the absorber temperature and T_S is the sun temperature (6000 K).

From equation 1.50 and equation 1.51, the efficiency of the absorber (η_{Abs}) is higher when T_A is lower whereas the efficiency of a heat engine (η_{TD}) is higher when T_A is higher. For total solar cell efficiency η_{SC} , we combine these equations as follow:

$$\eta_{SC} = \left(1 - \frac{T_A^4}{T_S^4}\right)\left(1 - \frac{T_C}{T_A}\right) \tag{1.49}$$

From this equation 1.52, the maximum limit is achievable as 85% [28]at T_A= 2480 K. This model does not represent real solar cell, where all the solar spectrum is utilized by the

absorber material with a lossless conversion of chemical into electrical energy. But it emphasizes on the physical limit of the utility of solar spectrum.

A solar cell based on a single semiconductor material with a single bandgap energy cannot reach this limit because photons with an energy below the band gap value are not absorbed, while photons above the band gap energy are only partially converted and cause thermalization losses. The efficiency limit based on these two effects (lack of absorption and thermalisation) was first determined by Shockley and Queisser in 1961, and it is known as the "Shockley-Queisser limit". The model considers an ideal single junction solar cell where the ideal device excludes all extrinsic losses such as contact losses and optical losses from the surface of the absorber material. Under these ideal conditions, photons are fully absorbed above the band gap and not at all absorbed below the bandgap. The loss mechanisms considered by this model are these unavoidable intrinsic losses only and so the maximum efficiency limit is calculated from the short circuit current that is extracted per incident photon. The ideal efficiency is a function of bandgap shown in Figure 1.14.

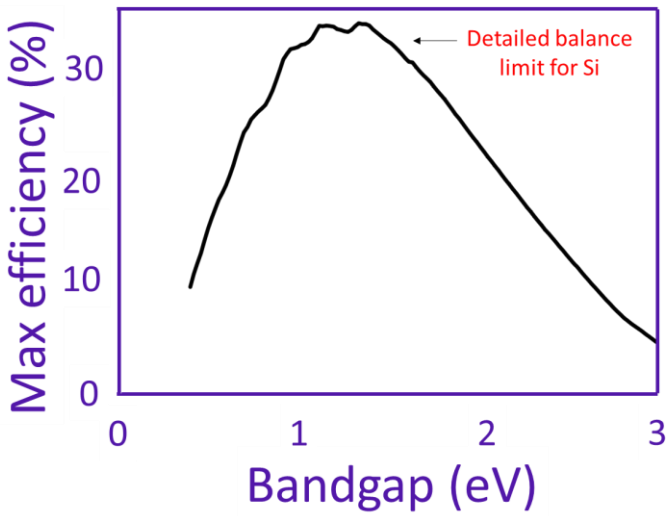

Figure 1.14. Calculation of the maximum efficiency of a single junction solar cell as a function of band-gap energy, known as the Shockley- Queisser limit model. [28]

The maximum efficiency calculated at 1 sun is around 30% for a material bandgap between 1.1 and 1.6 eV as highlighted by Figure 1.14.[29] Low bandgap semiconductors lead to a

decrease in efficiency due to thermalization losses resulting in a low V_{OC}, while higher bandgap semiconductors do not absorb low energy photons and therefore exhibit a low J_{SC}, the silicon band gap is close to the efficiency maximum and silicon (31 % with a band gap of 1.12 eV) is therefore a very good choice for a PV material. This efficiency limit for silicon is recalculated as 29.4% by Richter et al. where the non-radiative recombination losses are taken into account.[30] Compared to the modern monocrystalline silicon solar cell which has achieved an efficiency of 25%. Practically efficiency is lower due to optical and the contact /Si interface losses.

2 Chapter: Approaches for optical pathlength enhancement in silicon solar cells

Why apply light trapping in solar cells?

Light trapping in solar cells is realized to boost the absorption. Thus, light trapping in solar devices can give an enhanced short circuit current density (J_{sc}). The ultimate success of PV technology depends on efficiency enhamcement and effective cost reduction.

Integrating solar devices with light trapping nanostructures provide the simultaneous solution to these objectives. In weak light absorbing materials, light trapping allows the use of thin absorbing layer, reducing material's consumption without reducing the effective photo-generated charge carrier collection by reduced carrier collection path length in thin active layer. For cost-effective applications, thin film based PV technologies are potentially interesting to study due to their small material usage, additionally, to their applicability as flexible building integrated modules to light weighted portable power devices. This is not only a cost-effective solution but, most importantly, provides a way to improve the open circuit voltage (V_{oc}) while maintaining J_{sc} thus resulting in high efficiency.

Consequently, light-trapping is a promising solution to improve solar cells efficiencies with low material consumption. Independent of the material's thickness, the purpose of applying a light trapping structure in a solar cell to couple a maximum possible amount of photons into the active absorber layer and to increase the dwell time (path length) of light in it.

This chapter gives fundamental approaches for light trapping as well as the limitations to the enhanced light absorption factor in a silicon material layer. Commonly observed optical mechanisms are classified based on ray optics and wave optics; light trapping structures are discussed in the following section under the regiems of both ray and wave optics.

2.1 Geometrical optics

Geometrical optics is applicable when the interacting electromagnetic radiation has a small wavelength compared to the geometrical dimensions of the system under study. In such interactions, light propagation is studied as ray optics. When these light rays propagate in two media of different refractive indices, the reflection, refraction and transmission occurs at the interface and are described by Fresnel's equations. These equations also provide formulas of basic optical phenomenon like the total internal reflection and the Snell's law of refraction, discussed later. Likewise, the attenuation of the intensity of light when travelling in a material given by the Lambert-Beer law, also comes under the study with geometrical ray optics. In solar cells, the most commonly used silicon layer thickness is nearly 200 μm, much higher than the interacting light wavelength.

2.1.1 Anti-reflective dielectric coatings

Major optical loss comes from the reflectance at the front surface of the solar cells. For a planar Si surface, nearly about 30% of the incident light is reflected out at the Si/air interface. A commonly used technique to reduce front reflectance is to apply an anti-reflection coating (ARC) layer placed on the front surface of the solar cell active layer. Reflection of light between two given surfaces is given by Fresnel-reflection:

$$R = \frac{(n_1 - n_2)^2}{(n_1 + n_2)^2} \tag{2.1}$$

where n_1 and n_2 are the refractive indices of two media. Light reflectivity is strongly dependent to the indices contrast between the two media. For an air/silicon interface, R=30%. An intermediate material layer can be introduced to lower the indices contrast with an intermediate refractive index value given by $n_{ARC} = \sqrt{n_1 . n_2}$. The thickness of the ARC is approximately equal to the quarter wavelength (λ/4) inside the dielectric layer as shown in Figure 2.1 so the reflected waves will interfere destructively, resulting in lower reflectivity from the front surface. ARC coating is commonly made up of dielectric material with refractive index n_{ARC} lower than the absorber's index value. If the ARC film satisfies the

condition of equation 2, the reflection losses at wavelength (λ) can be significantly minimized.

$$n_{ARC}.t_{ARC} = \frac{\lambda}{4} \qquad (2.2)$$

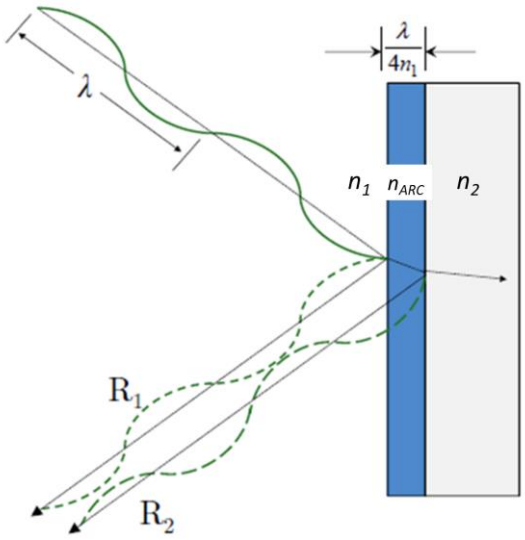

Figure 2.1. Destructive interference caused by an ARC with a thickness of quarter wavelength.[31]

Single ARC cannot meet the requirement of a broadband anti-reflection so multiple coatings are applied to minimize reflectivity from the silicon surface. ARC can be made of dielectric material which makes SiO_2 and Si_3N_4 appealing candidates due to their additional beneficial surface passivation effects. However, the deposition process of such multiple coatings is often expensive for most commercial solar devices.

2.1.2 Optical pathlength enhancement

2.1.2.1 Planer metal reflector (ML) at the rear surface

The front surface reflectivity of a solar cell can be reduced by adding an additional layer of ARC with minimum parasitic absorption losses to the front surface. In a silicon, solar cell, photons with energy much higher than the band-gap ($E_{photons} > E_{gap}$) of silicon are absorbed within first few microns of the absorbing layer, whereas photons with low energy near the band-gap ($E_{photons} \sim E_{gap}$) need to propagate a longer distance. In this situation, a large

amount of light will be transmitted out of the solar device if no optical barrier is introduced at the front or rear of the device to trap this light. Rear reflecting coatings, increases the optical pathlength. This will avoid the light escaping through transmission from the rear surface and will double the light pass-length in the active layer. The most commonly used back metal reflectors are aluminium (Al) and silver (Ag) which provide light reflection over 95%. However, doubling the optical pathlength in active material is not sufficient to maximize photon absorption; a solution to this is another critical approach where light scattering centres are introduced to increase optical path length within the active layer based on total internal reflection, this idea of light trapping by total internal reflection was first proposed in 1965. [32]

2.1.2.2 Diffusive reflectors (DR) at the rear surface

This approach introduces the light diffusivity concept in the active material. To minimise the escape of light, light scattering centres can be used to scatter back the propagating light at the rear of the solar cell. Light is reflected at an oblique angle and if the incident angle exceeds the critical angle, total internal reflection occurs at the front surface and the optical path-length is further increased. In this case of diffusion reflectors (DR), total internal reflection is maximised by using pigment based DR to trap more light in the absorber medium. Here, the reflecting coating is made up of micro/nano scale particles which are dispersed into a transparent binding material. This simple technique leads to low parasitic absorption and high reflectivity for silicon solar cells in a cheaper way. The concept of diffusive light reflector was introduced by Götzberger for light confinement in thin film solar devices [33]. Cotter et al. calculated the absorption enhancement upper limit based on an optical model in thin film solar devices by considering both reflection and scattering effects from DR[34].

An expression for the optical enhancement factor A for weakly absorbed light in a planar silicon with perfectly-diffused and perfectly-reflecting DR is given as [35]:

$$A = \frac{4n_{silicon}.n_{DR}^2}{n_{silicon} + \sqrt{n_{silicon}^2 - n_{DR}^2}} \qquad (2.3)$$

From above expression, the light trapping properties of DR significantly depend on the contrast of refractive indices of the ambient and the DR material. The interaction between the electromagnetic wave and the pigment is explained by Mie scattering theory. The size compatibility of the pigment particles with that of incident wavelength, geometry and the distribution of these pigment particles can strongly affect the optical confinement of the DR. Lin et al. has calculated an overall 99% reflectivity from 400 to 1200 nm with cylindrical shaped TiO_2 based DR distributed in the active medium[36]. The distribution order of these particles can lead to different spectral responses; ordered distribution results in high reflectance in a narrow band while disordered distribution gives significant broadband performance with lower reflectivity.

2.2 Geometrical optics (Yablonovitch) Limit on light trapping

A surface that randomizes and diffuses light into the absorbing layer is known to be a suitable solution for light trapping. The textured front surface has the function of enhanced scattering of the incident light into absorber layer. Light scattered at angles larger than the critical angle is trapped by total internal reflection. The introduction of the Lambertian scattering surface into a solar cell modifies the standard exponential absorption where Lambertian diffusive surface is the surface where the radiant intensity is directly proportional to the cosine of the angle θ between the direction of the incident light and the surface normal. For a single optical pass through the absorber layer of a solar device, the absorbed light fraction is simply given by the Beer-Lambert law:

$$A(\lambda) = 1 - e^{-(\alpha\lambda)l} \qquad (2.4)$$

I_o is the incident intensity of light and α the absorption coefficient. The absorption with a planar surface is related to the optical path-length l and α which is the absorption coefficient of the light absorber material in the solar device and is wavelength dependent.

In silicon wafer, excellent light trapping can be achieved with Lambertian surface. In Figure 2.2, the demonstration of escape cone is shown for a rear Lambertian surface. The incident

light which is totally internally reflected will be absorbed by silicon while the remains will escape through the cone to the air.

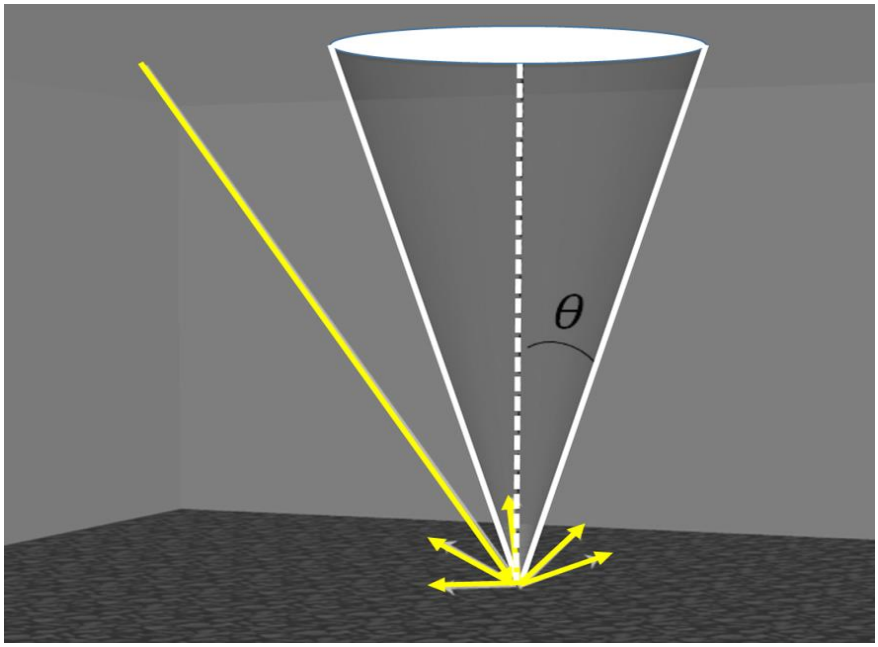

Figure 2.2. Illustration of the escape cone in a silicon absorber material with total internal reflection at a critical angle.

The critical angle is the half angle of the escape cone where the condition for total internal reflection is defined as: $\theta i \geq \theta c$. The critical angle of angle of total internal reflection is given by Snell's law of refraction:

$$n_{1,inc.}\sin(\theta_{1,inc.}) = n_{2,out}\sin(\theta_{2,out}) \qquad (2.5)$$

Here $\theta_{1,inc.}$is the angle between the incident light and the normal to the surface boundary and $\theta_{2,out}$ is the angle of the outgoing light with respect to the normal to the surface. Also, the refractive index $n_{1,inc.}$ corresponds to the medium in which light is incident and $n_{2,out}$ denotes the refractive index of the second medium where light escapes. From Snell's law, one can find that critical angle for silicon/air interface given as, $\theta_C = \sin\frac{1}{3.16} \sim 16^0$.

Integrating the escape cone reveals that only a small fraction ($1/n^2$) of light will scatter into the escape cone after encountering the Lambertian surface. According to Yablonovitch [1980s], an ideal Lambertian surface will provide the best light trapping scheme possible in a

textured slab using geometrical ray optics considerations. The Lambertian surface is a famous benchmark for light management in solar devices. An ideal structured surface is one which isotopically scatters light without any reflection losses. For an absorber material of refractive index n and thickness w, the optical path-length of weakly absorbed light is increased by an enhancement factor of $2n^2w$ with an application of a Lambertian surface at front. If this structure in a solar cell is combined with a perfect reflector at the back, this factor can be doubled and maximal optical path-length is given by[37]

$$l_{\max} = 4n^2 w \qquad (2.6)$$

For silicon absorber material, this factor translates to a path-length enhancement of around 50 times the solar device thickness. The maximal absorption for this optical path-length defined as Yablonovitch limit:

$$A_{\max} = 4n^2 w\alpha(\lambda) \qquad (2.7)$$

By considering that all the absorbed photons produce charge carriers and are collected

to contribute to the J_{sc}, then $A_{max.}$ provides an upper limit to the EQE of a solar cell. The statistical derivation of the fundamental limit can be found in [37].

2.3 Limitations of Yablonovitch limit

Now I discuss the theoretical aspects and the limitations of the Yablonovitch limit in this section. In the derivation of the Yablonovitch limit, the solar cell structures are considered without any optical losses, which are unavoidable in the realization of these solar devices. The optical losses in front and back of solar device, significantly reduce the enhancement factor of $4n^2$determined by the statistical optics.[38] To derive this fundamental limit, solar cell is assumed to be under isotropic illumination; independent of the angular confinement of the incident light.

Another assumption in the derivation of the fundamental limit is the thickness of the solar absorber material, which is much greater than the wavelength of incident light and is

described by geometrical ray optics. This assumption is not valid, when light propagation is considered in a thin absorber material. Another essential assumption for the Yablonovitch limit is the isotropic distribution of propagating light into the absorber material. Based on this, mostly isotropic light distribution is assumed to be equal to the Lambertian light scatterer. But this is not always the case, so the fundamental limit is not applicable to systems with selective directional light scattering such as gratings of periodicity significantly greater ($a>>\lambda$) than the wavelength of incident light.

Following the assumptions of absorber thickness and period size of the grating, the Yablonovitch limit is only applicable when the wave nature of light is not considered. At the same time, the wave optical effects such as interference, diffraction and local field enhancement phenomenon cannot be disregarded when the absorber thickness and grating period size get comparable to the wavelength of incident light. Wave optics becomes significantly important in thin film solar devices and solar devices with diffraction grating nanostructures. This fundamental theory, however, cannot be applied in the nanostructures regime. Briefly, wave optics is discussed in the following section.

2.4 Wave Optics

In wave optics, the light propagation can be described by plane electromagnetic waves which are time harmonic solution of the Helmholtz equations and is described as follow:

$$E\omega(x,t) = E_{\circ}e^{i(kx-\omega t)} \qquad (2.8)$$
$$B\omega(x,t) = B_{\circ}e^{i(kx-\omega t)}$$

where the direction of the electromagnetic waves is given by the k wave-vector. Wave optics not only describes geometrical ray optics but also the light interaction with system of dimensions compatible or smaller than the wavelength of light. Important phenomenon explained by wave optics are the light diffraction the interference of light waves.

When light is incident on the surface of a medium, it is redirected when it bounces off an obstacle: reflects or refract from one medium to another one with a change in its propagation

direction. This phenomenon also happens when light passes through an aperture. In 1665, Francesco Grimaldi published a work based on the discussion of this phenomenon[39]. In his experimentation, he shone a very narrow beam of light into a dark room and placed a rod in its path. He observed that the casted shadow of the rod in the cone of light was broader than the shadow predicted by geometric ray optics. He named this phenomenon "diffractio" which means "breaking up". He also used these results of his experiment to argue for the wave nature of light.

The patterns formed by superposition of diffracted waves is called as diffraction pattern and can be realized by textured structures. An important realization of diffraction is if the obstacle is an array of diffracting units that yield a periodic alteration of the phase or amplitude of the transmitted wave. Such an obstacle is named a diffraction grating.

The structures with lattice periods of comparable size to the wavelength of incident light do not obey the laws of geometrical ray optics. Such periodic structures are described using the wave nature of light which produce many interesting properties like interference; which cannot be described by geometrical ray optics. These periodic structures are also known as photonic crystal and may be classified based on periodicity such as one (1D), two (2D) or three-dimensional (3D) periodicity and these structures serve different purposes in a solar cell. In 1983, Sheng et al. first used the periodic structures to improve light trapping in solar devices. [40]They recognised a potential absorption enhancement in light trapping from these periodic structurers compared to the randomizing silicon surfaces. These periodic structures can be applied to both front and back surfaces of the devices. At the front surface, the periodic structures serve both as an ARC and to achieve light trapping. On the other hand, back surface structures are usually optimized to a narrow spectrum range; this range is determined by the spectral absorption of the solar cell along with its thickness which acts as a high energy light filter. For silicon absorbing layer of 20 microns, the light spectrum below 800 nm will be absorbed before it reaches to the rear side. So, the back side periodic structure

optimization needs to be in the wavelength range (Δλ) of 800 to 1100 nm, about 30 % of the full spectrum range.

2.4.1 Diffraction Gratings

Optical diffraction gratings are structure which redirects (transmits or reflects) the incident light into discrete diffraction orders. The diffraction orders are defined at certain angles where the scattered waves superimpose constructively. The diffraction angles of the diffraction orders are determined by the grating equation.

Here, we examine how a grating interacts with light to redirect the incident light into discrete diffractive orders. A diffraction grating is basically characterized by a grating vector **Γ,** which in terms of magnitude is defined as |**Γ**| = 2л/Λ, where Λ is the period of the diffraction grating, and the grating vector **Γ** is in the direction of periodicity. The grating redirects the incident light by adding integer multiples of the grating vector $m.\mathbf{\Gamma}$ to the incident transmitted parallel wavevector k_i.

$$k_m = k_i + m.\Gamma \tag{2.9}$$

m is the diffracted order. To explore more, we substitute the vector x and z components of the wavevectors into a two-dimensional geometry and rewrite above equation:

$$\frac{2\Pi n_2}{\lambda}(\sin\theta_m \dot{x} + \cos\theta_m \hat{z}) = \frac{2\Pi n_1}{\lambda}(\sin\theta_i \dot{x} + \cos\theta_i \hat{z}) + \frac{2\Pi m}{\Lambda}\dot{x} \tag{2.10}$$

Here, λ is the free-space wavelength of light $k = \frac{2л}{\lambda}$ is the wavenumber and n_2 and n_1 are the refractive indices of the transmitted and the incident medium, respectively.

We can rewrite the equation for $\sin\theta_m$ by only considering the ẋ components:

$$n_2 \sin\theta_m = n_1 \sin\theta_i + m\frac{\lambda}{\Lambda} \tag{2.11}$$

For the diffraction order is numbered as zero order and Snell's law is reproduced from the grating equation for m=0.

We can see that diffraction angles are highly dependent on λ. If the grating period Λ is chosen small with respect to the light wavelength, then small changes in the wavelength affect θ_m significantly. As gratings are highly dispersive, very sensitive to wavelength, they find direct and natural application in spectroscopy. In general, the larger is the ratio of the grating period to the incident wavelength, the more diffraction orders exist.

2.4.2 Wave optics (Electromagnetic) limit on theoretical designs for enhanced absorption

In the literature, several grating designs are investigated based on different numerical methods, to attain high absorption enhancement in solar cells. These methods include a rigorous coupled wave analysis (RCWA) method and finite difference time domain (FDTD) method. Recently, Fan and his co-workers, developed a statistical coupled-mode theory where wave optics is used for the description of light absorption enhancement with wavelength-scale grating structures. To illustrate their theory, a high-index optically thin-film active layer is considered with a high-reflectivity mirror at back and air on top, as this system provides guided modes. Light trapping is realized when incident plane waves are coupled into these guided modes, either by applying wavelength-scale grating with periodicity.

By considering the case of very low absorption, when light propagation is realized by exciting individual guided modes, the maximum spectral absorption can be calculated by the temporal coupled-mode theory equation. By adding up the maximal absorption of all individual guided modes of the active layer in the limit of strongly coupled guided modes to the incident light, Fan and co-workers derived an upper limit for the maximum enhanced absorption Abs. $_{MAX}$ in the solar device given as:

$$A_{MAX.} \frac{1}{\triangle \omega} \sum \frac{2\Pi \delta_i m}{N} \qquad (2.12)$$

where m is the number of coupling modes in the active layer and N is the number of incident plane waves that can couple to a certain guided mode. δ_i is the intrinsic loss rate related to guided modes which is equal for all.

Equation 2.12 is valid over a frequency bandwidth $\Delta\omega$ where all resonances are occurring. From each of the resonant mode, the peak absorption is in fact strong but relatively thin so the total enhanced absorption factor can be obtained by summing over the contributions from all individual resonant modes. Fan et al. has detailed that the fundamental limit of $4n^2/\sin^2\theta$ is correctly applicable to the bulk structure regime but in case of nanostructuring for light trapping, the fundamental limit can be higher with the application of proper grating design.

As the thickness d of device is much larger than the incident wavelength, the waveguided modes can be approximated as propagating waves. Then m, the total number of resonant modes in the active layer of solar device is equal to the product of the local volume and the photon flux density. For the specific case of subwavelength confinement model, the absorption enhancement factor of $4n^2 \times 12$ is determined with isotropic angular response and over an unlimited spectral bandwidth. In next chapter, I will review the nano-scale diffraction light trapping structures reported in literature by comparing with the micro-scale structures.

3 Chapter 3: Review of light trapping nanostructures

Crystalline silicon (c-Si) solar cells are the dominant photovoltaic technology and represents nearly 92% share of the production market with the remainder being thin film technology. Monocrystalline and multi-crystalline silicon solar cells have achieved 25.6 % and 21.7 % power conversion efficiency (PCE), respectively, in the laboratory[41,42]. Silicon is a weak absorber (at longer wavelength) material with high refractive index. To reduce the difference between the theoretical (29.4%) and practical silicon solar cell efficiency (25%), in optical and recombination loss is needed to be reduced. For the optical side, reflection suppression is achievable using ARC and the index graded nano-structures whereas in the electrical side, light trapping structures allow a significant reduction in material thickness (lower bulk recombination) while sustaining the high light absorption.[43]

High reflection losses (30%) at front surfaces are reduced using ARC whereas the weak light absorption character at longer wavelength is suppressed using light trapping structures. AR effect mainly applies 1. high index anti-reflection coatings (ARC) which are optimized in thickness on planar silicon surface to reduce reflectance from the silicon front surface. However, these high index coatings tend to produce undesired reflection losses of incident light and do not provide light trapping. Another AR approach is achieved from 2. nano-textured silicon surfaces, famously known as ‘’Black silicon’’ for graded index character of textured features.

The research and development efforts to enhance the efficiency of silicon solar cell by thinning down the silicon wafer for lower bulk recombination (high V_{oc}) while maintaining the high J_{sc} by applying efficient light trapping schemes. In thin silicon devices, micron-scale

structures cannot be because the size of the nanostructures become compareable with the thickness of the absorbing layer.

In this chapter, I will describe the State-of-the-Art of nanostructures integrated into silicon solar cell devices.

Two distinct categories are introduced with respect to their scale:

- Wavelength scale texturing (Random/Periodic)
- Sub-wavelength scale texturing (Random/Periodic/quasirandom(QR))

The first category regards the length scale of micron-size under ray optics regime whereas nano-scale covers structures under wave-optics study. Sub division of nano-scale structucres is then compared based on periodicity.

3.1 Micro-scale texturing (ray optics)

3.1.1 Upright pyramids

Randomly distributed pyramid texture facing the incoming solar radiation is the current State-of-the-Art for light trapping scheme in commercial solar cell technology. Together with a thin anti-reflection film, it offers very high performance and allows relatively simple implementation by wet etching. An additional advantage of using the wet etch process is that it cleans saw-damage and unwanted contamination on the surface, typically used before solar cell fabrication. The basis for the ability of creating pyramids by a simple wet etching process is the crystal structure of silicon, as silicon crystallises in a diamond lattice, which is illustrated in Figure 3.1. The diamond lattice can be understood as two interpenetrated fcc sub-lattices [44] with one sub-lattice being displaced from the other by a quarter length along the body diagonal. This structure creates a different packing density along the different lattice planes. It must be noted that such pyramid structures are only observed for [100] oriented silicon wafers and only formed by preferential etching along crystallographic orientations in monocrystalline silicon. As the packing density is higher in the (111) planes compared to

the (100) planes, the etch rate is faster along the (100) planes, which generates facets of (111) planes. The resulting pyramids typically cover the surface with average size of 10 μm [given the angle of 54.7 degrees].

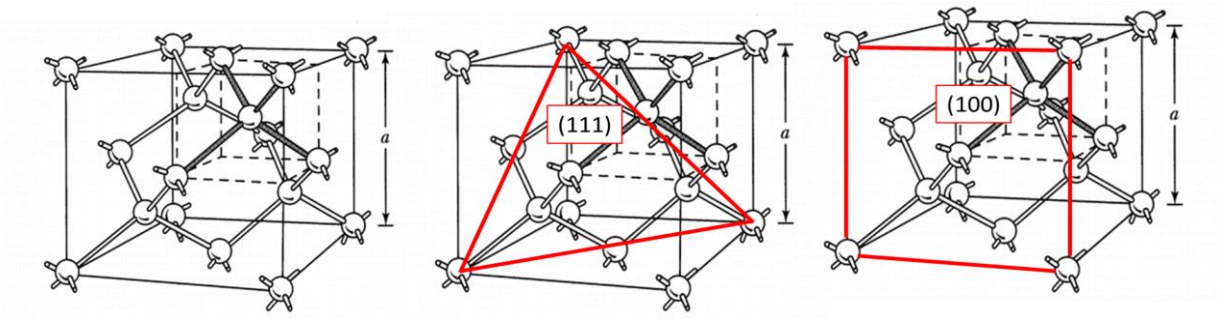

Figure 3.1.Illustration of the silicon diamond crystal lattice structure along with its planes representation.

The structure is random in its nature due to varied distribution in positioning and size over the surface. Commonly used wet etching methods involve alkaline chemistry such as potassium hydroxide (KOH) or (tetramethylammonium hydroxide) TMAH. As the chemical etch depends on to the orientation of atomic planes of the wafer, the angles are different, and random distributed, for multi-crystalline silicon. The alkaline solvents provide a hydroxyl group, which attacks silicon with a resultant H_2 by-product that escapes in gaseous form (bubbles). The chemistry is summarised by the following reactions[45]:

$$KOH \rightarrow K^+ + OH^-$$
$$Si + OH^- + 2H_2O \rightarrow Si(OH)_2 + H_2$$
$$Si(OH)_2 + 2H_2O \rightarrow Si(OH)_4 + H_2$$

Isopropyl alcohol (IPA) is commonly used as an additive to increase the number of etching spots by reducing the surface tension and resulting in a high-density pyramid texture. [46] [47]

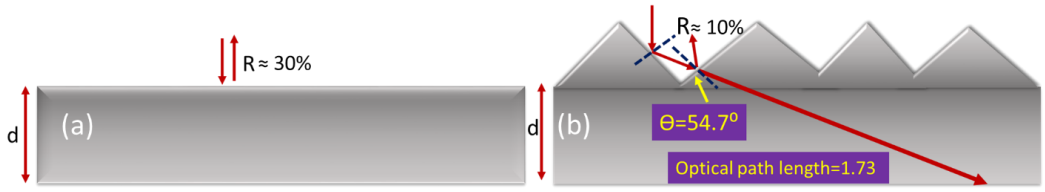

Figure 3.2.Optical ray tracing is illustrated for an incident light normal to the silicon front surface. (a) Polished surface. (b) Upright pyramid texture.

The light in-coupling is shown in Figure 3.2, which illustrates how the pyramid structure increases the probability of light coupling into the high index material. Because the light reflected at the first interface will hit another face, it gets at least one more chance to enter the absorber material. Multiple bounces (scattering) at the front surface couples even more light into the absorber. This effect accounts for a lower reflection when front pyramid surface is used. Once light enters the silicon wafer, the optical path length $\left(\frac{1}{\cos\theta}\right)$ is increased by a factor of 1.73 for a facet angle of 54.7 degrees. The details of ray tracing analysis for upright pyramid structures can be found in reference [29] where micron-sized pyramids have been studied using the geometrical optics approximation. As conventional pyramids provide the benchmark for light trapping in silicon solar cells, I use them as a reference to make a fair comparison with nanostructures; the detailed fabrication and characterization methods are described in section 4.3.

3.2 Periodic Inverted pyramids

Alternative textures are aimed at improving the scattering efficiency, the honey-comb structure being a good example, which is periodic and micron-sized. Inverted pyramids use the same multi- bouncing mechanism as upright pyramids. Periodically arranged inverted pyramids (honey-comb) structures performance was shown by Baker-Finch et al [48] to be

optically comparable (J_{sc}: 41.71 mA/cm^2 with SiN (ARC): 72.8 nm) to the upright random pyramid texture (J_{sc}: 41.57 mA/cm^2 with SiN (ARC): 76.3 nm).

Corresponding to the higher performance of inverted pyramids, the highest performing solar cells use this geometry, e.g. the PERL cell with a reported efficiency of 25.0% (Zhao et al, 1998) [49] The fabrication process of inverted pyramids is more complex than that of upright pyramids, as it involves photolithography, laser ablation [50], ion implantation[51] [52] and a plasma etch clean process, the fabrication process costs more, its application at the industrial level are hindered.

3.3 Sub-wavelength scale texturing- Random texturing

More recently, sub-wavelength scale textured surfaces have been investigated showing potential to reach the Lambertian limit at lab-scale fabrication. Most prominent are the randomly etched features with gradient index density accompanying anti-reflection (AR) effects over a broad-spectrum range with large acceptance angle. This random structure is known as Black Silicon, which features nearly zero reflection over a broad spectral range and a large acceptance angle. The high index mismatch between air and silicon interface is reduced by incorporating tapered nano-texturing for lower reflection by grading the index value. Black silicon is created via a mask-less reactive ion etching[53] process with a mixture of (SF_6+O_2) or (F_2+O_2) gases, which creates standing arrays of needle-like structures. Their key advantage is the ease of fabrication and their exceptionally high AR performance, as they achieve low reflectivity (<1%) over almost entire spectrum. In comparison to pyramids, this texture is independent of the crystal orientation and being mask-less cost-effective process, which eliminates the need of vacuum based expensive AR deposition techniques, so it can potentially replace the current state of the art. But the limitation lies in the electrical regime where the nanotextured surfaces are highly prone to high recombination losses and the gain in

the optical regime is compromised by the electrical losses. This is why the record is only 22.1% from Aalto compared to 25.6% HIT cell with pyramid structures.

3.4 Sub-wavelength scale texturing- Periodic

3.4.1 Photonic crystal structures

Photonic crystals are a two-or three-dimensionally periodic structures that trap light by exciting guided modes. Photonic crystal light trapping structures operate in the wave optics regime and are correspondingly designed for thin film solar cells. Nanophotonic structured layers with several morphologies[54] include nanowires (Experimental J_{sc}: ~17 mA/cm^2 for 20 μm),[55] inverted nanopyramids (c)[56] nanodomes (theoretical J_{sc}: 33.7 mA/cm^2 for the 2 μm) [54], nanopillars (99% absorption over 300-900 nm range),[57], inverted nanocones (34% higher performance than flat counterpart) [58], nanocones (theoretical J_{sc}: 34.6 mA/cm^2 for the 2 μm) have been reported.[59]

3.5 Sub-wavelength scale texturing- Quasi-random

Periodic structured gratings are designed to excite well-defined diffraction orders with strong resonant absorption enhancement but their limitation is that the absorption enhancement is only achieved over a narrow bandwidth. In contrast, random structures offer a large number of diffraction orders that cover an extremely large bandwidth, but their limitation is that the absorption enhancement at each wavelength is relatively weak. Quasirandom (QR) nanostructured gratings are positioned between these two extremes by providing both strong and broadband absorption enhancement. The design of the quasi-random nanostructures follows the recipe of enhancing Fourier components with higher orders while suppressing Fourier component with lower orders [9, 23]. This approach promotes diffraction into higher angles, thereby boosting the light trapping properties. The period of the unit-cell is 1800 nm and each unit cell is composed of a matrix of 8 x 8 pixels [23]. The resulting Fourier spectrum is shown in Figure 3.3. Notice that the spectrum is characterized by a depletion of

energy in the low k components and a concentration of energy in the high k components. In my work, I have etched QR nanostructures into the front silicon surface as will be discussed in chapter 4.

3.6 Light trapping textures realization onto silicon solar cell

3.6.1 Industrial scale light trapping integrated solar cell technology

The three-main silicon solar cells are the PERL (passivated emitter rear localized), HIT (heterojunction intrinsic thin) and IBC (interdigitated back contact) architectures. All of these are currently using pyramids for light trapping in combination with single or double ARC. In PERL devices, micron-sized pyramids are already a benchmark for light trapping.[60] At laboratory scale, PERL device was reported with efficiencies of 24% in 1990 and 24.7% in 1996 and is the most efficient monocrystalline device to the date.

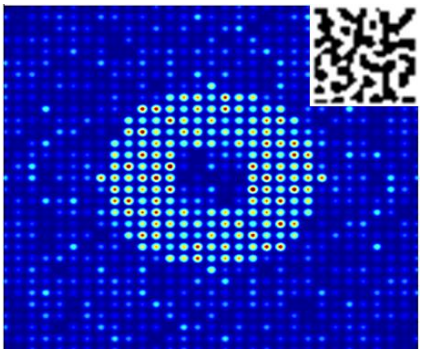

Figure 3.3. QR structure in Fourier and real space (inset) with a unit-cell of 1800 nm.

The catch in PERL is its high-quality passivation of all surfaces and its point contact design to minimize the metal/contact interface area to reduce recombination losses at the interface. It is important to say here that high-quality passivation and point contact design makes PERL fabrication, an expensive technology to implement on commercial level. As a resplacement of multiple lithography steps which make this process expensive, PLUTO [61](19.2%) device design was developed at same UNSW in 1985 and is commercialized by SunTech Co. [62]

IBCs: Another commercialized technology IBC solar cells use random upright pyramids integrated light structures. SunPower cooperation is a leading company in producing IBC modules with device efficiency of 24.2 % and 21% module efficiency. [63][64] The detail of this architecture is given in section 4.2, where I have fabricated these solar devices in our available facilities.

HIT: Another technology important for industrial commercialization, HIT solar cells were reported with an efficiency of 24.7 % for large area device (100 cm^2) by Panasonic[65]. HIT uses intermediate intrinsic amorphous silicon layers to reduce recombination, resulting in a V_{oc} of 729 mV compared to that of 706 mV in PERL devices. A heterojunction is built-up by introducing a wider bandgap material between the Si/metal interface. The wider bandgap material introduces energy steps due to a combination of two different band-gap materials. Now only holes (minority carriers) can drift by tunnelling through this energy step and advanced quality passivation is accomplished.

But due to the incorporated a-Si layer, the blue spectrum is compromised based on its high index gradient causing a lower J_{sc} value of 39.5 mA/cm^2 compared to PERL device with 42.7 mA/cm^2.[66] An important limitation of HIT design is the parasitic absorption losses due to TCO (commonly used is ITO) which is layered above the a-Si layer to achieve good conduction of carriers as a-Si has poor conduction. The HIT-IBC device is a combination of above two technologies to overcome the parasitic absorption losses at front contacts by moving them at the rear. Panasonic has optimized this design with the highest efficiency of 25.6 %[67]. Massive production technology: The above three technologies are expensive on a mass production level. Commonly solar cell architecture massively produced is Al-BSF p-type device due to its process simplicity and cost-effectivity. The centre of attraction in mass production is its simplification of the fabrication process. The above discussion shows that the light trapping structures are not updated since the commercialization of PV technology. The main reason is the cost of PV module fabrication which is 50 % of the total installation

(including cables, batteries and invertors) process, so cost-effective, high efficient textures are the key to replacement.

3.7 Why are nanostructured solar cells not as good as those using pyramids?

I will now address the question why nano-structures are mainly used in passive devices and are only reported with simulated J_{sc} values, and only very rarely feature experimental measurements. Simultaneously, I also address the question why Black Silicon does not provide the highest performance compared to pyramids despite its superior antireflection performance. As discussed above, the point of nanostructuring is to maintain a high J_{sc} in a thinner device, because thinner material allows for a higher V_{oc}. The relationship between wafer thickness W (μm) and the V_{oc} is described as follow:

$$V_{oc} \approx C + \frac{K_B T}{q} \ln\left(\frac{L}{W}\right) \qquad (3.1)$$

The larger the absorber thickness (W), the lower is the V_{oc}.[38,68]

However, the optimization of a nanostructured solar device requires a balanced design involving various parameters, such as shape, roughness, depth, aspect ratio, periodicity and fabrication method, all of which impact on the opto-electronic performance.

3.7.1 Surface area

Even though nano-texturing enhances photons harvesting, it also adds surface area to the device, which increases the surface recombination current and thereby lower the V_{oc}, as detailed by Oh et al. [69]. The non-planar junction caused by doping a nanostructured surface may also lead to lateral current flow and lower shunt resistance as reported by Hsu et al.[70] Doping control is more critical because the surface area is increased, the same doping conditions used in planar surfaces will show high lifetime of minority carriers compared to the lifetime at nano-textured surfaces [71] i,e in a report for a planar and nanostructured Si surface, lifetime varies from 130 μs to 71 μs at the same doping conditions. High dopant

concentration in textured surfaces make them highly vulnerable to the Augur recombination losses. [72] One might think of a solution by lowering the dopant concentration but this causes an additional increase in series resistance. This effect is also explained by Oh et al. in a report showing a 18.7% Black silicon solar cell. In this report a low sheet resistance showed a decrease in FF from 79.3 to 75.9% as R_{sheet} increases from 55 Ω/□ to 200 Ω/□. Sevin et al. reports a 22.1% black silicon IBC device by overcoming the surface recombination which is a commonly believed to be the cause of recombination in the nanotextured surface due to the increased surface area[53]. They found that conformal alumina layer deposition a good solution to passivate the device chemically and electrically.

An additional loss on the textured surface is the increased contact resistance, because roughness contributes to a poor silicon/metal interface. This point is discussed in detail by Naser et al. [66]

3.7.2 Etching transfer methods

In the dry etching method, nanostructures are etched away using a plasma which introduces many defects and damages to the surface. Intomat et al. [1997] used only dry etch (ICP-RIE) to etch nanostructures, passivated with SiN, showing an efficiency of 17.1 % while Schnell et al,[73] Yoo et al [74]and Zaidi et al. [75] experimented the same process and claimed that the absorption enhancement factor for nanostructures is compromised in the blue spectrum due to introduced damage at front surface[76]. Reactive ion etching can form a 50 nm thick layer of defects, called a dead layer. [77] The defect layer can significantly decrease the minority carrier lifetime; one report shows it goes down from 400 μs to 3 μs whereas a decent 20% efficient devices need a lifetime of 1 ms (corresponding to a surface velocity of 20 cm/sec). As a solution, post-processing of damage removal is performed via post-wet etching process to remove the damage introduced in the dry etching method. This additional process showed that the lifetime goes up from 3 μs to 36 μs. [78] Many groups studied the effects of damage removal etching (DRE) post-process where they found the unwanted optical loss from

featured textures [75][69].They suggested a balanced DRE treatment to optimize nano-texture for minimum surface damage while maintaining low optical losses as recommended by Otto et al[79]. The highest efficient reviewed above black silicon devices are not as good as PERL and HIT devices which incorporate micron-sized features. Later, Hung et al. reported the same device with an additional post wet etch featuring an efficiency of 15.1%. [80] Yoo et al [81] and Chen et al. [82] reported better output device in 2011 with an optimized passivation scheme 17.27%, 18.3 % respectively. Repo et al. used ICP -RIE with passivation Al_2O_3 and reported an efficiency of 18.7%. They did not use any post wet etch treatment but only Al_2O_3 as a passivation layer. [83]

3.8 Summary

This chapter has introduced the major light trapping schemes by categorizing them into either the ray optics or the wave optics regime and described the State-of-the-Art in both regimes. size and degree of periodicity. I have also discussed the current state of the art of micron-sized pyramid and compared them with black silicon AR texture. I reviewed a number of nano- light trapping grating structures (PC) reported on passive devices by raising the question of why these structures are not commonly apply into active solar cells to characterize in both optical and electrical regime. To address this question, I have discussed the limitation factors where benchmark parameters to analyse the optoelectrical character always focuses on absorption vs electrical losses.

To improve the State-of-the-Art, it is possible that nanostructured surfaces may outperform the existing ray-optics pyramid-type structures because of their ability to combine excellent AR coating with the efficient light trapping of quasirandom nanostructures, all in a thinner cell that has the potential to achieve a higher V_{oc}. My solution to this challenge is described in chapter

4 Chapter 4: Fabrication techniques and experimental details

This chapter gives an overview of the experimental techniques and provides a short theoretical background of methods and the equipment used for the fabrication of Si solar devices. In this work, I have fabricated two configurations of devices; front- back (FB) and interdigitated back contact (IBCs) solar cells. The fabrication of the basic FB structures consists of a thermally doped pn junction at the front of the silicon wafer and metal contacts at both the front and the back side of the device. The optimization of various parameters is discussed in detail; the goal is to obtain a good rectifying diode involving shunting paths elimination, reduced series resistance and conformal doping processes. The second type of structure I investigated were interdigitated back contact (IBC) solar devices, whereby both the p-type and the n-type contacts are placed on the back of the wafer as interdigitated fingers. The IBC architecture has advantages in terms of zero optical shading as it has a metal free front surface with all current-collecting contact fingers being placed at the back surface. These n and p type fingers are interdigitated by a minimum isolation gap. A photolithography process is used to create selective doped areas and selected metal deposition for creating the fingers. In addition, the integration of light trapping structures and the characterization techniques required to investigate the solar cells performances are described.

4.1 Processing of front back (FB) Si solar cell

All the processing steps are carried out in the cleanroom facility at the York Jeol Nanocentre. The process flow for the front back solar cell is shown in Figure 4.1 and each step is explained in detail. Even though most steps are commonly used in silicon processing, it is important to describe the aspects that are required to obtain highly efficient solar cells.

In the fabrication process of a solar cells, the main technical aspects to be considered are

1) Enhanced light absorption in the semiconductor material to increase the generation of charge-carriers.

2) Enhanced collection probability of light generated charge carriers.

The enhanced light absorption is the optical aspect of device and it is the main content of this thesis in terms of integrating light trapping structures into solar cells. The collection probability mainly refers to the electrical properties of solar devices in terms of shunting paths, series resistance, recombination losses, design of the metal contact grid design (for optimum transport of carriers) and the metal/silicon interface passivation (by enhancing the field at the back side of device). These details are discussed in following sections.

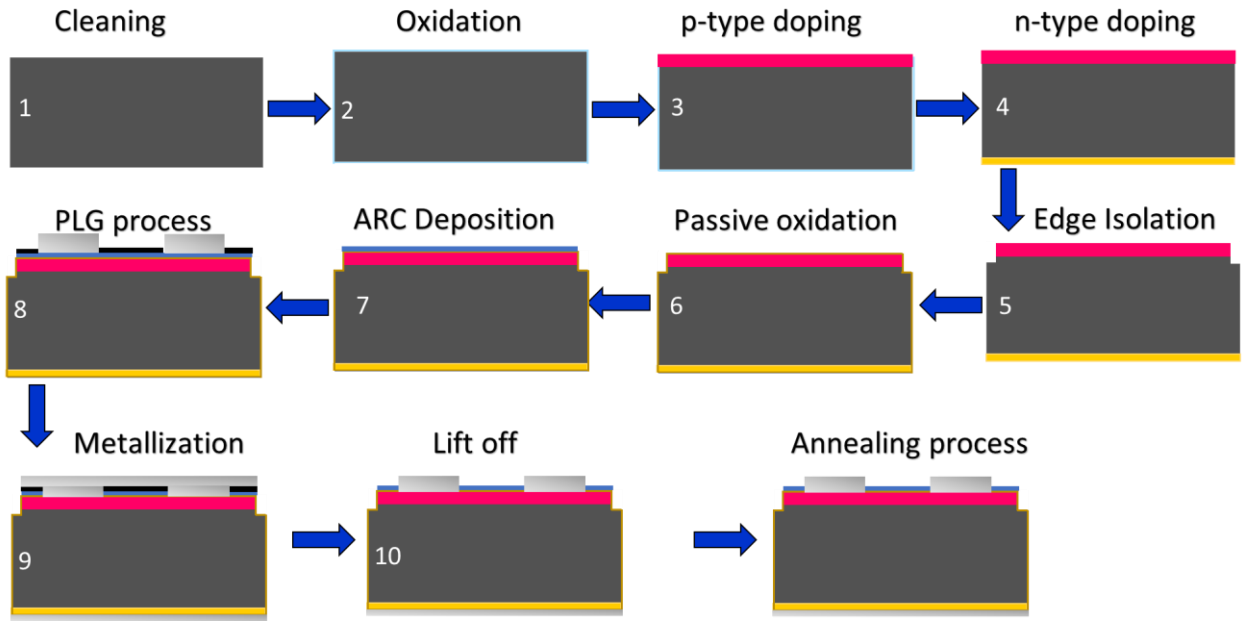

Figure 4.1. Fabrication process of front back (FB) silicon solar cell device.

4.1.1 Wafer specification

Thickness: The first step in the fabrication process is to select silicon wafers of the correct thickness, resistivity and quality. As silicon is an indirect material, the wafer thickness commonly used is 200 to 300 µm for effective absorption of photons; thicker material tends to deliver higher absorption, especially for long-wavelength (above 900 nm) light where the absorption coefficient is low (1000 cm^{-1} at bang gap edge), while thinner material delivers a

higher open-circuit voltage due to its reduced bulk recombination losses. As I am integrating light trapping structures on to devices, I used wafers with a thickness of 180 μm where the light trapping effect can be significantly observed if compare to a bare surface device.

Type and Resistivity: I used n-type wafer of resistivity in the range of (1 - 20 ohm.cm) with <100> ± 0.5º oriented planes; the material was sourced from Siltronix (France). Since the wafers are n-type, the dopant impurity in phosphorous. The resistivity is determined by the doping concentration which is then verified by using a four-point probe instrument (JANDEL RM3-AR). Briefly, the material's sheet resistivity is calculated by the following expression:

$$R_{Sheet} = \frac{\pi}{\ln 2}.\frac{V}{I} = 4.35.\frac{V}{I} \qquad (4.1)$$

where 4.35 is a tooling factor depending on the dimensions of the probes used. For my wafers, the typical voltage measured across the two outer probes is 11 mV, with an inner probe current of 100 μA so the calculated sheet resistance is approx. 500 Ω/sq. With this known quantity, we can calculate the resistivity as follows:

$$\rho = R_{sheet}.t \qquad (4.2)$$

where ρ is the resistivity of the wafer and t is the wafer thickness value. For our wafers with their thickness of 180 μm, the resistivity is 9 ohm.cm which is well within the expected value provided by the data sheet with a variation of ± 10 Ω.cm. The main concern here in determining this value is to estimate the doping conditions for the emitter (p-type), the back surface field (BSF, n^{++}) and front surface field (FSF, n^{++}) formation considering the concentration of phosphorous already present into the wafer (n^{+}), so the doping conditions to attain a certain doped layer can be found. For example, wafer with a background (n^{+}) phosphorous doping of 10^{14} will need longer doping time compared to the wafer with background doping of 10^{16} at constant given temperature to achieve a n^{++} doped layer (BSF) of 10^{18} cm^{-3}. The sweep for resistivity and dopant concentration [https://www.pvlighthouse.com.au/resistivity] is determined as 9 Ω.cm resistivity leads to a background concentration value of $5.02x10^{14}$ cm^{-3}.

4.1.2 Wafer cleaning process:

4.1.2.1 Wet chemical cleaning (RCA cleaning)

As-cut wafers from the silicon ingot have damaged surfaces at the micron-scale level. To remove this damage, an alkaline solution is used at high temperature with high concentration.

In our process, we remove the surface damage with the RCA four step wet chemistry process developed at RCA laboratories in 1960 [84]. This process involves (1st step) a 5:1:1 wt. % ratio of alkaline etch solution, made of NH_4OH, H_2O and H_2O_2 at a temperature of 80 ^{o}C to remove all organic contaminations. The 2nd step uses a 1:6 diluted HF: H_2O etchant for 20 to 30 seconds to remove any oxide layer contamination. The 3rd step uses an acidic etch solution consisting of a mixture of HCl, H_2O_2 and H_2O (5:1:1). This step is also known as the ionic cleaning and is useful for the removal of metal ion impurities. Finally, an HF: H_2O clean is performed for oxide removal. Samples are nitrogen gun dried after each step.

4.1.2.2 Thermal cleaning and mask formation

Diffusivity of commonly used dopants is comparatively lower in silicon dioxide than in silicon. Therefore, SiO_2 is an effective mask material against impurities. In a diffusion process, at 1st step, dopant deposits on SiO_2 to form a layer then in 2nd step diffuses into the underlying silicon. So, in the1st step, SiO_2 acts as a masking barrier against impurities in gaseous phase with an effective thickness value. According to theory, SiO_2 thickness is determined as $\sqrt{D.t}$[85] where D is the diffusion coefficient of respective dopant and t is the time. The minimum thickness of SiO_2 required to mask against phosphorous dopant, is 150 nm @ 900 ºC for 60 min. Other parameters, e.g. number of doping steps, gaseous flow and position distance of sample to the impurity source can change this thickness value. I performed an oxidation of Si wafers by a dry oxidation thermal process at 1000 °C for 7 hours aiming for a ~ 275 nm thick thermal oxide to act as a mask for selective area impurity diffusion. This thickness value is selected after a number of trails and this value worked

perfectly as a barrier in multiple doping processes (particularly, in IBCs fabrication) once placed in furnace.

$$Si\ (s) + O_2\ (g) \rightarrow SiO_2\ (s)$$

It is worth noting that the dry oxidation reaction occurs even at room temperature where it forms a native oxide layer of ~ 2 nm thickness. The oxidation process helps to draw metal ion defects from the silicon wafer into the oxide layer which is later removed. A second step aimed at passivating bulk metal impurities and vacancies is to perform hydrogen assisted annealing at the end of the device fabrication process. This step is known as forming gas annealing, which uses a mixture of N_2: H_2. In the forming gas annealing step, hydrogen not only passivates free dangling bonds on the surface, but it also diffuses into the bulk to passivate bulk defects and vacancies. I relate thermal cleaning at the beginning of the fabrication process to the same characteristic to draw impurities from near surface region and is the step of a certain importance to get uniform doped regions.

4.1.3 Thermal doping

Doping is used both for junction formation and for increasing the conductivity on the surface to facilitate contact formation.

Diffusion is a process used for doping where the mass (impurity atoms) is transported by atomic motion. In thermal doping process, a solid is sublimated to activate the diffusion of sublimated species under a concentration gradient which is stated by Fick's 1st law[86].

$$F = -D\frac{dC}{dx} \qquad (4.3)$$

where D (cm^2/sec) is the diffusion co-efficient, F (atoms/ms^{-1}) is the flux of atoms across the planar area per unit time and unit area. The negative sign shows that flux flows from higher to lower concentration.

A detailed dopant distribution is given by the Fick's 2nd law. It describes the change in flux through volume element. Mathematically, Fick's 2nd law is[86]:

$$\frac{\Delta C}{\Delta t} = -\frac{\Delta F}{\Delta x} \tag{4.4}$$

It describes the change in concentration by the change in flux getting in and out of the volume element.

Using 1st law, we can rewrite the 2nd law as follow:

$$\frac{dC}{dt} = \frac{d}{dx}\left(D\frac{dC(x,t)}{dx} \right) = D\frac{d^2C}{dx^2} \tag{4.5}$$

For a given case, when a constant source is present near the silicon surface, the analytical solution of the Fick's law in equation 4.5 is governed by the complementary error function (the diffusion profile):

$$C(x,t) = C_S erfc\left\{ \frac{x}{2\sqrt{Dt}} \right\} \tag{4.6}$$

where C_S is the surface concentration (atom.cm^{-3}) and $\sqrt{Dt}$ (cm) is the diffusion length with a junction depth x (cm).

The doping process introduces impurities into the crystalline structure of the semiconductor to alter its electrical properties, using either p- or n-type dopants. These dopant atoms are introduced at high temperature. I use a Carbolite furnace fitted with a quartz tube designed to operate wafers at high temperature (max. 1200 °C). Each dopant source has its specific tube to avoid intermixing and the system is connected to gas flow valves. In all thermal processes, we use a nitrogen flow rate of 0.5 sL/min.

4.1.4 Boron doping process

A pn junction is formed in the solar cell to separate and collect charge carriers that have been generated by the incident light. Boron and Aluminium, as group III elements, are the

commonly used p-type dopant in silicon while phosphorous (group V) is typically used as the n-type dopant. The solubility of these elements is very high (of order 5 x 10^{20} atoms / cm^3) at a temperature range between 850 °C to 1100 °C. We use solid state sources, namely ceramic wafers loaded with boron nitride (BN) and phosphorous pentoxide (P_2O_5). The wafers are placed in the diffusion furnace with the silicon wafers and doping occurs in the gas phase. The Boron wafer has a composition of 3.5-6.5 % B_2O_3 (Grade BN-975, Saint Gobain).

Source preparation step: The doping source (BN) needs to be activated by placing it into the furnace under inert atmosphere and drying at 400 °C to remove all entrapped moisture. This step is followed by oxidation at 975 °C, which grows a thin layer of B_2O_3 on the surface of the dopant wafer. After 30 minutes, the ambient is changed from oxygen to nitrogen and the temperature is increased to 1000 °C for 30 mins to stabilise the source, illustrated in Figure 4.2 (a). The reaction from boron nitride to boron oxide can be described as follows;

$$2BN(s) + 3O_2(g) \rightarrow B_2O_3(s) + N_2(g)$$

I found the reproducibility and homogeneity of the doped layers to be significantly improved with the source preparation step which we introduced at the later stage of our process.

Once the source is prepared, the temperature is cooled down to a temperature of 750 °C to place the sample into the furnace by facing one another. Now the temperature cycle is set as a function of time, shown in Figure 4.2 (b). At an activation temperature of 975 °C, B_2O_3 sublimates to provide dopant atoms. These atoms accumulate at the clean silicon surface and diffuse into the bulk silicon, following Fick's law of diffusion.

During the diffusion process, boron is released upon reduction of the B_2O_3 by silicon and it is then driven into the silicon substrate.

$$2B_2O_3(l) + 3Si(s) \rightarrow 4B(s) + 3SiO_2(s)$$

$$B + 3Si \rightarrow \text{p-type Si}$$

4.1.5 Phosphorous doping process

For the phosphorous doping, a phosphorous solid source (grade-975) was used. The P_2O_5 source preparation step only involves the drying step at 400 °C for 60 min and does not require the oxidation process, illustrated in Figure 4.3. Phosphorous pentoxide (P_2O_5) reacts with the silicon lattice at high temperature according to the following reaction:

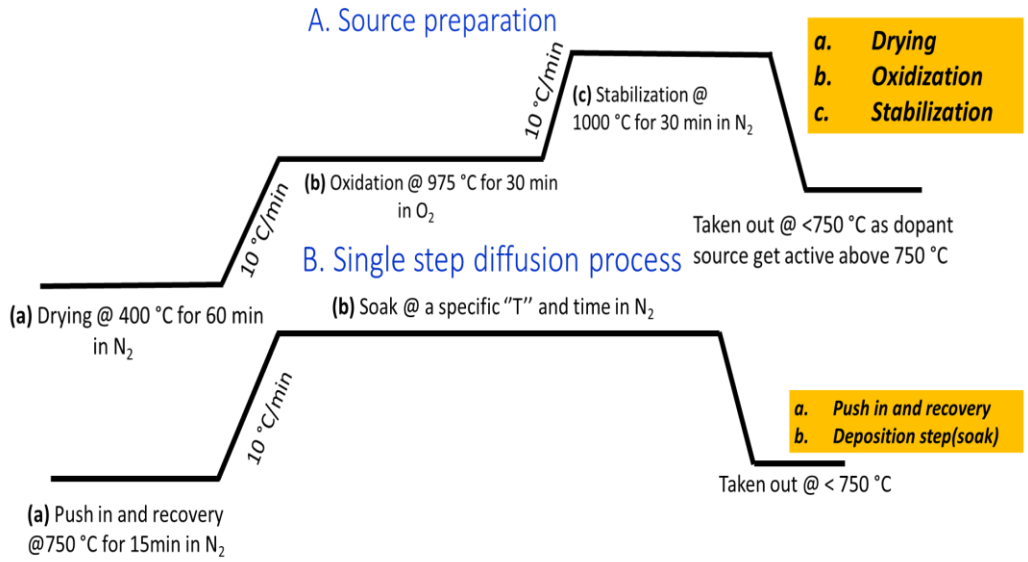

Figure 4.2. Doping scheme for p-type doping. (a) BN dopant source preparation. (b) Diffusion process conditions.

$$2P_2O_5(l) + 5Si(s) \rightarrow 4P(s) + 5SiO_2(s)$$

$$P + 3Si \rightarrow \text{n-type Si}$$

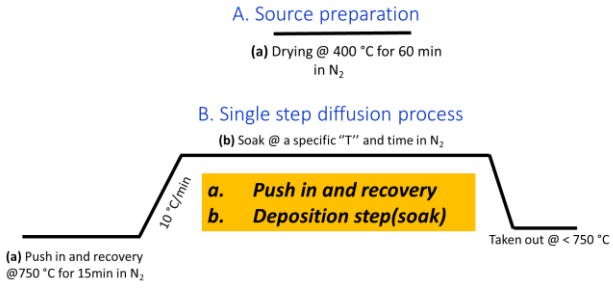

Figure 4.3. Doping scheme for n-type doping. (a) Phosphorous dopant source preparation. (b) Diffusion process conditions.

4.1.6 Phosphorous/ Boron glass removal

Depending on the nature of the doping process, a thin layer of boron glass silicate (BGS) or phosphorous glass silicate (PGS) forms on the silicon surface. This layer must be removed before proceeding, which is done via a 40 second bath in HF. In case of BGS, which forms a thin brown “dead layer”, removal is more difficult. The dead layer is full of defects and raises the contact resistance at the metal-silicon interface. The defects also act as recombination sites for light induced charge carriers and significantly lower the collection probability. To effectively remove the dead layer, another low thermal oxidation process is introduced at 750 °C. This oxidation step is performed for 20 minutes after which the HF bath effectively clears the surface, schematic is shown in Figure 4.4.

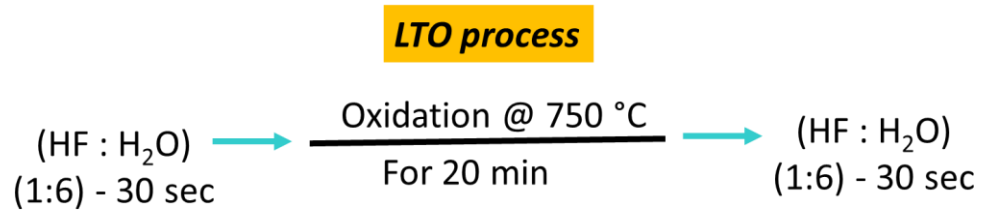

Figure 4.4. Recipe used for Low thermal oxidation (LTO) process.

4.1.7 Edge isolation

The isolation of the wafer edge is a necessary step to prevent the formation of shunt current paths. During the various doping processes, the wafer edges are exposed to all impurity types, making them more conductive so current can flow along the wafer edges. To block these shunt paths, the front and back surfaces of the device need to be isolated. Such edge isolation can be implemented by laser scribing, plasma etching or wet chemical etch processes. We use plasma reactive ion etching to create recesses on the surface and to block any possible current flow. A similar same step is used to isolate the doped interdigitated fingers in the IBC cell design. The possible current paths in etched structures are shown in Figure 4.5, before and after edge isolation step. I use typical etch depth of 500 μm.

For the reactive ion etching process I used a SF_6 / CHF_3 plasma at a power of 22 W. The plasma produces F* radicals which are accelerated to the silicon surface by a DC bias of 180 V. The Fluorine radicals react with the silicon to produce SiF_4, which is volatile and removed by the pumping system.

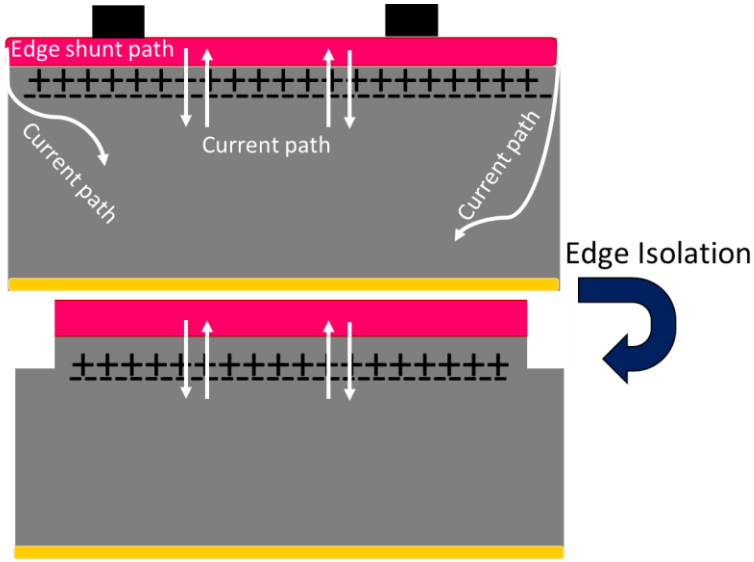

Figure 4.5. Illustration of possible paths for current flow, before and after edge isolation step.

4.1.8 Surface passivation:

As the surface velocity of the minority charge carriers is crucial for controlling the surface recombination discussed in chapter, section 3.7.1. Commonly, two complementary approaches are used; one way is to reduce the trap density at the surface by passivating these states, while another is to reduce the excess minority charge carrier concentration ($p_{surface}$ or $n_{surface}$) by introducing a high doping concentration that acts as a barrier for minority carriers at the surface. This method is called surface field passivation and significantly applicable to the back surface of FB device to create lower defect density at the metal / Si interface. We use both methods.

First, we introduce an n^{++} layer at the back surface by thermal diffusion of phosphorous. This step creates an electric field at the n^{+}/n^{++} interface which acts as a barrier for the minority

carriers (i.e. the holes) in the n-type region and stops them from diffusing to the back surface where the minority carriers are repelled from the concentration gradient at the back surface.

Second, I perform a chemical passivation step at 850 °C for 30 minutes in O_2 atmosphere. This step generates a 12 nm thin SiO_2 layer which draws out many of the surface defects.

4.1.9 Sputtering deposition of SiO_2 layer as an ARC

Sputtering is a widely used technique in the semiconductor industry for the deposition of various metallic and dielectric thin films. Our sputtering setup uses a pulsed DC magnetron configuration to support both conducting and dielectric film deposition and consists of a vacuum chamber and a substrate holder (anode) parallel to the target (cathode). A plasma is generated by injecting argon into an oscillating electromagnetic field between the two electrodes; the argon is ionised and accelerated towards the target holder (cathode) with sufficient momentum and kinetic energy to dislodge the target atom clusters. The sputtered clusters travel through the chamber until they condense on the sample surface. Other gases such as nitrogen or oxygen are introduced to form nitride and oxide films, respectively. Here, we deposit SiO_2 as an anti-reflection coating for our silicon solar cells with an optimized thickness value of 80 nm.

4.1.10 . Contact metallization process

4.1.10.1 Front surface contact grid:

We use aluminium and silver for the metal contacts, which are deposited by evaporation in a vacuum chamber (Mantis plc). For the FB-type device, an Ag/Al stack is deposited on the entirety of the back surface, while a pattern of narrow fingers is used on the front surface. This grid at the front provides a uniform coverage for charge collection while also allowing light to enter to the front surface of the silicon device. The finger pattern is produced by photolithography using a lift-off process. The pattern is designed by considering the lateral and the series resistance and the pattern is a compromise between conductivity and shading, as I discuss next.

As the metal/Si interface is an area with high defect density, it is a good idea to minimize the front contact area, naturally also in terms of reducing optical shading. The layout of the front contact consists of a busbar which connects all the fingers. The resistance R_{finger} is the resistance of metal contact finger, it increases with length (l) and decreases with cross-section (*wh*) as per the standard relation:

$$R_{finger} = \rho \frac{l}{wh} \tag{4.7}$$

In terms of the equivalent circuit of a solar cell, the contact resistance contributes to the series resistance of the circuit and a high series resistance leads to a low fill factor of the solar cell. So, it is important to create relatively thick fingers. Another parameter to consider is the metal finger spacing while designing a metal grid, as the carrier has to travel laterally in the emitter to be collected; excess spacing also increases the series resistance[3].

In order to balance these effects, we have designed the contact fingers with a width 100 μm with thickness of 1.5 μm and the finger spacing (space distance between two consecutive fingers) is 2000 μm covering over the given front surface of the device.

4.1.10.2 Photolithography

To transfer the desired pattern from the mask to the silicon substrate, a photo-resist layer is illuminated under ultra-violet (UV) light. UV light chemically changes the nature of the resist and its solubility in a developer. We use the positive resist S1818, spins at 4000 rpm for 60 sec and soft-baked at 95 °C for 120 sec. The process schematic is shown in Figure 4.6 (b). Exposure makes S1818 more soluble, so the developer removes all exposed areas. Further HF cleaning, metallization or RIE transfer methods are performed depending on the processing requirement.

4.1.10.3 . Alignment Techniques

A Karl Suess MJB-3 mask aligner shown in Figure 6 (a) is used to conduct the photolithography process. The MJB-3 is a contact mask aligner whereby the mask is pressed

on to the substrate to achieve a pattern transfer when illuminated with a UV source (here, we use an array of high power GaN LEDs). In case of the IBC processing, a number of lithography steps are involved and reference marks are included to ensure high precision alignment between subsequent layers.

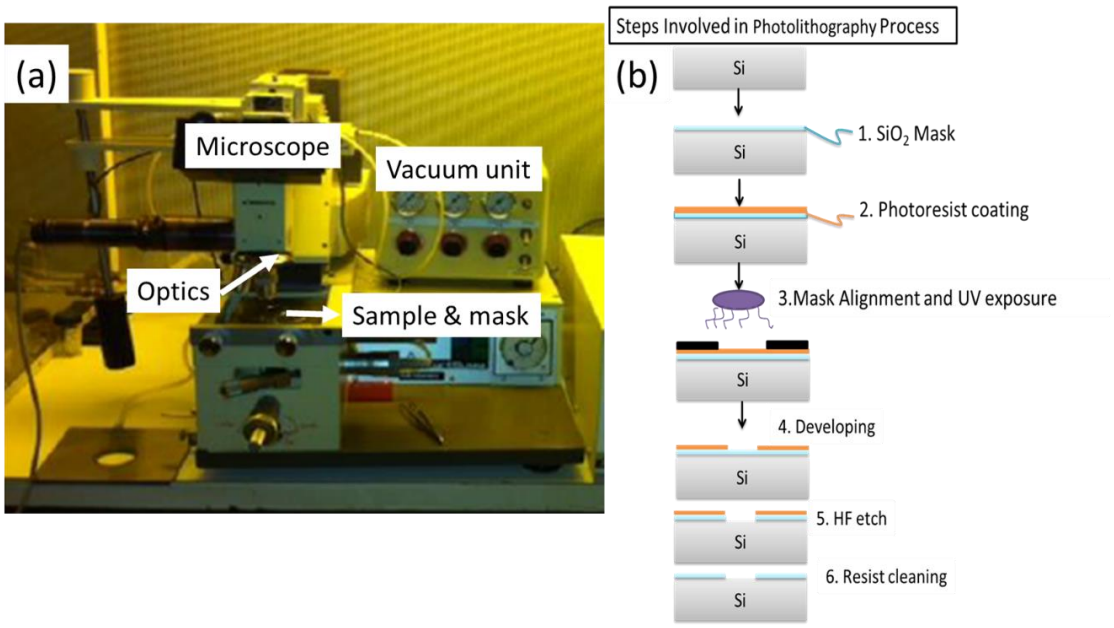

Figure 4.6. Photolithography technique. (a) Mask aligner setup (b) Flow process illustration.

4.1.10.4 . Exposure and Developing conditions:

After exposure to UV- light, the resist is lifted off using the developer MF-319. An overall accuracy of ±10 μm is estimated, which may depends on positioning of mask over the patterned silicon surface. Both the exposure and developing times are 2 minutes.

Aluminium is used for the metal contacts which are deposited by evaporation in a vacuum chamber. For the front back type of device, Al is deposited on the entirety of the back surface, while a pattern of narrow fingers is used on the front surface. The finger pattern is produced by photolithography using a lift-off process. After lift-off, metal contacted samples are annealed at 180 °C for 40 minutes for improved metal conductivity. These annealing conditions are carefully chosen, as high temperature may promote Al diffusion to the back BSF layer and can cause leakage current.

4.2 Interdigitated back contact (IBC) solar

4.2.1 Why IBCs?

A major drawback of traditional FB crystalline Si solar devices is the optical shadowing loss that occurs because of the front metal contact grids. This loss becomes worse when a series of solar devices are connected together to form a solar module. Moreover, the presence of metal strips on the same front surface restricts our degree of freedom in terms of applying optical techniques, such as light trapping nanostructures. To overcome these issues, the interdigitated back contact (IBC) design was suggested by Schwartz and Lammert in 1975 [87] where the front surface was metal free to avoid optical shadowing[88]. In the IBC architecture, both the junction and the metal contacts are placed on the rear side in an interdigitated finger pattern. IBC solar cells have been commercialized by SunPower and they exhibit efficiencies as high as 25%[89][90] IBCs are multi-junction devices whereby the electrons and holes are collected at multiple pn- junctions on the backside of the wafer. Here, the motivation for using IBCs is that light trapping structures can be implemented across the entire front surface of the device.

4.2.1.1 Wafer type, quality and thickness of silicon for IBCs

Commercial IBC devices are made of n-type monocrystalline silicon wafers; n-type is used because n-type wafers typically contain fewer impurities such as boron and oxygen, which give rise to unwanted carrier recombination. The growth process of the silicon wafer determines its quality. Float zone (FZ) method is used to control contaminations in the wafer, particularly oxygen and carbon (typically, below 10^{15} cm^{-3}) as the liquid silicon does not come into direct contact with that of the quartz crucible in this method. This results in crystals of high quality (high lifetime, > 1 ms). Wafer quality is determined by lower bulk recombination rate. As the photo generated charge carriers have to travel all the way to the rear of the wafer, to be collected at contacts.

Clearly, the thickness of the wafer should not exceed the diffusion length and, ideally, the diffusion length should be much larger than the wafer thickness in order to ensure that most of the carriers are collected. Practically, the directly measurable quantity is the carrier's lifetime. The optimal wafer thickness plateau is shown over the range of 160 to 280 µm for IBCs given by McIntosh et al as shown in Figure 4.7. These results are based on simulation and experimental agreement.

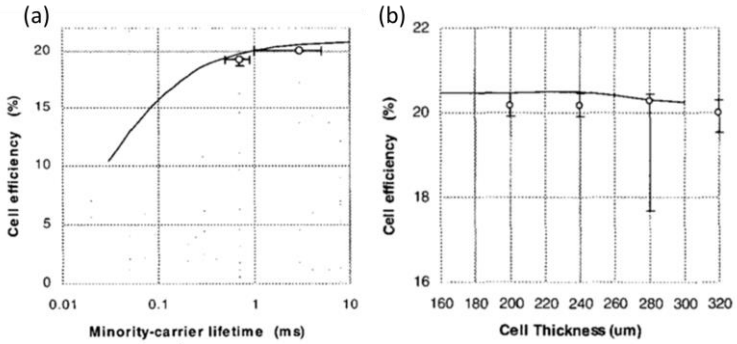

Figure 4.7. IBCs solar cell efficiency dependence on (a) Minority carrier lifetime. (b) absorber layer thickness.

[91] Keeping in mind these facts, I have chosen 180 µm thick FZ silicon wafers with a lifetime of 1.2 ms.

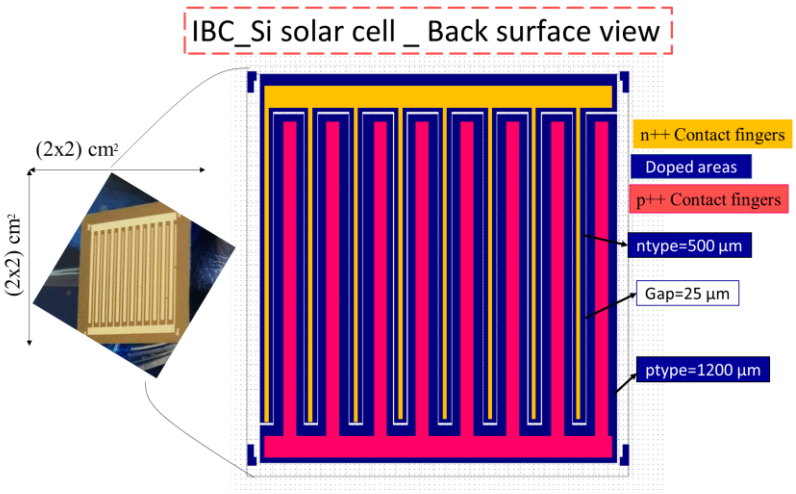

Figure 4.8. Mask designs at the rear surface of the IBC device realized on (2*2 cm^2) area.

A design of an IBC solar cell with a surface view of a real device is shown in Figure 4.8, as fabricated in our lab. The layout design for the contact fingers at the back of the cell needs to

minimise the series resistance and the creation of local defects; the larger the contact fingers, the more defects are created by the metal contacts while the series resistance is reduced commensurately. This significance is due to the lateral transport mechanism in IBCs compared to FB devices. A current flow schematic in IBCs is shown in Figure 4.9, which highlights the combination of wafer thickness and finger spacing in the transport path. Therefore, it is even more important to use high quality wafers with long carrier lifetimes for IBCs.

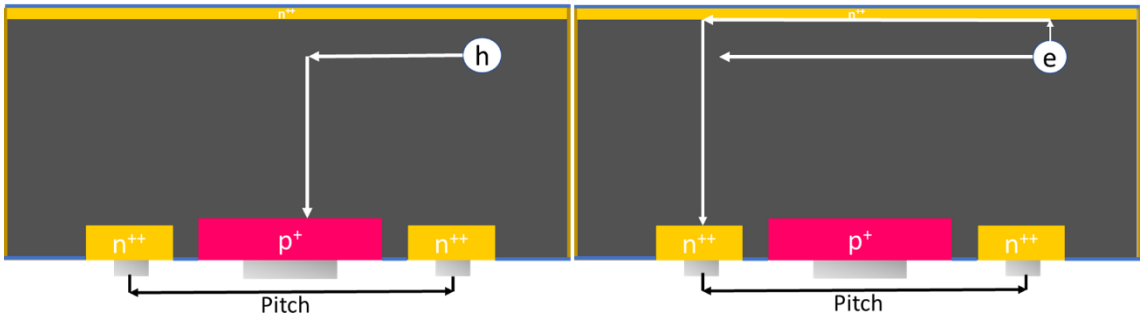

Figure 4.9. Illustration of charge carriers flow in IBCs solar cell.

I used a designed mask with a high emitter coverage with each finger width of 1200 µm while keeping the BSF (n^{++}) finger width at 500 µm. The metal contact area is adjusted at a deposition fraction of 50% (< 50% offers high series resistance in my devices) design. The undoped area between two opposite polarity fingers is kept constant at 25 µm.

The doping areas and metal contacts are then realized by three photolithography steps defining emitter coverage, BSF fraction area and the metal contact area. An example of a fabricated structure is shown in Figure 4.10.

4.2.2 Fabrication steps in IBCs solar device

Following the same wet-chemical cleaning process used for the FB fabrication, a p-type boron diffused uniform emitter is applied on the back side of the wafer. The n- and p-type doped fingers are patterned using photolithography masks. Firstly, the emitter finger pattern

is transferred on the already doped emitter layer surface and the pattern is back etched using reactive ion etching (RIE) to avoid shunts. This step not only isolates the emitter fingers from the edges of the wafer but also provides patterned fingers for n-type doping. The diffusion process for the n-type fingers is followed by a barrier oxide deposition (we use flowable oxide, i.e. spin-on glass, see below) to protect the previously doped p-type fingers. The front side of the silicon wafer is passivated by thermally grown oxide SiO_2 film and a diffused n^{++} FSF.

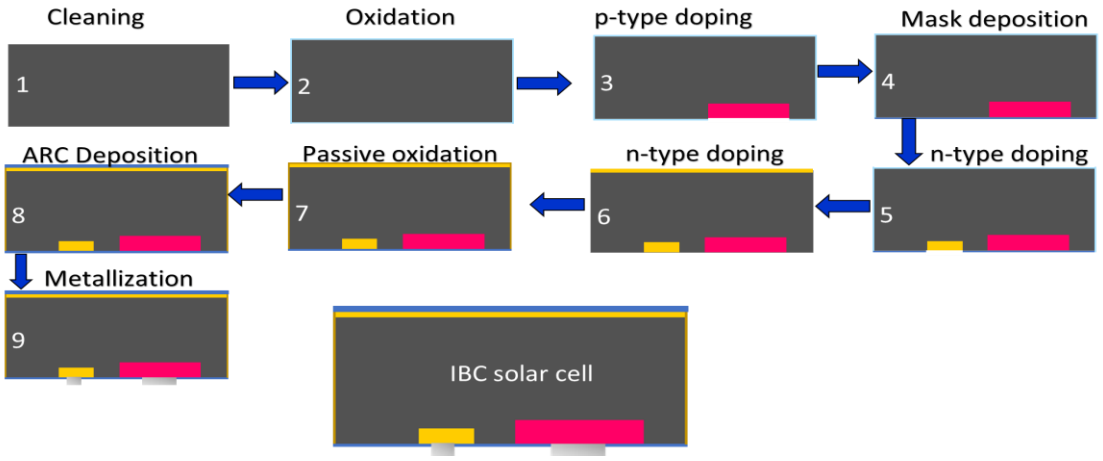

Figure 4.10. Fabrication process of IBCs silicon cell devices.

4.2.3 Masking layers for Junction formation and edge isolation

A key issue for the IBC devices is to ensure good electrical isolation between the p- and n-type contact fingers, to avoid shunts. As the p- and n-type doping is performed on the same side of the wafer, it is important to include suitable diffusion barrier materials. We identified spin-on glass (flowable oxide FOx, Dow Corning) as such a barrier material. We tested it against both phosphorous and boron diffusion and found that it worked well for masking against the phosphorous source. In the case of boron, the FOx readily mixed with the boron glass silicate (BGS) and did not provide a good barrier. Therefore, we adjusted the fabrication sequence such that we only required a barrier against phosphorous doping in all fabrication process. I also tested sputtered silicon nitride but found that it did not to provide suitable masking.

4.2.4 IBC metallization process

The metallisation of the doped fingers is provided by a thermally evaporated aluminium (Al) film of 1 μm in thickness, followed by lift-off in acetone. It is important to note in this context that any inadequacy in the cleaning processing, the thermal doping process, the ARC deposition and the edge isolation may deteriorate the performance of the device. The contacts are annealed at 180 °C; a lower temperature increases the series resistance while a higher temperature leads to shunted junctions.

4.3 . Fabrication of light trapping structures

For light trapping in solar devices, the State-of-the-Art is to use pyramid structures. Therefore, I have also implemented textured pyramid surfaces on my devices. Furthermore, I conducted a comparison with quasi-random (QR) nanostructures both in terms of the J_{sc} and V_{oc}. The QR concept was published by my group in 2012 and it numerically demonstrated the most effective light-trapping enhancement in thin-film (1 μm) silicon as shown in Figure 4.11. The quasi-random structures appear random but possess a unit cell which is repeated periodically. QR nanostructures are designed to enhance high diffraction orders and suppres the lower orders of the Fourier spectra in order to enhance light absorption. The structures are fabricated directly using electron beam lithography (EBL).

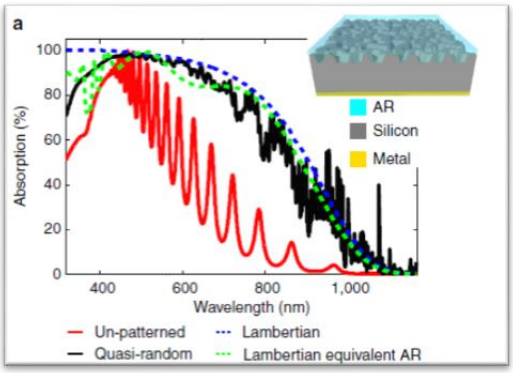

Figure 4.11. Comparison of absorption spectra of 1 μm thin silicon under different trapping structures[92].

4.3.1 Electron beam lithography

Electron beam lithography (EBL) is a specialized technique to create extremely fine patterns down to a few nanometres in size. EBL is an extension of scanning electron microscopy (SEM), which was developed in late 1960s. In brief, EBL uses a focused beam of electrons to scan a surface coated with a resist; the resist is sensitive to the exposed electrons and the exposed area becomes more soluble to the developer. The beam is generated in a column, focussed by electromagnetic lenses and deflected electrostatically. There is a chamber facilitating the stage for loading, unloading and moving the sample. A vacuum system is associated to the chamber section for the maintenance of a pressure at $\approx 10^{-9}$ mbar. The beam is controlled by a computer and it generates the pattern in a raster-scan fashion.

To implement our QR structures the sample is spin-coated with an ebeam resist (CSAR-62-AR-P 6200.09 ALLRESIST GmbH). The spin speed is kept at 2000 rpm for 60 sec and the sample is hard baked at 180 °C for high quality adhesion of resist to the substrate. After completing the resist-coating step, samples are loaded to the e-beam main chamber. As the sample is positioned into the chamber, the ebeam current, spot size, exposure dose, time, beam stigmation and alignment parameters are set according to the recipes previously determined by other members of the group colleagues [93].

The QRS were designed by other group members using direct binary search algorithm-details can be found in reference[94]. After patterning the ebeam resist, the development process is performed with Xylene solvent at room temperature for 20 minutes. The developing processes is quenched by a final IPA wash, as shown in Figure 4.12 (b).

4.3.2 QR transfer methods

Once the resist has been patterned, I transfer it into the silicon material by using either dry or wet etching. In the dry etching process, the patterns are etched using reactive ion etching whereby the resist can be used directly as the mask. Alternatively, I use wet etch, which dissolves the silicon using an alkaline solution. As the alkaline solution tends to be very

corrosive, an additional SiO_2 layer is thermally grown to act as a hard mask because the ARP resist is not able to withstand the etchant.

4.3.2.1 Dry etched QR

CF_4 gas is typically used to generate fluorine free radicals (F*) for etching away the silicon material.

$$e^- + CF_4 \rightarrow CF_3 + F^* + e^-$$

$$4F^* + SiO_2 \rightarrow SiF_4 + 2O$$

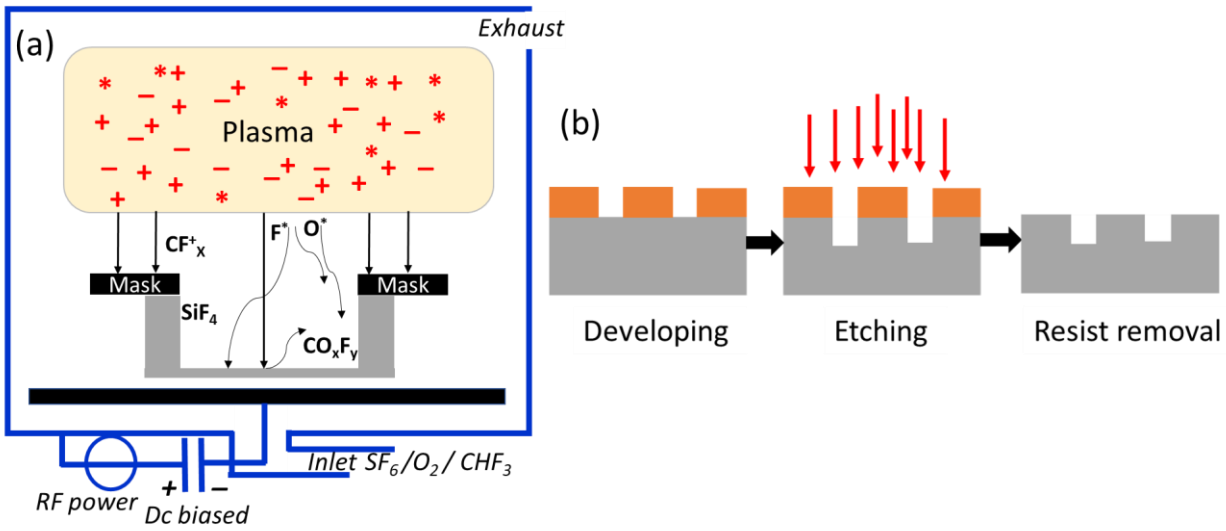

Figure 4.12. (a) Basic schematic of reactive ion etching system. (b) RIE flow process to etch the silicon surface.

As shown above, silicon is removed by reacting with fluorine radicals to form SiF_4, which is volatile. Dry etching offers high dimensional control thus gives faithful transfer of features into the silicon substrate with well-defined vertical walls. This fidelity is due to the combination of chemical etching and ion bombardment, the ratio of which can be controlled by the etching parameters. The recipe is optimized as follow: CHF_6 gas; 14.5 sccm, SF_6 gas 12.5 sccm and 22 V, ~180 W.

4.3.2.2 Wet etched QRS

Since dry etching causes surface damage and thereby increases the recombination rate, wet etching should be considered as an alternative. I use a TMAH solution (25% in water) at 80 °C, which gives a typical etch rate of 1000 nm/min.

4.4 Light trapping structures characterization

4.4.1 Absorption Measurement setup

Absorption measurements are performed using an integrating sphere (4 inch, Labsphere) and reflection and transmission measurements were performed simultaneously. The sample is placed at the centre of the sphere and the photodetector is directly mounted onto the exit port, as shown in Figure 4.13. As the light interaction is strongly wavelength dependent, I chose a monochromator (Omni-λ150, Gilden) to take measurements as a function of wavelength.

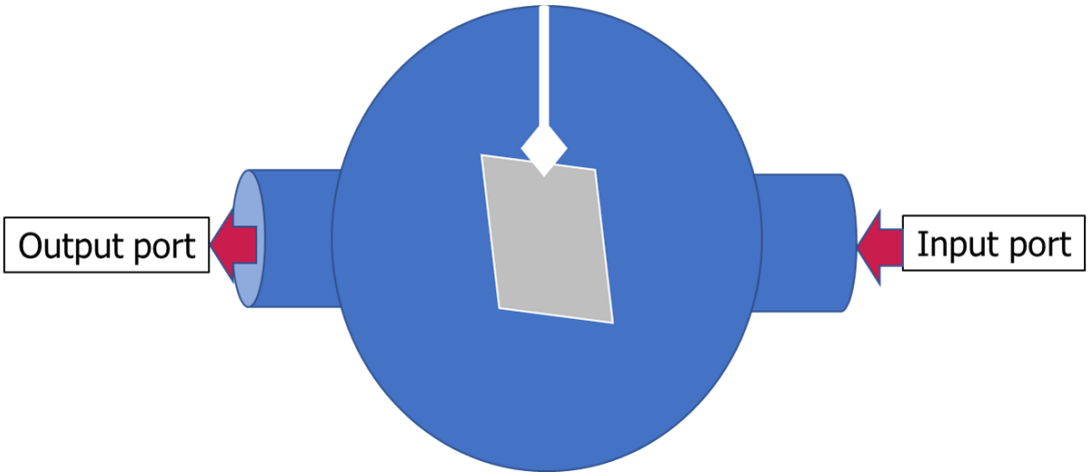

Figure 4.13. Sample placement in an integration sphere in an absorption measurement setup.

A Thorlabs halogen light source is used for illumination, mounted at the entrance of the monochromator. The optical power spectrum covers the visible spectrum (between 400 – 1100 nm) as required by the silicon material. The monochromator has an optical resolution of sub-nm [0.1 nm]. To block harmonics at longer wavelength (i.e. second order diffraction), short pass filters are used. An amplified silicon detector (type PDA100, Thorlabs) of femtowatt noise floor and fixed gain is attached to the sphere's exit port and is read using a

Keithley 2400 digital multimetre (DMM). All components in the setup are virtually controlled via Labview. The sample is placed at the centre of the sphere and the photodetector is directly measures onto the exit port, as shown in Figure 4.13.

4.4.2 Morphology analysis

To image the textured patterns, scanning electron microscopy (SEM) is used **(**field emission SEM JEOL FE-SEM 7800). While the SEM provides 2D information of a scanned area, it cannot measure the depth profile of a textured surface in top view. Usually, atomic force microscope (AFM) is used to provide such topography information. An AFM generates an image by scanning an atomically sharp tip to record very small features. Along with the feature size, it also determines the roughness at the surface. The tip is positioned at the end of a cantilever and the bending or deflection of the cantilever is recorded by a laser beam deflecting from the back of the cantilever. I use a Bruker BioScope Resolve.

4.4.3 Opto-Electrical characterization setups

In this section, I illustrate the measurement set-up for the opto-electrical analysis of fabricated devices.

4.4.3.1 External Quantum Efficiency (EQE)

The EQE is the ratio of incident photons to the number of collected charge carriers and it is wavelength dependent. The EQE describes how well the device converts solar energy into current; at a given wavelength, the EQE is ideally unity if all the incident photons are absorbed and the free charge carriers are collected. When a solar cell is illuminated, the resulting photocurrent at zero biase is known as J_{sc}. This measurement is conducted as a function of wavelength and the integration of the spectrum gives $J_{sc\ (calculated)}$. This $J_{sc(calculated)}$ is comparable to the $J_{sc(measured)}$ value measured from the JV-characteristic. An EQE-setup is also referred to as a spectral response setup and an example is shown in Figure 4.14.

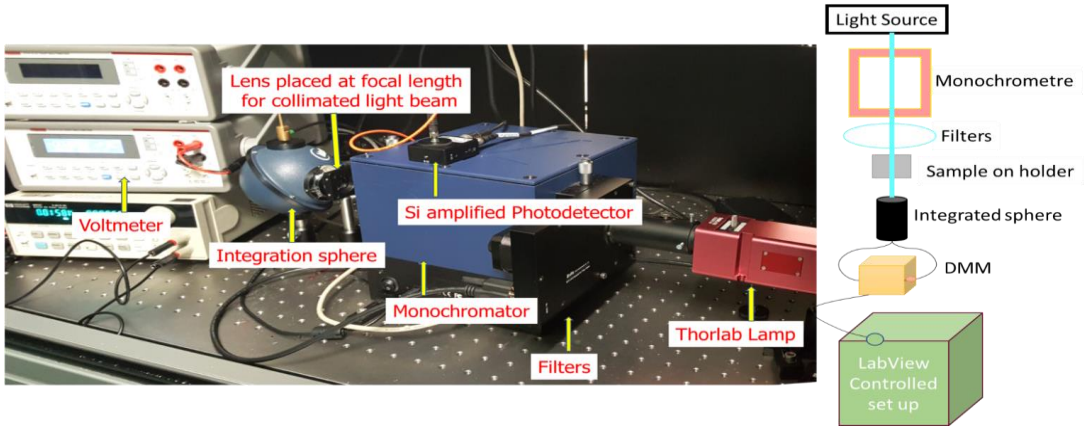

Figure 4.14. Illustration of components in external quantum efficiency measurement setup.

The measurement proceeds as follows: The light source is placed at the entrance slit of the monochromator and a sample holder is attached directly to the exit port. The lenses are used to focus and shape-up the incoming collimated light into a rectangular band of (5 x 2) mm.

The responsivity (R) quantifies the current output of a device for a given incoming optical power.

$$\Re = \frac{Current\ (A)}{Incident\ Optical\ Power\ (W)} \tag{4.8}$$

The current signal from the solar cell is measured with a pico-Ammeter (Keithley 2400 DMM). All the components are synchronized and controlled using Labview. I chose a step size of $\Delta\lambda$=10 nm because the spectral response of the cell changes slowly with wavelength. As the spectral responsivity $\Re_{Ref.\ Diode}$ of the reference diode (FDS1010) is known, the reference diode current $I_{\mathrm{Re}f.Diode}$ can be used to determine the $P_{incident}$.

$$P_{incident}(\lambda) = \frac{I_{\mathrm{Re}f.Diode}}{\Re_{Ref.\ Diode}} \tag{4.9}$$

The incident optical power is determined for each wavelength and we can calculate the EQE as:

$$EQE = 1240 \times \frac{\Re_{Device}}{\lambda} \tag{4.10}$$

where

$$\frac{hc}{q} = \frac{6.626068E^{-34} \times 299792458 \times 1000000000}{1.602E^{-19}} = 1239.9 \sim 1240$$

where $\Re_{Deivce}$ is the responsivity of the device at zero bias.

4.4.3.2 Current Density – Voltage (JV) Characteristic setup

The power conversion efficiency (PCE) is the most relevant figure of merit for solar devices. The PCE is determined by the ratio of the power generated by the device to the incident power. The standard testing conditions for illuminating device used are (AM1.5; 100 W/cm^{-2} solar spectrum; $T = 25$ °C). The reference solar spectrum ASTM G173-03 is used to determine the conversion efficiency of a solar device and the setup is is shown in Figure 4.15 As we do not have a calibrated light source available, we compare the measurements to a reference solar cell of known efficiency. The two cells are placed in front of a lamp at an approximate intensity is 100 mW /cm^2. The IV data is recorded using an Agilent semiconductor analyser.

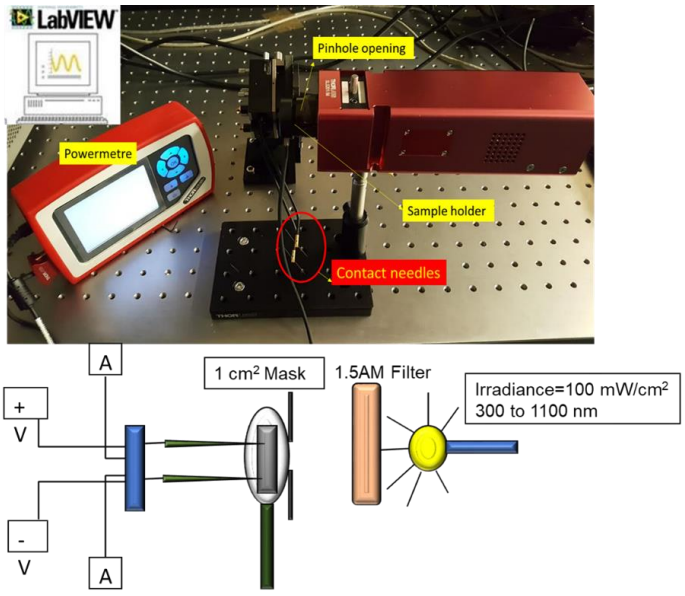

Figure 4.15. Illustration of components in current- voltage characteristic measurement setup.

The parasitic resistances are also determined from the IV-characteristics under illumination conditions, in particular the series and shunt resistances as shown in Figure 4.16. Let us consider the diode equation by taking parasitic resistances into account:

$$I = I_{sc} - I_o(e^{\frac{q(V+IR_{series})}{K_BT}} - 1) - V + \frac{IR_{series}}{R_{shunt}} \tag{4.11}$$

For the series resistance calculation, we assume that R_{shunt} is very large compared to R_{series}, so the R_{shunt} term can be neglected and we obtain:

$$I = I_{sc} - I_o(e^{\frac{q(V+IR_{series})}{K_BT}} - 1) - V \tag{4.12}$$

By solving this equation for the voltage:

$$V = \frac{K_BT}{q}\ln(\frac{I_{sc} + I_o - I}{I_o}) - IR_{series} \tag{4.13}$$

Then differentiating with respect to I :

$$\frac{dV}{dI} = -\frac{K_BT}{q}\ln(\frac{1}{I_{sc} + I_o - I}) - R_{series} \tag{4.14}$$

At neighbouring open circuit condition (at point A): ($V \approx V_{oc}$, $I \approx 0$), we can write:

$$R_{series} = -\frac{dV}{dI}\bigg|_{V=V_{oc}} - \frac{K_BT}{q}\ln(\frac{1}{I_{sc} + I_o})$$

$\frac{K_BT}{q}$ is the thermal voltage which is typically 25 mV, so it is much smaller than the typical $V_{oc.}$ of 0.5-0.7 V, so it can be neglected and we can approximate R_{series} as the inverse slope of IV-curve.

$$R_{series} \approx \frac{dV}{dI} \tag{4.15}$$

Similarly, we can approximate shunt resistance if R_{series} is assumed to be small. We can then write equation 4.13 as:

$$I(V) = I_{sc} - I_o(e^{\frac{qV}{K_BT}} - 1) - \frac{V}{R_{shunt}} \tag{4.16}$$

By differentiating this expression with respect to the voltage, we get

$$\frac{dI}{dV} = -\frac{q}{K_BT}I_o e^{\frac{qV}{K_BT}} - \frac{1}{R_{Shunt}} \tag{4.17}$$

At neighbouring short-circuit condition (at point B): (V≈0 and I≈I_{sc})

So

$$\frac{1}{R_{shunt}} = \left.\frac{dI}{dV}\right|_{V=0} + \frac{qI_o}{K_B T} \tag{4.18}$$

If R_{shunt} is very large then I_o is very small , we can neglect the $\frac{qI_o}{K_B T}$ factor and approximate as follows:

$$\frac{1}{R_{shunt}} = \left.\frac{dI}{dV}\right|_{V=0} \tag{4.19}$$

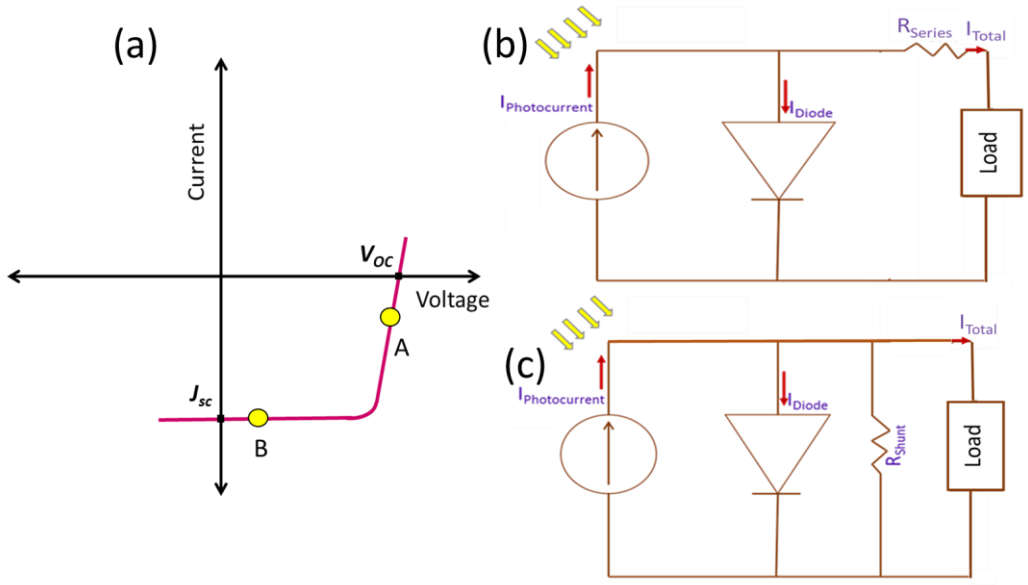

Figure 4.16. (a) Graphical representation of an IV- characteristic curve under illumination where two operational modes are represented by point A and B (b) An equivalent circuit for an ideal solar under load condition to calculate series resistance at point A. (c) An equivalent circuit for an ideal solar cell to calculate shunt resistance at point B.

These characterisation techniques are used in next chapter.

5 Chapter 5: Optical and electrical characterisation of silicon solar cells with light trapping structures.

This chapter covers the results of my work on light trapping structures integrated into real solar cells. In the first section, light trapping structures are textured into the silicon substrate and are characterized in terms of their morphology. In the 2nd section, solar cells (both with front-back (FB) and with interdigitated back contacts (IBCs) are optimized and characterized. Finally, light trapping structures are integrated into the devices and are analysed both optically and the electrically, i.e. for absorption, external quantum efficiency and overall device efficiency.

5.1 Section A:

5.1.1 Light trapping structures

5.1.1.1 Wet etched quasirandom (QR) structures

The initial aim of the study was to fabricate tapered QR structures, where a QR structure is defined on the surface and wet etched into the substrate. The hypothesis was that a tapered structure should give a more gradual index variation between air and semiconductor thus resulting in better in anti-reflection properties. Figure 5.1 gives a schematic illustration of the process. The silicon wafer is first cleaned and thermally oxidised for produce a SiO_2 mask for the wet etching process. The SiO_2 layer is ~ 12 nm thick by oxidation at 850 °C for 25 min. This process is followed by the deposition of an ARP resist, which is spin coated at 2000 rpm for 60 sec. The ARP resist layer is hard baked at 200 °C for 10 min, followed by e-beam writing and the developing steps (detailed in the experimental chapter).

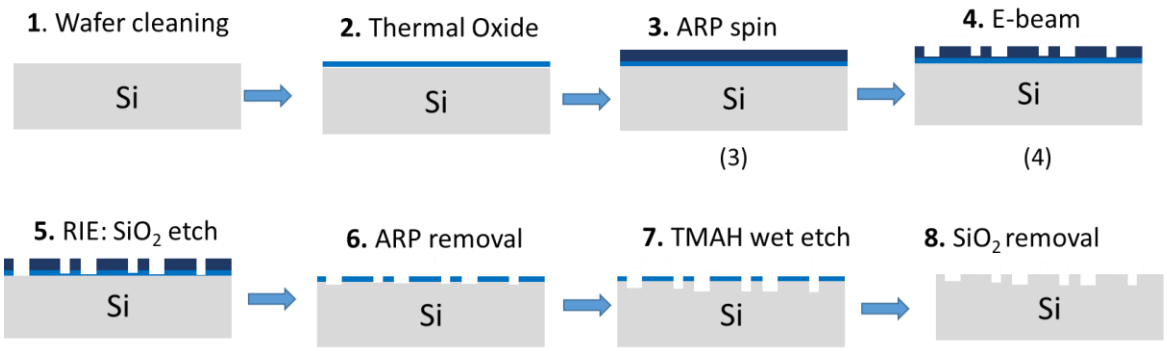

Figure 5.1. Schematic of fabrication process of light trapping QR structures into silicon substrate.

5.1.1.1.1 SiO_2 mask (over- under) etch process

The next step is to etch away the SiO_2 mask under the developed pattern using RIE. Here, it is important to note that the SiO_2 mask should be over-etched rather than under-etched, as shown in Figure 5.2 (a,b). If the mask is under-etched, a thin film of SiO_2 may remain which will obviously stop the wet etching process. An SEM image is shown in Figure 5.2 (c), where the contrast area shows a difference of SiO_2 (masked) and Si (un-masked) surfaces. The RIE etch recipe to etch SiO_2 is optimized as: CHF_6 gas; 60 sccm, DC bias 120 V, ~700 W, 3.5 min.

5.1.1.1.2 Optimisation of wet etch conditions

The temperature of the wet etch process is a crucial parameter, both for etch rate and morphology. Initially I aimed for tapered structures, these require a higher process temperature, above 80 °C, but a shorter etch time of 2 min. Results are shown in Figure 5.3. (a), (c). where two structures show tapered structures of different dimensions (rectangle and square) that had been processed at the same conditions [temperature (82 °C) and time (1 min)]. The size of the etched features is not consistent over the surface area, as shown in figure 5.3 (b); the feature size varies from 150 to 400 nm.

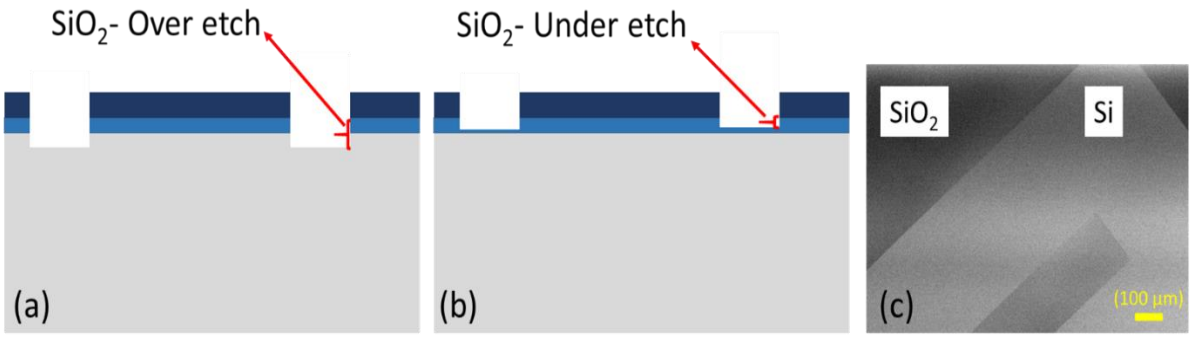

Figure 5.2. SiO_2 mask etch process in wet QR structure fabrication (a). SiO_2 layer is over-etched to provide the sites for initiating wet etching on silicon surface. (b) SiO_2 layer is under-etched and is not suitable for wet etch (c) SEM micrograph, describes a contrast of etched Si surface and unetched SiO_2 layer.

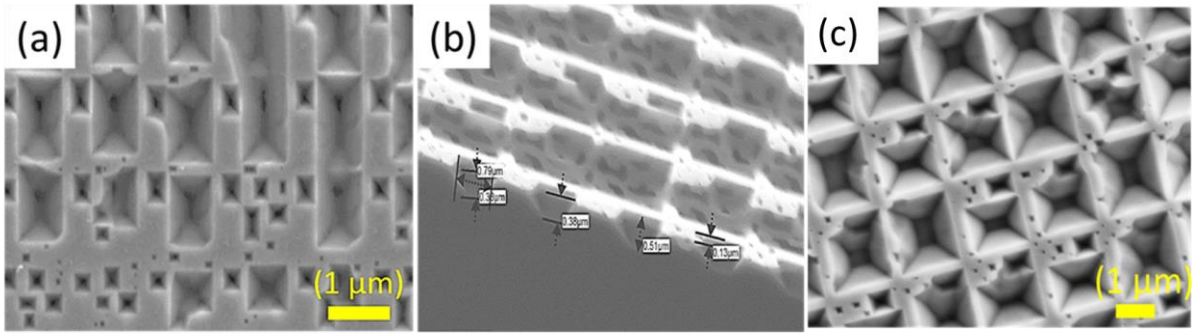

Figure 5.3. Morphology comparison of etched structures on a silicon surface at the same processing conditions of 82 °C and 2 min. (a), (c). (b) Cross-sectional view with an etch depth ranging from 150 to 400 nm.

Since reproducibility is a crucial aspect of the process, I decided not to pursue this high temperature and short time process. Therefore, I opted for a lower temperature condition of 65 °C and a longer etch time, hoping to attain better reproducibility and control. The lower temperature also gives more flexibility in terms of etch is time, which needs to be varied to achieve different etch depths. Changing these conditions also leads to a change in morphology, as schematically shown in Figure 5.4 for the two cases of (a) High temp. & short etch time and (b) Low temp. & longer etch time.

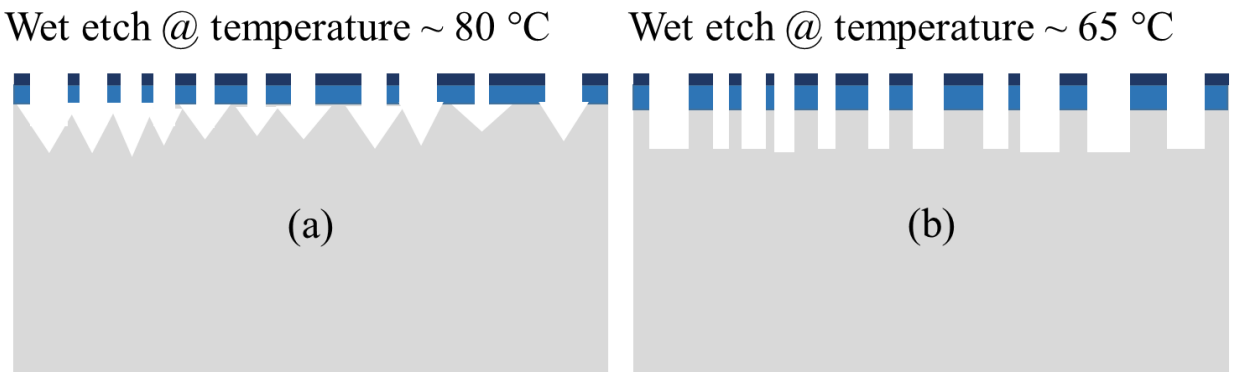

Figure 5.4. Dependence of morphology on temperature condition. (a) Temperature above 80 °C gives under-etched tapered pattern as an inverted pyramid structure. (b) Temperature at 65 °C gives much more vertical walls.

5.1.1.1.3 Optimisation of lithography conditions.

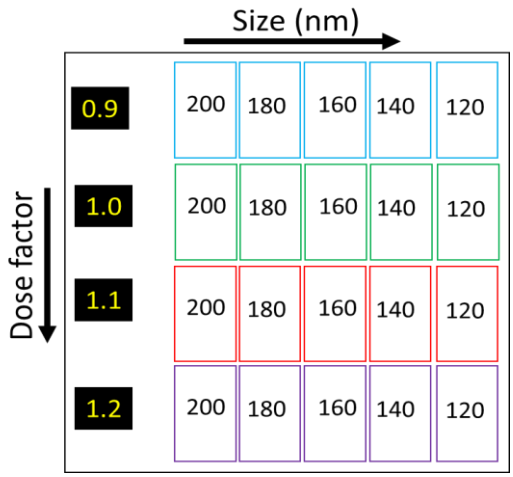

Figure 5.5. Typical sample layout at different dose factors, ranging from 0.9 to 1.2 and feature size variation from 200 nm to 120 nm.

To create QR structures of controlled size, the dose factor and the feature size need to be optimized. Figure 5.5 shows a matrix of 20 patterns which are exposed with a dose factor varying from 0.9 to 1.2 and a feature size from 200 to 120 nm. The etching proceeds at 65 °C for 10 minutes in each pattern and the SEM images of selective patterns are shown in Figure 5.6. It is clear that for dose factors between 1 and 1.2 with a feature size of 200 nm, the patterns are overetched while the minimum feature sizes (120 nm) are under etched. A dose factor of 0.9 shows the required morphology for feature sizes of 200 nm and 180 nm, as shown in Figure 5.7, so I chose a dose factor of 0.9.

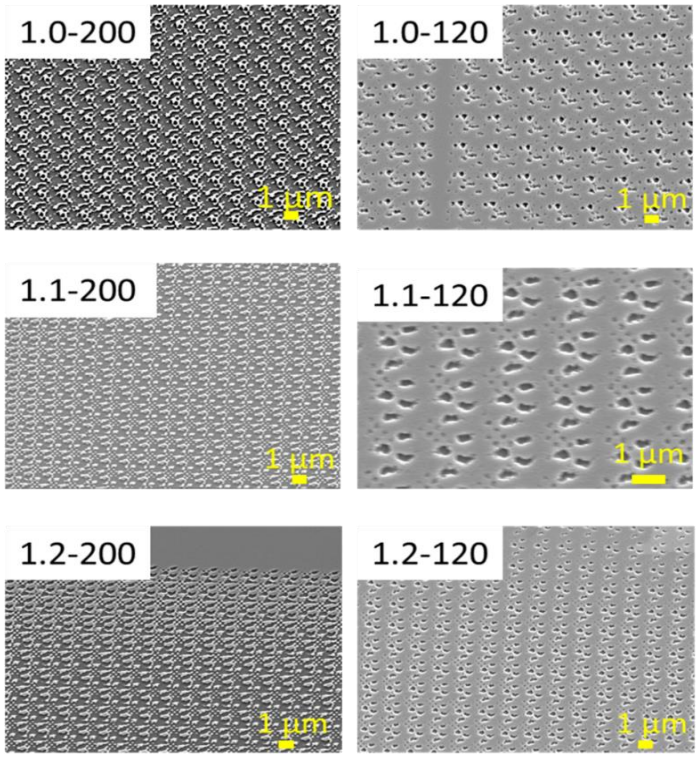

Figure 5.6. SEM micrographs of wet etched QR structures etched at 65 °C for 10 min varying dose factor and feature size.

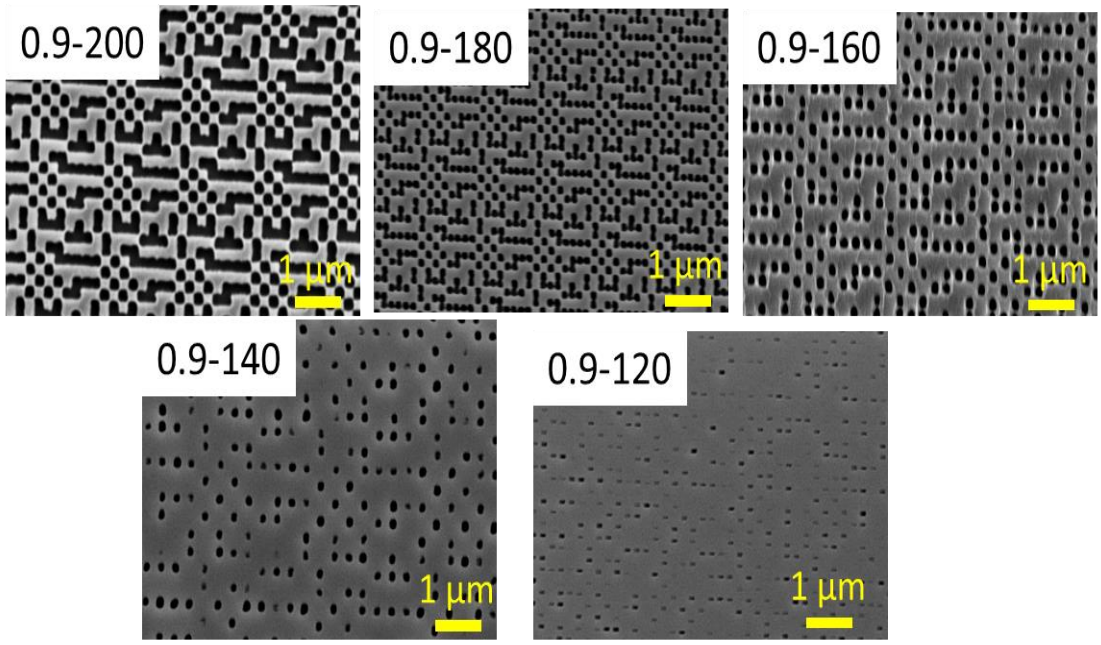

Figure 5.7. SEM micrographs of wet etched QR structure etched at 65 °C for 10 min for a dose factor of 0.9 and different feature sizes.

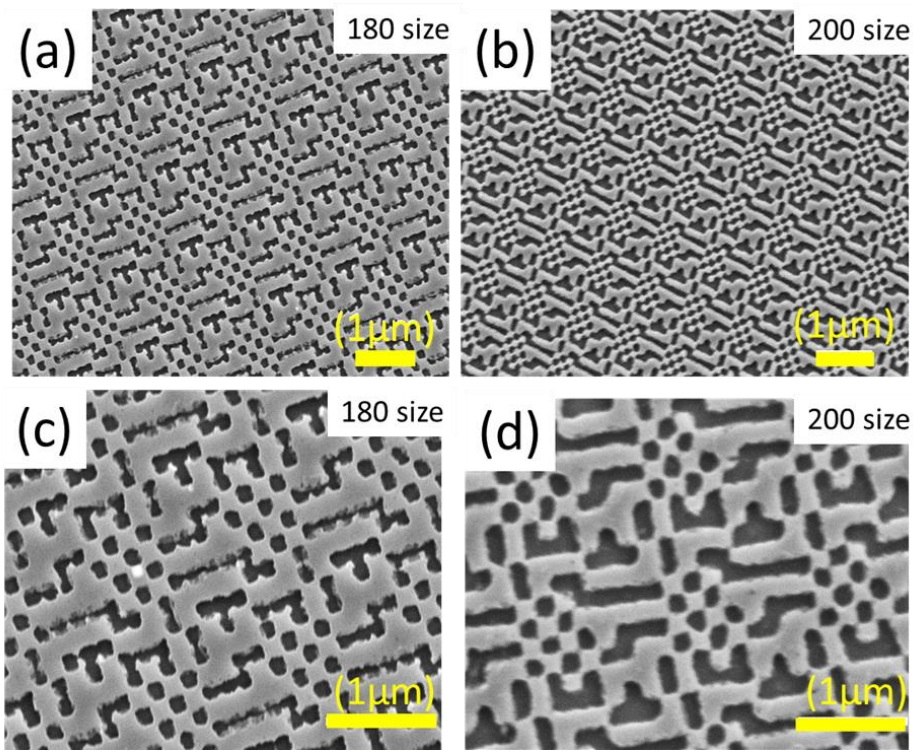

Figure 5.8. SEM micrographs of wet etched QR structures etched at 65 °C for 10 min at optimized dose factor and size conditions.

Figure 5.8 shows wet etched QR structures of dose factor 0.9 for feature sizes 180 nm and 200 nm. The 180 nm feature is shown in Figure 5.8 (a), (c) for two different magnifications, as indicated by the scalebar. The smaller features are somewhat under-etched, they have rounded edge corners and are not connected. In Figure 5.8 (b) and (d), features are connected very well and closely resemble the design file, so the dose factor of 0.9 and a feature size of 200 nm is considered optimum for a wet etched QR structure.

5.1.1.2 Dry QR structures

The same series of experiments were performed to optimize the morphology of the dry etched QR structures, although the task is somewhat easier due to the better reproducibility of the dry etch process. The RIE recipe is kept the same for each pattern, as detailed in the experimental chapter. In Figure 5.9, the dose factor is varied by keeping the feature size the

same (200 nm, as optimized in the wet QR recipe). Again, the 0.9 dose factor appears optimum, as other doses give a somewhat over-exposed structure.

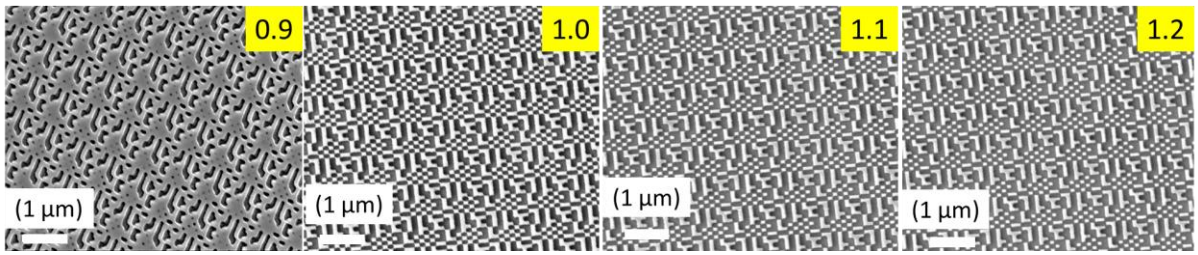

Figure 5.9. SEM micrographs of dry etched QR structures at different dose factors of 0.9, 1.0, 1.1 and 1.2 for a feature size of 200 nm. The 0.9 dose factor resembles the design pattern most closely.

5.1.1.3 Wet etched pyramid structures

Wet etched pyramids are widely used in the solar cell industry, as they do not require lithography and can be produced on a large scale with low cost. I therefore included wet etched pyramids as the control sample in our studies. To create such a micron-sized pyramid structure, I varied the etch time while keeping the solvent temperature at 82 °C. The important parameter here to look for is the fill factor of the pyramids on the etched surface.

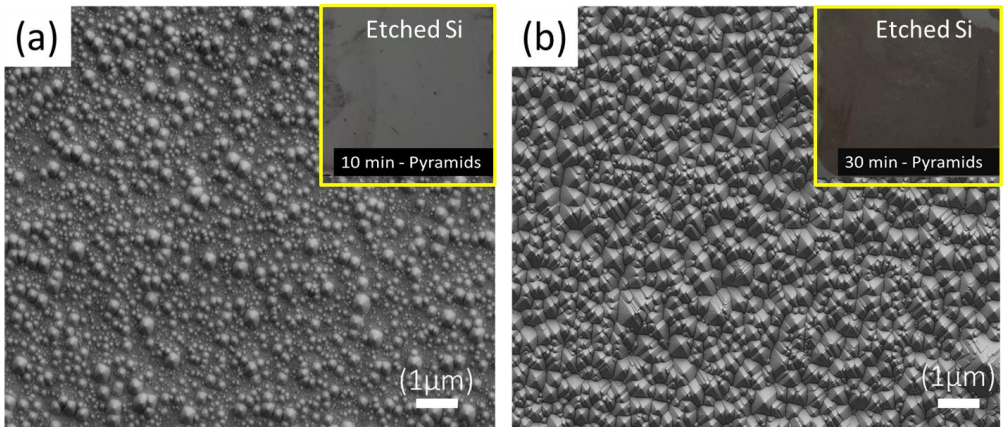

Figure 5.10. Surface micrographs of wet etched pyramids (a) for 5 min. (b) for 30 min etch time.

Figure 5.10 shows two SEM micrographs of pyramid structures etched for different times: 10 min. and 30 min. I observe a significant difference in the fill factor of the two structures, with

the 30 min. etching time producing a much higher fill factor. The insets show a low-magnification optical image of the two surfaces. The 5 min. etched surface displays a grey colour, whereas the 30 min. structure looks nearly black, indicating its much lower reflectivity. Figure 5.11. shows a zoomed-in view of a high FF pyramid surface with the base size of the pyramids varying between 2 μm and 5 μm.

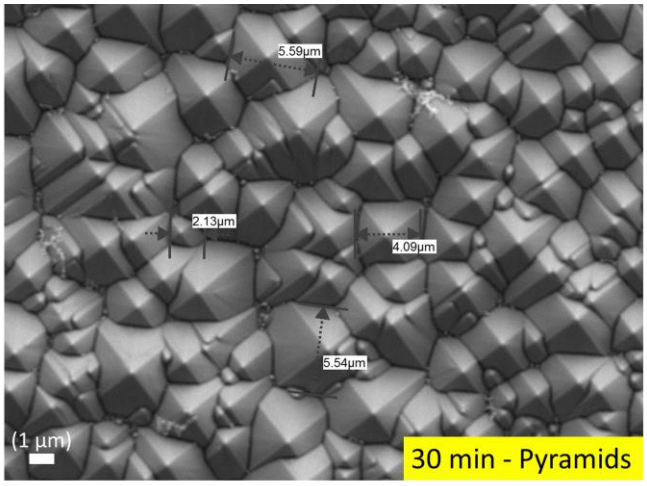

Figure 5.11. Pyramids of variable sizes are apparent on the surface for an etch time of 30 min.

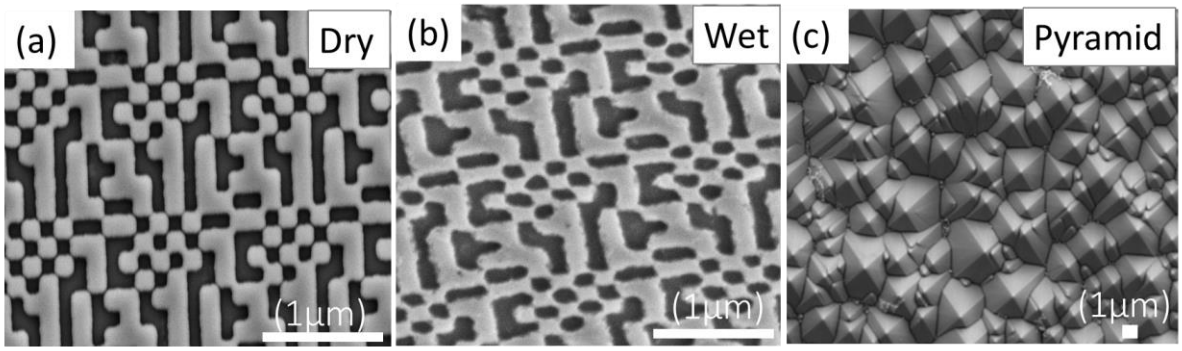

Figure 5.12. SEM micrograph images of different light trapping structures on a silicon surface for enhanced light absorption in solar cells. (a) dry etched quasirandom (QR); (b) wet etched QR and (c) wet etched pyramids.

Finally, I compare the three types of structures in Figure 5.12 (top view) and Figure 5.13 (perspective view). The dry etched QR shows uniform features which have turned somewhat rougher on the wet etched structure. The random distribution of the pyramids is clearly apparent in Figure 5.12 (c) with its (111) planes forming the angled surfaces. The typical size

of these pyramids is in the range of 1- 12 μm. As will be shown in section B, the highest performing dry QR device has an etch depth of (80 ± 10) nm (fig. 13a), the best wet QR 50 ± 10 nm (figure 5.13 (b)) and the best device of those structured with pyramids has bases up to 1500 nm in size (figure 5.13 (c)).

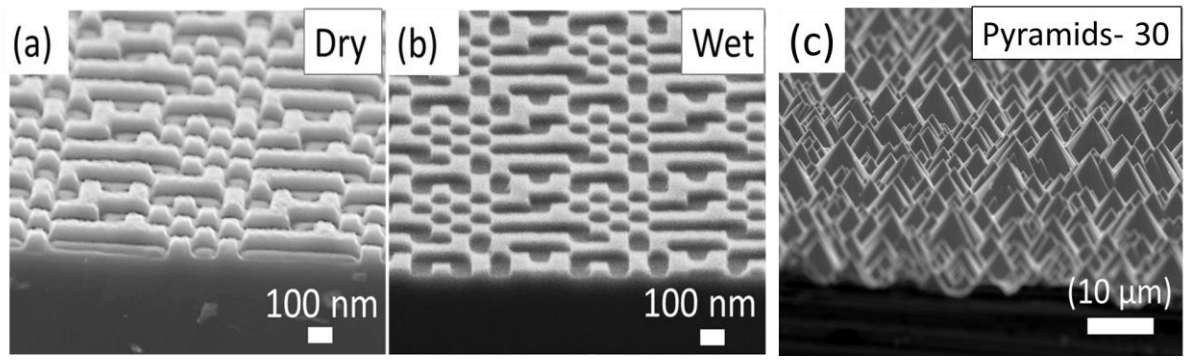

Figure 5.13. Perspective view of the best performing devices structured with (a) Dry QR; (b) wet QR (c) pyramids to allow a comparison of the different etch depths and feature sizes.

5.2 Section B

5.2.1 Device characterization

The electrical character of the devices is now investigated. First, I discuss the doping profile, then the IV- characteristics. This section highlights the challenges of fabricating devices with good electrical performance.

5.2.1.1 Doping profiles

The sheet resistance and the thickness of the doped layer are the key parameter to determine the doping profile. Typically, doping profiles used in silicon solar cells are deeper with moderate concentration or shallow with higher concentration. I opted for shallow doping with higher concentration because higher surface doping makes the contact formation easier, although it has the risk of increasing Auger recombination at the surface. The goal was to achieve a sheet resistance of $R_{sheet} \leq 100$ ohm/sq (typically used to achieve moderate doping concentration). Determining the doping profile is important for maintaining the consistency

of fabricated devices across different batches. The numbers are obtained for devices at given temperature and time conditions.

5.2.1.1.1 Sheet resistance data

The first step following doping is to remove the glassy remnant that forms during doping from the surface and to measure the sheet resistance. The quality of the doped area is significant, as the vacant sites (pinholes) or imperfections may lead to shunts. Surface defects, such as metal ion impurities or voids may cause non-uniform doping because they become active under high temperature conditions and cause a discontinuity to the introduced dopant impurities across the exposed surface.

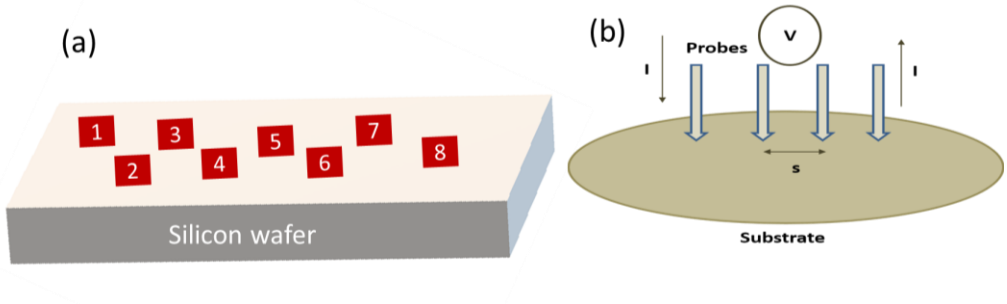

Figure 5.14. Sheet resistance (R_{sheet}) values, (a) at different positions across the silicon wafer surface. (b) measured using four-probe method.

This effect is modified as a non-uniform sheet resistance distribution at different positions of the wafer as shown in Figure 5.14.

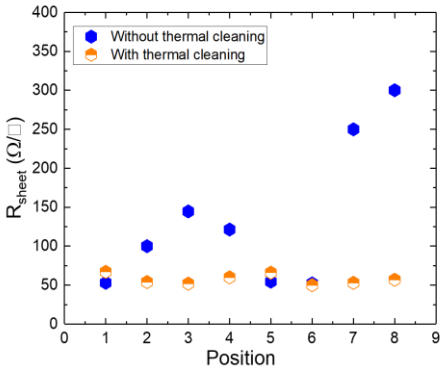

Figure 5.15. Sheet resistance spread data, with and without thermal cleaning process.

This unwanted spread in R_{sheet} values is reduced by performing a thermal oxidation step, which I name thermal cleaning. At high temperatures in the presence of oxygen, contaminations and other discontinuities at the surface are consumed by the oxide layer

which is removed afterwards with HF clean. After performing this oxidation cleaning step, the doping profiles show uniform sheet resistance values, shown in Figure 5.15.

5.2.1.1.2 Dopant layer thickness measurements

To determine the dopant profile, it is necessary to know the thickness of the doped layer. Having determined the sheet resistance over the surface, the depth of the doped layer is investigated further. I developed a multiple etch step method which proceeds as follows.

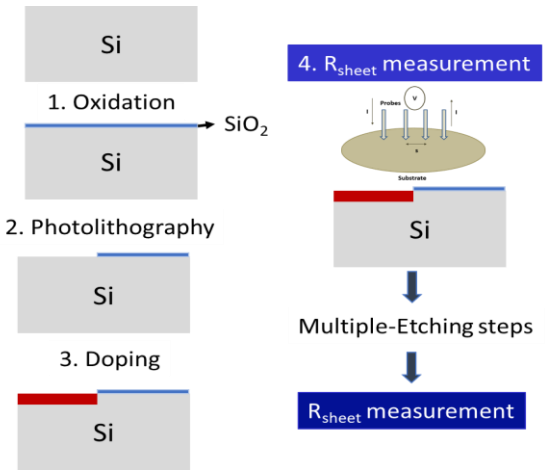

Figure 5.16. Multiple step etch method to determine the concentration profiles.

First, a step is defined on the doped surface as shown in Figure 5.16 by covering one half of the sample with a mask (SiO_2), while the other half is the doped layer. Here, the SiO_2 area is used as a reference plane to determine the etch depth via SEM cross sectional analysis.
The sample is then processed in multiple dry etching steps, with R_{sheet} being measured at each step.

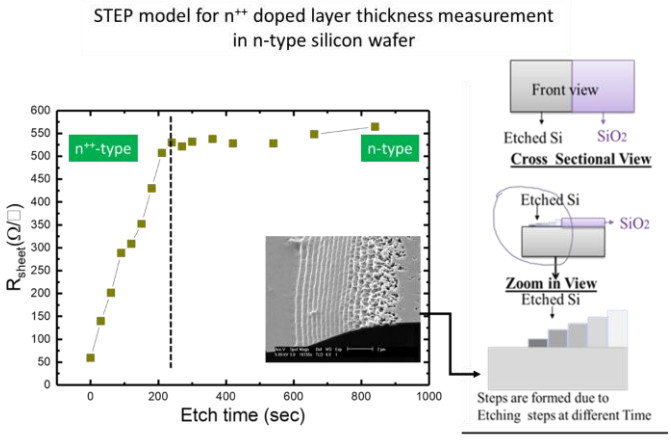

Figure 5.17. R_{sheet} measurements for multi-etched steps on a doped silicon surfaces.

Multiple etch steps are performed until the background wafer (n-type) R_{sheet} value (~500 Ω/□) is reached; an example is shown in Figure 5.17. An SEM image of the multi-etched surface is shown in the inset, which allows determining the thickness of the etch steps.

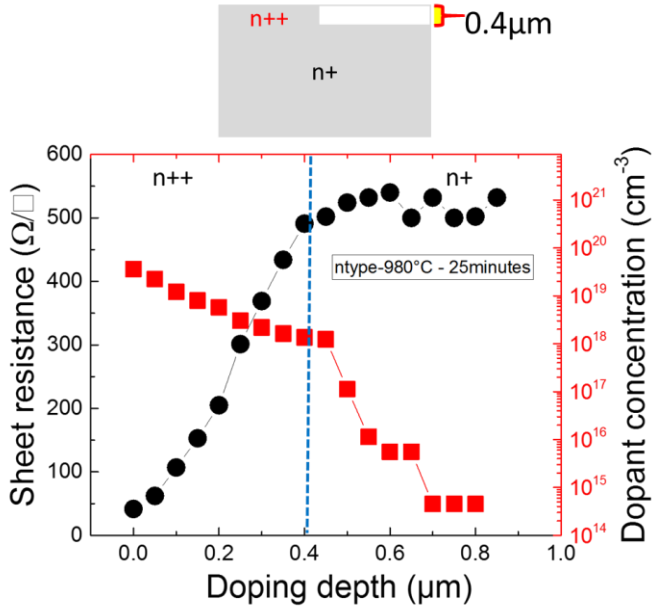

Figure 5.18. Doping profile of silicon surface doped at 980 °C for 25 minutes.

By taking an average thickness value of the doped layer from a set of samples, I estimated a thickness of 400 nm for the n-type doping process of 980 °C / 25 minutes. A dopant profile is shown in Figure 5.18. where the dopant concentration is distributed from the n^{++} region (<< 500 Ω/□) to the background n^{+} region (≈ 500 Ω/□). The doping profiles for p-type and n-type conditions are given in Table 5.1 and 5.2 respectively. These conditions are used to optimize the sequence of the fabrication process for both the FB and the IBCs devices. The doping depth and concentration profiles are shown in Figure 5.19.

Table 5.1. Doping conditions at given temperature and time for n-type process.

Sample ID	n-type doping conditions.
1	1000 °C -20 min
2	980 °C - 20 min
3	985 °C - 25 min + 850 °C - 25 min (FSF) + 1000 °C - 20 min (oxidation)
4	985 °C - 25 min + 850 °C - 25 min (FSF) + 850 °C - 25 min (oxidation)
	n-type doping conditions (FSF)

5	850 °C - 25 min
6	850 °C - 60 min

Table 5.2. Doping conditions at given temperature and time for p-type process.

Sample ID	p-type doping conditions.
1	975 °C - 40 min
2	975 °C - 40 min + 980 °C - 25 min
3	975 °C - 40 min + 980 °C - 25 min (BSF) + 850 °C - 30 min (FSF)
4	975 °C - 40 min + 980 °C - 25 min (BSF) + 850 °C - 30 min (FSF) + 850 °C - 25 min (oxidation)
5	1000 °C - 20 min deposition + 850 °C - 60 min drive-in step.
6	1000 °C - 20 min deposition + 850 °C - 30 min drive-in step.

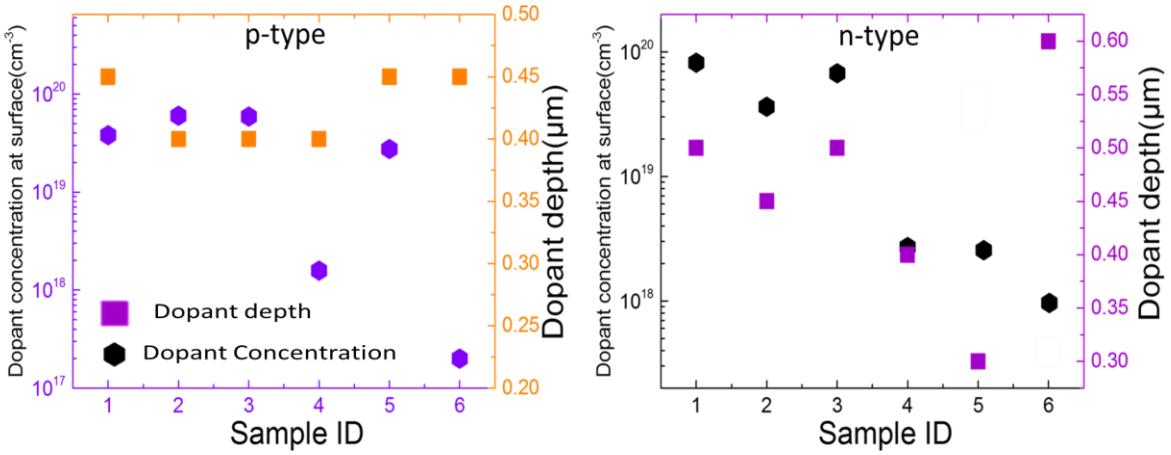

Figure 5.19. Doping profiles at given temperature and time conditions used in the realization of devices. (a) p-type. (b) n-type.

5.2.2 IV- Characteristic measurements

5.2.2.1 FB devices (No light trapping, planar surface with AR coating only)

The IV characteristic of the fabricated FB device is shown in Figure 5.20 (a), where I make a comparison with a reference device of 16.6% efficiency. The output power curves are plotted in Figure 5.20 (b), (c) with a power conversion efficiency value of 9 % for my device. The

reference device features pyramids and an AR coating while my device only features a 80 nm thick SiO_2 layer for AR coating. For the reference device, I measured a V_{oc} of 555 mV and a J_{sc} of 40 mA/cm^2, while for my device, I measured 510 mV and 28 mA/cm^2 [a and b]. In the next section, I will add the light trapping structures discussed in section A onto these devices and will discuss their advantages/disadvantages both in the optical and in the electrical regime.

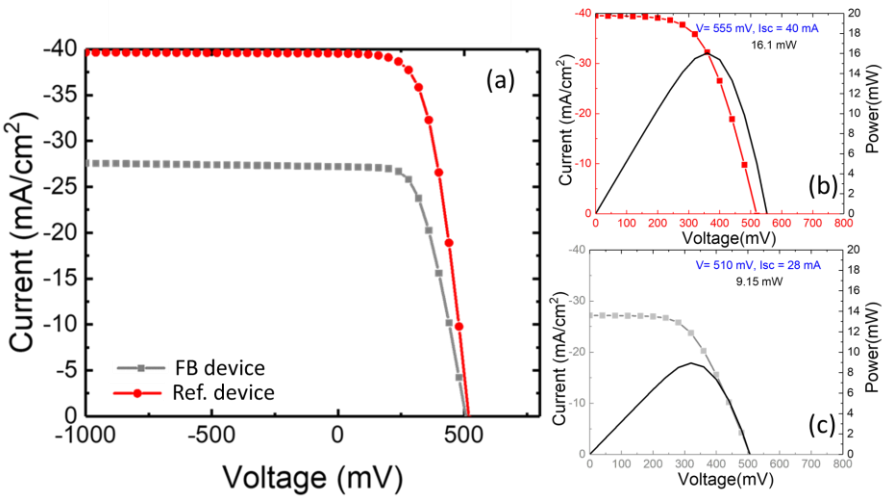

Figure 5.20. Electrical performance of fabricated FB device in comparison to a reference device of known efficiency (16.6%). (a) IV-characteristic under illumination condition. (b) Power output of Reference device. (c) Power output of fabricated FB device.

5.2.2.2 IBC devices

I also fabricated a 10% efficient IBC device, which involved developing the correct doping sequence, introducing masking barriers, edge isolation and passivation conditions. The key steps are now detailed for their significance in fabricating a working device.

5.2.2.2.1 Flowable Oxide (Fox) recipe

As discussed in the experimental section, I used FOx (Flowable Oxide, or spin-on glass) as a mask in alternative to the thermal SiO_2 mask. FOx is more convenient to use, but it is not as reliable as thermal oxide, so I found that FOx work sometimes, but not always. The recipe used to deposit the FOx is shown in the flow chart below where it is spin coated at 4000 rpm

for a final thickness value of ~250 nm (same thickness as optimized for the thermally grown SiO_2 mask), followed by baking at 220 °C and curing at 420 °C for one hour. FOx forms a uniform mask layer as shown in Figures 5.21 (a), (b) and (c).

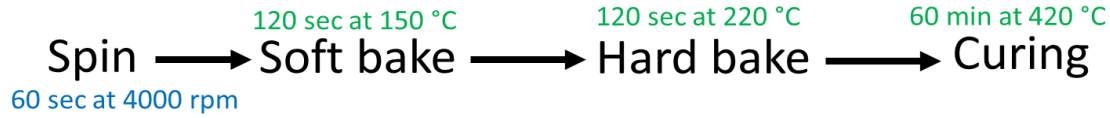

The electrical IV-characteristic under dark conditions is shown in Figure 5.21 (g), for various devices fabricated in the same batch. It is clear that low shunt resistance is always there, which is significantly changing from device to device. The reason for this inconsistency is determined by optical imaging of FOx before and after the doping processes, shown in Figures 5.21 (d), (e) and (f). It is apparent that the mask is disrupted in some devices which causes intermixing of doped species, resulting in inconsistent shunt behaviour. In the later stage of my project, a sputtering tool became available, so I replaced the FOx with sputtered SiO_2, which worked much better. Nevertheless, it was a good learning experience to understand that Fox is not as stable as SiO_2 at high temperatures and may crack which can cause shunts in the final device.

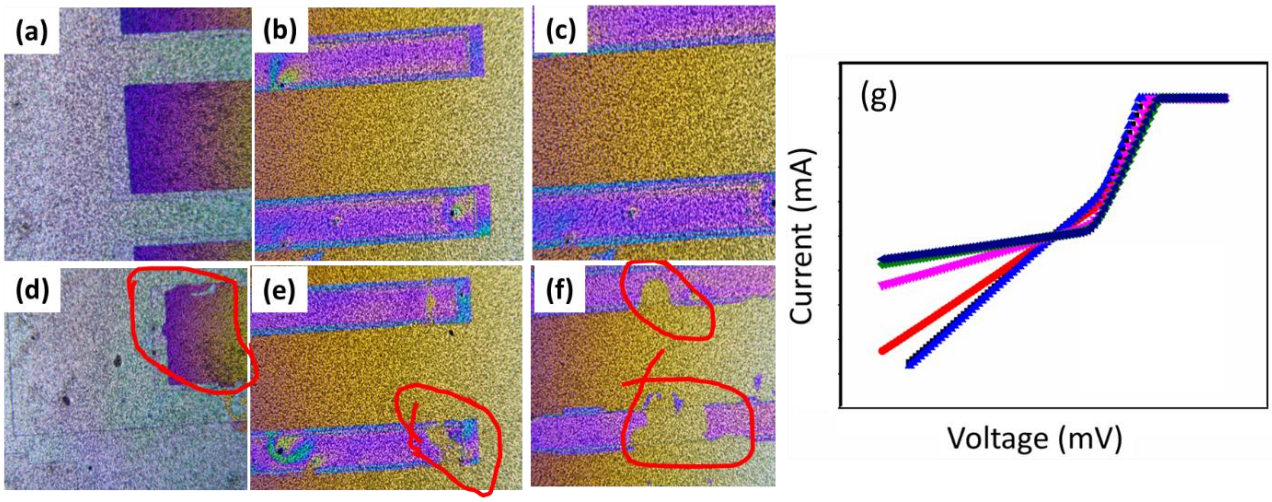

Figure 5.21. Optical images of FOx deposited onto a silicon surface. (a), (b) and (c) FOx mask before the thermal doping process. (d), (e) and (f) Fox mask after thermal doping process. (g) IV- characteristic curves for FOx processed IBC devices.

In IBC device fabrication, the edge isolation step is performed after the p-type doping process which isolates the p-type fingers from the base and the n-type fingers. It is interesting to show the significance of this process. The rear surface view of a device is shown in Figure 5.22 (a), where the SiO_2 is a mask protecting the doped p-type fingers. Two recipes are used for the edge isolation, first a Plasma (RIE) etch alone and second, a Plasma (RIE) etch followed by a wet etch (80 °C of TMAH for 3 minutes).

5.2.2.2.2 Edge isolation

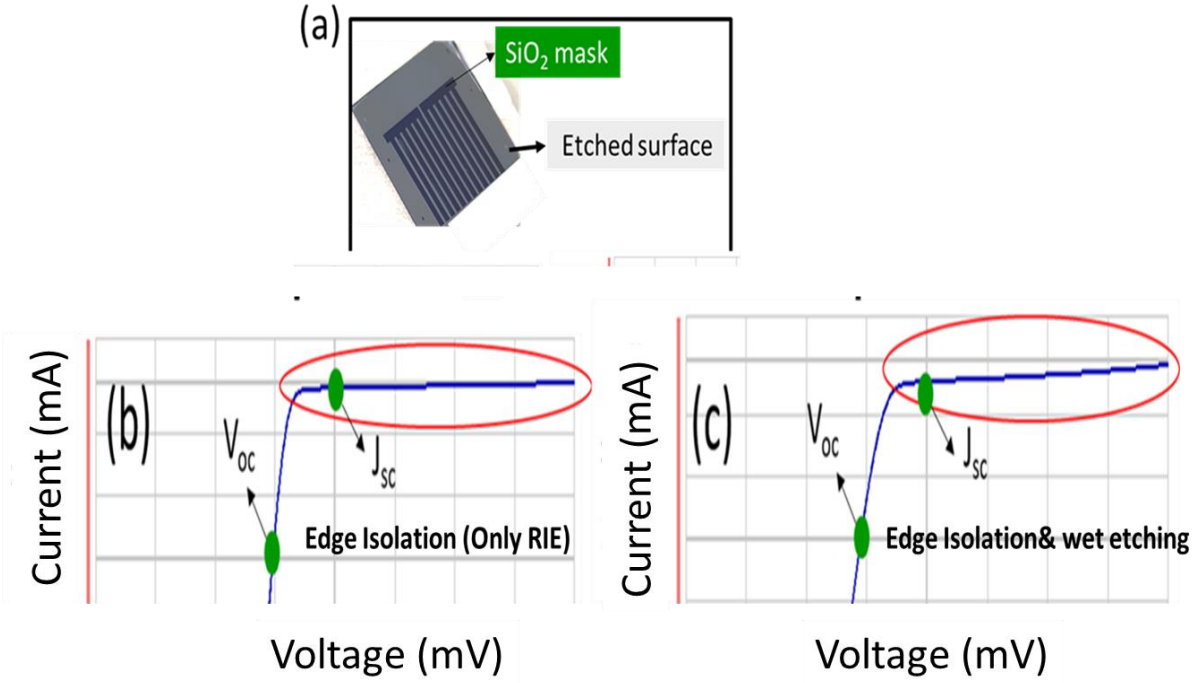

Figure 5.22. Edge isolation step optimization characterised by current leakage, apparent from the IV- characteristic curve under illuminated condition. (a)Device surface view after edge isolation with SiO_2 layer as an etch mask. (b) Edge isolation using reactive ion etch process. (c) Edge isolation followed by wet etch.

In the first recipe, the diode shows a leakage current of 1.1 mA, which causes a lowering of the photocurrent (J_{sc}) of the device under illumination conditions, highlighted in Figure 5.22 (b). This leakage current may be caused by the defects induced by the plasma etch process, which is performed for the relatively long etch time of 10 minutes. In the other recipe, the dry

etch is followed by a wet etch, for 3 minutes, which takes away all of the surface damage along with the defects. Accordingly, I observe a much lower leakage current of 50 μA, which is a significant improvement.

5.2.2.2.3 Passivation recipe

Another important processing step is to passivate the surface with a thermal oxide. I compare different passivation conditions in terms of their IV-characteristics under illumination conditions in Figure 5.23, which highlights some striking differences. When the sample is fabricated without passivation, it shows a J_{sc} value of only 5 mA. This value increases to 10 mA with a thermal passivation step conducted at a temperature of 850 °C for 25 minutes.

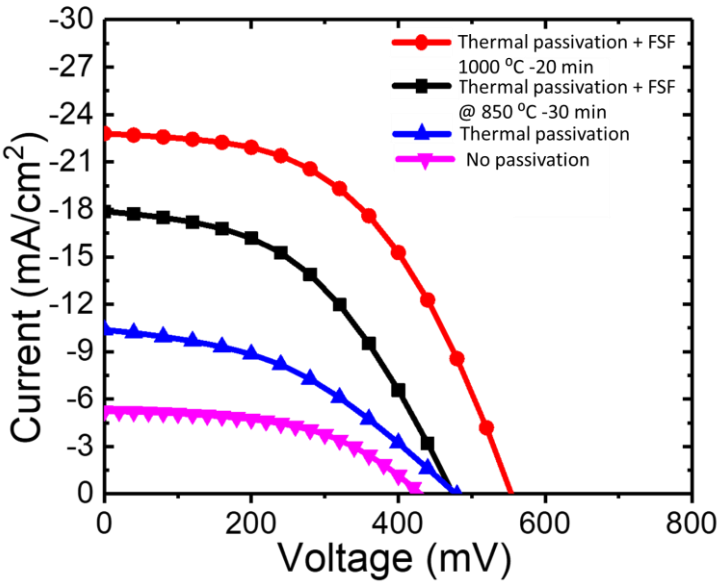

Figure 5.23. IV-characteristics of IBCs devices under illuminated conditions, fabricated using different passivation conditions.

Next, I introduce another doping step, referred to as creating a “front surface field” (FSF). This doping process is performed in order to create a high-concentration barrier with the purpose of repelling minority carriers from the front surface; the logic is that if the minority carriers are repelled form the surface, they cannot recombine with majority carriers, even if the majoriy carriers exist there in abundance. I tried two different conditions for forming the FSF. First, diffusion at 850 °C for 30 min (for a moderate concentration at surface, $2x10^{18}$,

400 nm), second, 1000 °C for 20 min, (for a high concentration at surface; $7x10^{19}$, 500 nm). The thermal passivation (850 °C / 25 min, as before) is then performed afterwards. The FSF formed at 850 °C gives a current of 18 mA, while the high concentration FSF (formed at 1000 °C) results in a currnet of 23 mA, which is clearly better [I believe this number can be improved with optimized conditions]. These values are very reasonable and form a very good basis for adding light trapping structures at the next stage.

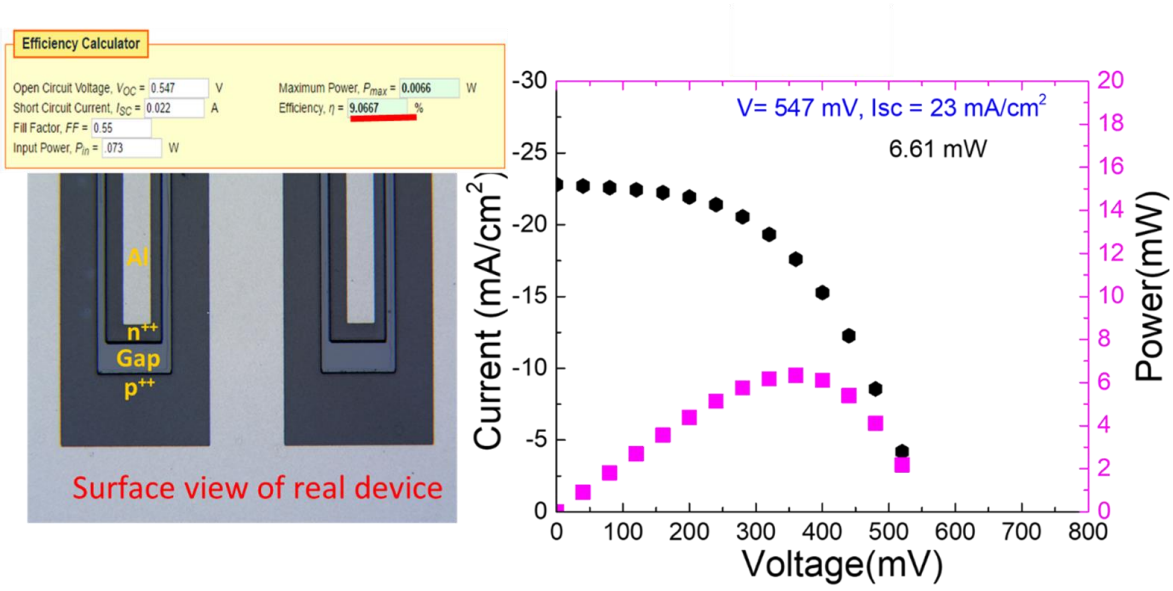

Figure 5.24. Surface view of the rear side of an IBCs solar cell (a), with (b) the corresponding output power analysis.

In Figure 5.24, For the IBC device, I achieve a 10% efficiency, which is an excellent result although it needs further optimization. The rear surface view of IBC device with contacts dimensions is shown in Figure 5.24a, which shows the power output of the device along with the IV curve under illumination (fig. 5.24b).

5.3 Section C

5.3.1 Light trapping structures on solar cell devices

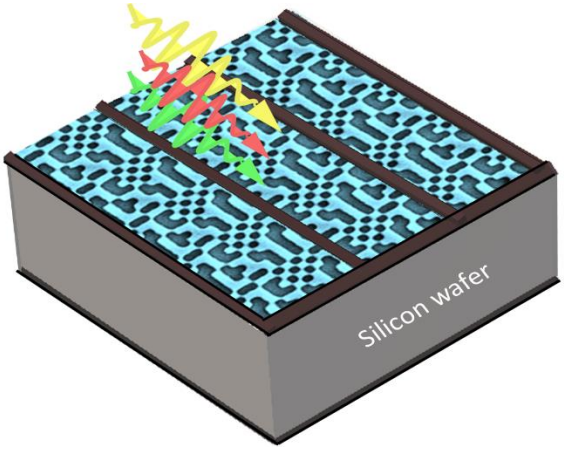

In this section, I describe the realisation and characterisation of light trapping structures on solar cell devices (both FB and IBC). For the IV- characteristic, I recall the two parameters J_{sc} and V_{oc} which are key to describing the performance of a solar cell, whereby differences in light collection through light trapping and AR coating are mainly reflected by the short-circuit current (J_{sc}), while electrical effects such as recombination losses are mainly apparent from the open circuit voltage V_{oc} as explained in the context of the diode equation given below:

$$V_{oc} \approx \frac{nk_BT}{q} \ln\left(\frac{J_{Ph}}{J_0}\right) \qquad (5.1)$$

where $\frac{k_BT}{q}$ is the thermal voltage and *n* represents the ideality factor. V_{oc} is the voltage when no current flows through the external circuit and it is directly dependent on the saturation current density (J_0) and the photo generated current density (J_{Ph}). As described in the equivalent circuit of a solar cell, recombination losses occur in the internal circuit, so they directly impact on J_0 and thereby on the V_{oc}; hence a variation in V_{oc} is interpreted as a signature of recombination losses.

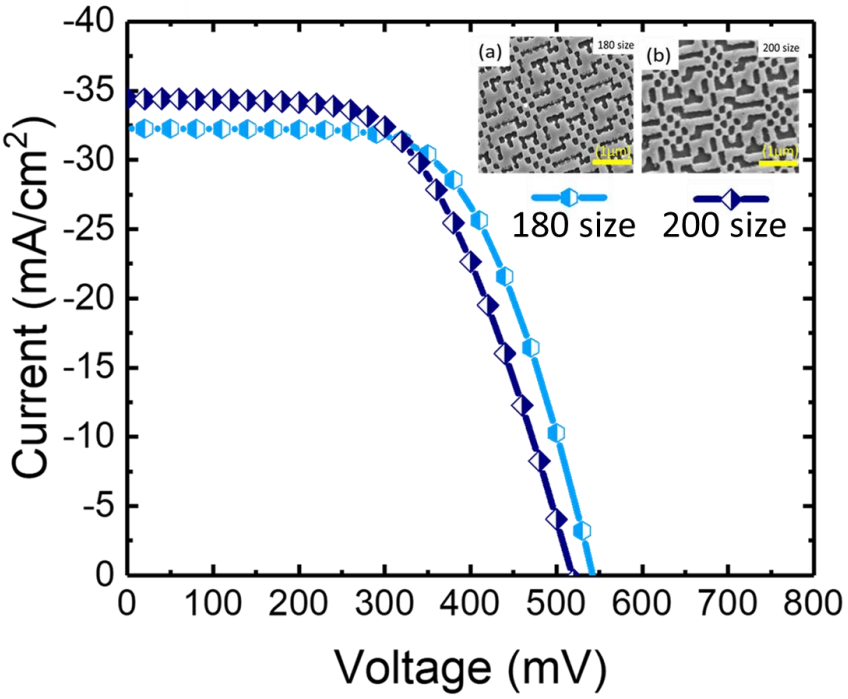

Figure 5.25. IV - characteristic comparison of wet QR structures for different feature size, i.e. 180 nm and 200 nm.

I start with the IV- curve comparison of the wet QR structures optimized for a feature size of 180 nm and 200 nm, shown in Figure 5.25. The V_{oc} changes from 522 mV to 540 mV and the J_{sc} changes by approx. 1 mA. These differences are not large, so I opted for the 200 nm feature size of the wet QR structure for a fair comparison to the Dry QR which is also 200 nm in feature size.

Next, I compare wet and dry QR structures separately, in terms of the contact placement. In one design, the QR structures are etched onto the silicon surface with the contact finger area being left un-etched. In another design, all of the surface area is structured and the contact fingers are directly deposited on the structured surface. In Figure 5.26, the IV- characteristic for both wet and dry QR structures, the fill factor is significantly affected when the flat area contact finger design is used. This effect, I assume, is mainly arising due to the difference of the etched and unetched surface height. If the etch depth of the structure is 50 nm deeper than the deposited contact fingers, this adds a path length for carrier collection which may lead to

a higher series resistance of the device. To avoid this issue, I deposit the contacts directly on the etched features in all three (wet, dry and pyramid) structures.

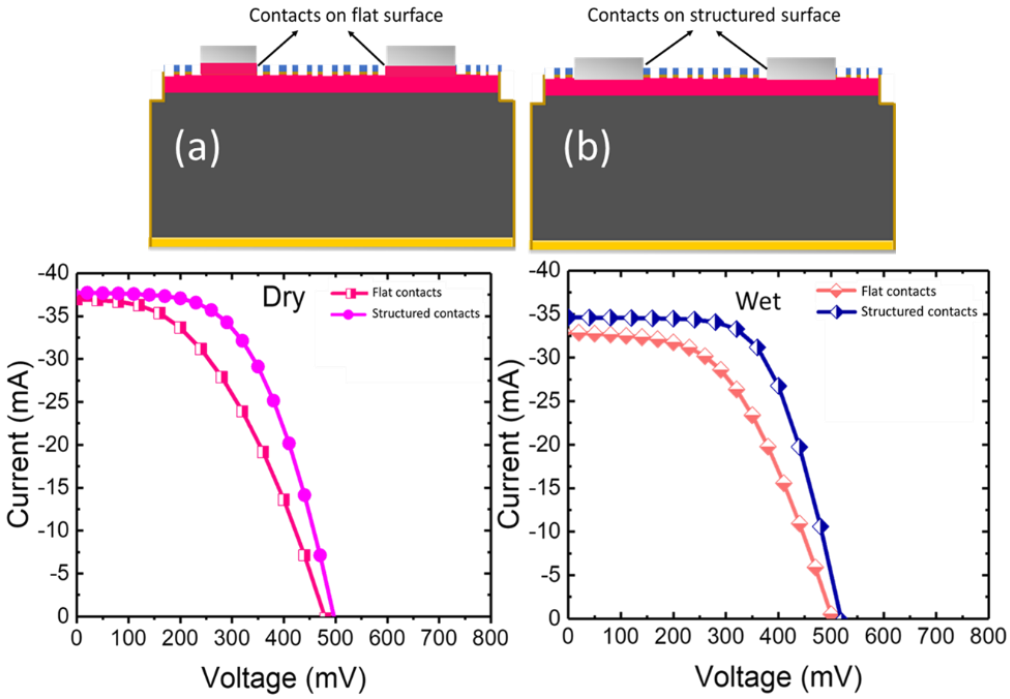

Figure 5.26. IV - characteristic comparison of Dry and wet QR structures for different contact configurations. i.e. contacts on flat surface and contacts on structured surface.

Next, I compare the IVcurves of different wet QR structures as a function of etch time/depth in Figure 5.27 and note that the 7 minutes etch, with its 50 nm etch depth, exhibits the highest performance of all three wet etched structures.

For 10 minutes (70 nm) and 13 minutes (100 nm), V_{oc} and J_{sc} both reduce with etch depth. The lowering of the V_{oc} is associated with the higher surface area caused by the deeper etch, thus creating more surface recombination centres. The lowering of the J_{sc} is assumed to be caused by the increased roughness on wet etched features as a function of etch time (notice also the SEM images). As roughness promotes random scattering, it reduces any light trapping effect. This argument is supported by the optical absorption and external quantum efficiency spectra.

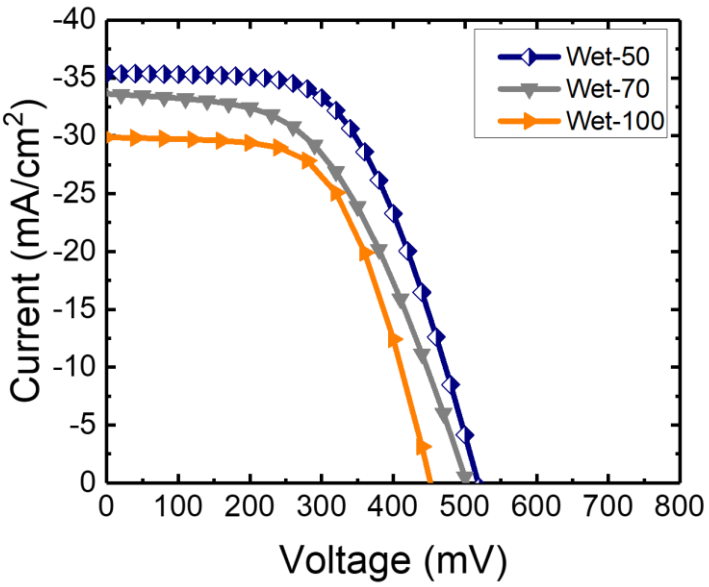

Figure 5.27. IV comparison of wet QR structures for different etch depths, i.e. 7 min (50 nm), 10 min (70 nm) and 13 min (100 nm).

A comparison of the wet etched QR structures as a function of etch depth/time i.e. Wet-50 (50 nm/7 min) and Wet-70 (70 nm/10 min) is shown in Figure 5.28. It is clear that the deeper structure performs worse than the shallower one at longer wavelength where light trapping is most effective. This observation is counter-intuitive but supports my random scattering hypothesis.

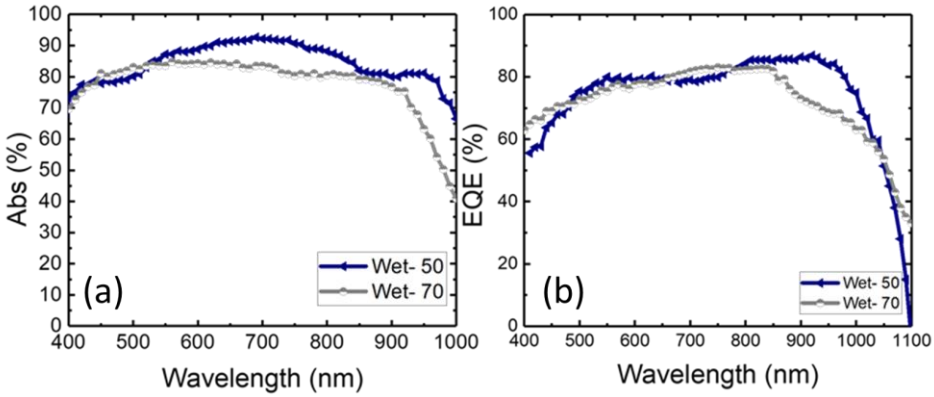

Figure 5.28. Wet etched QR structures for etch depths of 50 nm and 70 nm. (a) Optical absorption spectra comparison. (b) EQE spectra comparison.

The EQE data (Fig. 5.28b) is almost identical, except in the long wavelength regime, for the same reason. It is noted that unlike in the dry etched case, the performance in the blue is virtually identical because there is no difference in surface de fects as a function of etch depth. So, 50 nm is the best etch depth for wet etched QR structures.

Similarly, to optimize the dry QR structure in terms of etch depth, devices have been realized with different etching time. The absorption and EQE spectra of these dry etched structures for the three different etch depths/times of 40 nm (30 sec) 80 nm (50 sec) and 110 nm (90 sec) are shown in Figure 5.29. Absorption measurements are shown in Figure 5.29 (a). It is noted that the optical absorption characteristics are better for the 80 nm (Dry-80) and 110 nm (Dry-110) structures while absorption is lower for the 40 nm etch depth (Dry- 40). The EQE spectra comparison in Figure 5.29 (b) then shows that both devices give equally good response in the longer wavelength range while in the blue, Dry-80 is better, so Dry-80 shows the higher performance overall. The lower EQE in the blue for Dry-110 indicates stronger surface recombination due to the longer etch time because blue light is absorbed closer to the surface so is more sensitive to surface defects

Finally, for the pyramids, as I fabricated two structures with low fill factor (10 minutes etch) and high fill factor (30 minute etch), shown already in SEM images (Figure 5.10).

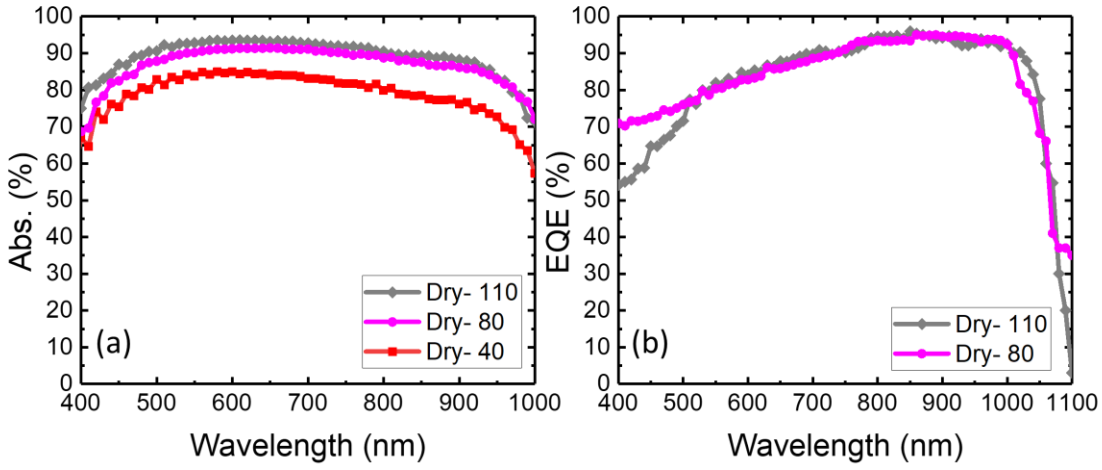

Figure 5.29. Dry etched QR structures for etch depths 110 nm, 80 nm and 40 nm. (a) Optical

absorption spectra comparison. (b) EQE spectra comparison.

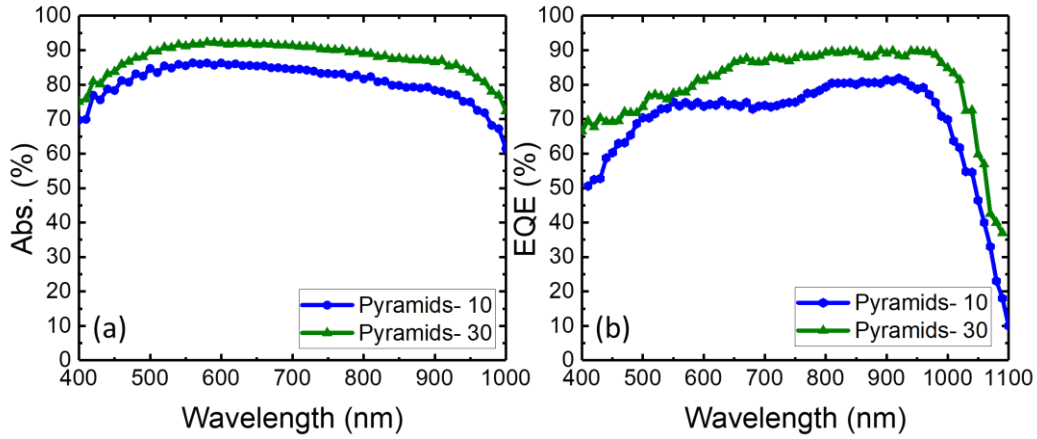

Figure 5.30. Wet etched pyramids for 10 min. and 30 min. etch time. (a) Optical absorption spectra comparison. (b) EQE spectra comparison.

The effect of the pyramid fill factor is clearly reflected in the opto-electronic performance shown in Figure 5.30 (a) which shows the optical absorption while Figure 5.30 (b) shows the EQE comparison, with the 30 min. structure being superior in both cases. The optical comparison is done for different etch times to determine the highest performing pyramid structure as shown in Figure 5.30a. I note that longer etch time improves performance, the key being to ensure that the entire surface is covered with pyramids of different sizes.

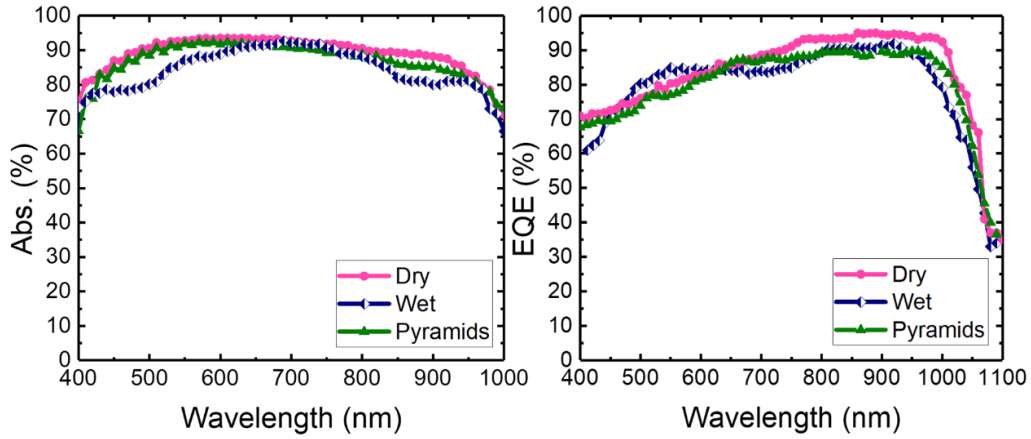

Figure 5.31. Comparison of a) the optical absorption spectra and b) the external quantum efficiency of the three structures over the wavelength range from 400 to 1100 nm.

Now I compare the three types structures altogether, all fabricated with their optimized conditions. The absorption spectra of the three structures are shown in Figure 5.31 over a wavelength range from 400 to 1100 nm. The spectra show that the QR structures show slightly better absorption performance than the pyramids over the entire wavelength range, both in the blue, which is associated with AR coating properties, and in the IR, which is associated with light trapping. The dry QR performs better than the wet QR, which is associated with the increased roughness of the latter. This difference highlights the importance of the controlled scattering performed by the QR structure, which appears to be more effective than the random scattering of rough features. This difference between the QR structures is more pronounced in the EQE measurements (Figure. 5.31b).

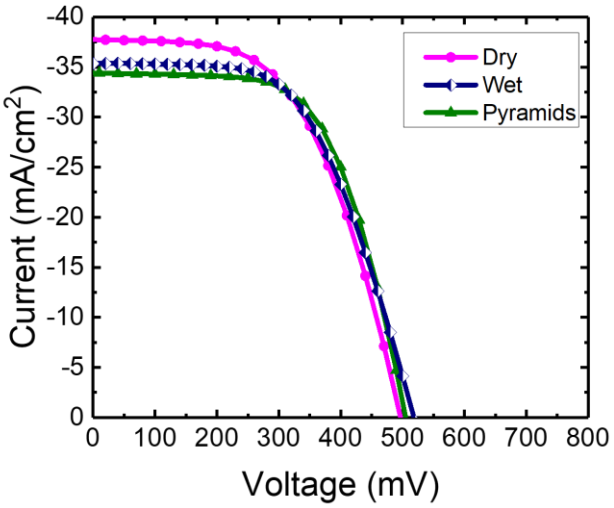

Figure 5.32. Comparison of the I-V curves of pyramids vs the two types of QR structures.

Here, the dry QR shows its advantage in the light trapping region in comparison to the pyramids**;** this advantage is also reflected by the IV- curves (Fig. 5.32), especially in terms of the short circuit current density (J_{sc}) where the highest value (38 mA/cm^2) for the dry QR structure is observed. Overall, the dry QR is the highest performing of the three structures, which is interesting and unexpected: indeed, the general perception is that pyramids should

outperform nanostructures in thick solar cells. It is worth recalling that all structures have been optimised for etch depth to allow a fair comparison, the performance as a function of etch depth for the three different structures having been discussed in Figures. 5.28-5.30.

Figure 5.32 compares the opto-electronic behaviour of the three structures via their IV-characteristic. The pyramids and the wet etched QR exhibit the same V_{OC} of ~520 mV, which is not surprising as they have experienced almost identical processing steps with the surface structure having been wet etched in both cases. The curves shown here are representative of a large number of samples and we typically observe deviations of less than ±5 mV between nominally identical samples made in different batches. In terms of J_{sc}, the wet QR outperforms the pyramid, which is unexpected. Again, it is noted that pyramidal structures made in different batches look somewhat different due to the spontaneous nature of the wet etch process, but their performance is consistently below those of QR structures. While it is not claimed here that the comparison is made with the very best pyramidal structure, still it is a remarkable finding that the QR structure, which was originally designed for thin film silicon devices, also performs well in bulk solar cells, and that it performs even better than the widely used random pyramids.

5.3.1.1 Light trapping structures integrated into IBCs solar devices

Finally, I compare the IV curves of IBC devices as shown in Figure 5.33, integrated with wet (50 nm; etch depth) and dry (80 nm; etch depth) QR structures. I use the QR structures which performed best in the FB devices. In Figure 5.33 (a), both devices show a decent diode character with leakage current of no more than 30 μA but with an increase in series resistance; 10.5 Ω is observed, which is high compared to the 4.5 Ω observed in FB devices. Under illumination, the series resistance contributes to lowering the FF (poor electrical performance) which makes my IBCs a poorer choice for evaluating the effects of light trapping structures. The optical performance wet and dry QR structures exhibit values of J_{sc}

of 28 mA and 32 mA, respectively, so the dry QR structure performs better than the wet QR structure, as already observed in FB devices. The V_{oc} (555 mV) is higher in both IBC devices than in FB devices (≈ 500 mV) which highlights the main advantage of using IBC structures. As the junction is placed away from the etched nanostructures, surface etching losses do not affect V_{oc} as much as they in FB devices.

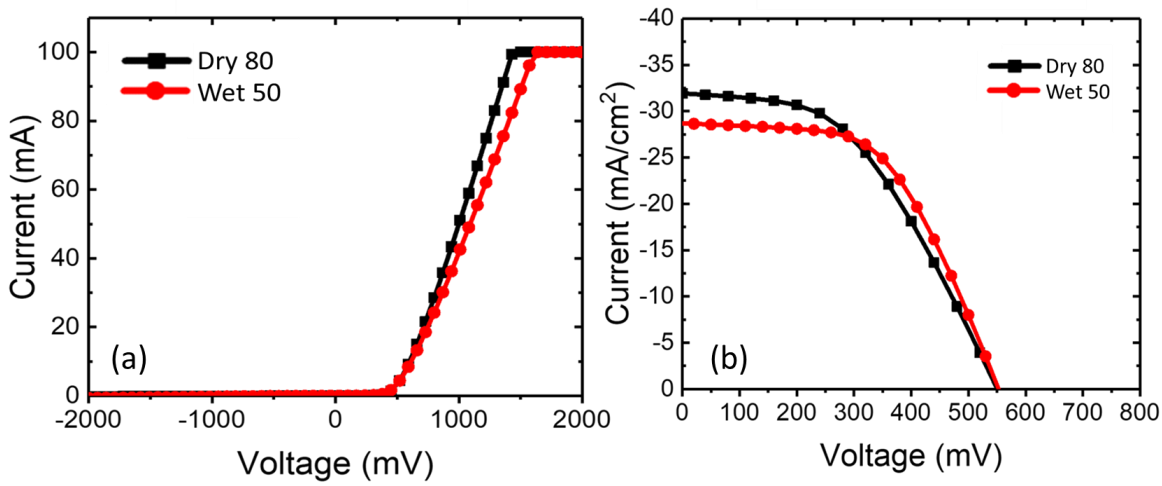

Figure 5.33. IV-characteristic comparison of IBCs devices integrated with wet and dry QR structures. (a) under dark condition. (b) under illumination condition.

To summarize, I have shown that deterministic, quasirandom nanostructures offer better light trapping and antireflection properties than randomly etched pyramidal structures. This is somewhat unexpected, as the quasirandom class of structures was invented to improve light trapping in thin film solar cells, but not in thick devices. Here, the speculation is that the controlled number of diffraction channels offered by the quasirandom approach is advantageous, especially as it favours diffraction into guided modes with high absorptivity rather than random scattering [95] which also excites air modes that can radiate back into free space. This hypothesis is supported by the fact that the wet etched QR structures, with their increased roughness, perform less well than the dry etched ones that use the same design. Verifying this hypothesis is the subject of further study.

Additionally, it is noted that the dry etched QR structure is the highest performing structure I have investigated (both in FB and IBCs), which suggests that the dry etch damage suffered is not as detrimental as expected, which is most likely due to the gentle etch recipe and low etch depth (80 nm) used here. Overall, the comparison of different nanostructures on real solar cell devices is demonstrated that can obtain a short circuit current as high as 38 mA/cm^2 with dry etched structures, which is close to the State-of-the-Art for silicon and thus demonstrates that quasirandom nanostructures have an important role to play even in bulk silicon devices.

6 Chapter 6: Perovskite as an optoelectronic material

This chapter introduces perovskites material, which is famous for its meteoric rise in efficiency, from 3% to 22.1 % over a timespan of only 5 years. Perovskites are solution-processable, so are inherently cheap to make. Even more interestingly, perovskites can be combined with silicon solar cells in a tandem configuration and achieve higher efficiencies. Recall that a single junction silicon solar cell can give a maximum theoretical efficiency of 31%, known as the Shockley-Queisser limit, a value recently updated by Richard et al[30] to 29.4 % by taking non-radiative recombination losses into account. The Shockley-Queisser limit is based on a material with a single bandgap only.

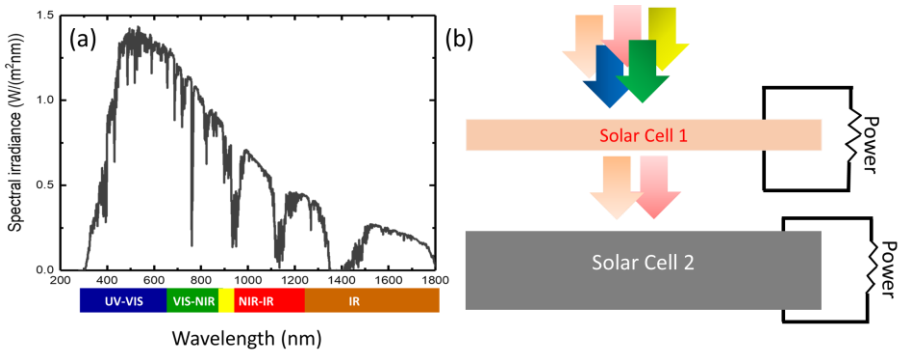

Figure 6.1. (a) Solar spectrum highlighting different ranges of photon energy; (b) sketch of a tandem configuration, whereby the top cell converts high energy photons and the bottom cell converts the low energy photons.

One approach to increase the efficiency is therefore to combine multiple materials with different bandgaps, e.g. in two-material tandems. In such a tandem stack, the blue part of the spectrum is converted by a large bandgap semiconductor, and the red part by the lower bandgap silicon, a configuration illustrated in Figure 6.1.

In order to realise such a silicon-based tandem cell, a wider bandgap material should be placed on top, with a bandgap of 1.5 eV-1.8 eV being considered ideal).[96] [97] III-V semiconductors could provide the top layer material and indeed, an efficiency of 29.8% has already been achieved with a four terminal Si/III-V tandem architecture.[98] The problem is that III-V technology is too expensive. The lack of a cost-effective photovoltaic material with suitable efficiency has inhibited the realisation of a competitive c-Si based tandem device. The situation has changed recently following the reports of dramatically improved perovskite efficiency to the current value of 22.1%. [99]. Such perovskites are very promising candidates for the large bandgap semiconductor in a tandem cell.

More specifically, the term "perovskite" in this context refers to the family of hybrid organic-inorganic lead halides that crystallise in a perovskite structure. A crystal structure with the general formula ABX_3 (where A is referred to as the organic cation, B is a divalent metal component and X is a halide or combination of different halide ions) is referred to as perovskite; a generic lattice structure is shown in Figure 6.2. Different types of perovskite compounds are under investigation, e.g. $CH_3NH_3SnI_3$, $CH_3NH_3PbI_{3-x}Cl_x$, $CH_3NH_3PbI_{3-x}Br_x$ or Cs lead halides. [100,101]

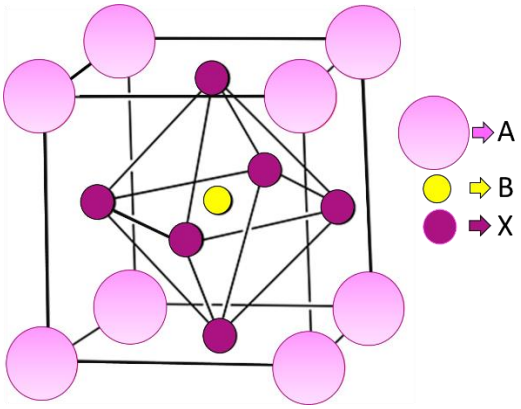

Figure 6.2. Crystal structure belonging to perovskites family.

For solar cell applications, organic-inorganic lead tri iodide with a band gap of 1.50 eV to 1.56 eV (depending on the iodide composition) has been the most efficient and stable material so far, compared to other compositions. Based on the negligible exciton binding energy (large exciton binding energy being a major hurdle in organic solar cells), free charge carriers are formed directly upon photoexcitation. Accordingly, an approximately ~500 nm thin film is sufficient to absorb the incident light completely over the entire visible spectrum with very low blue spectrum absorption. Based on this low absorption, the short wavelength radiation up to 1.1 eV is then efficiently converted by the silicon bottom cell. Such a tandem configuration has a theoretical efficiency limit of over 41%, [99]overcoming the single c-Si limit of 29.4 %.

6.1 Experimental:

6.1.1 Perovskite solar cell structure

Different architectures of perovskite cells have been reported depending on the energy band diagram. Commonly, a hole transfer layer (HTL) and an electron transfer layer (ETL) are added to the active layer in order to extract holes and electrons from the absorber. Two exemplar architectures are shown in Figure 6.3, namely (a) a regular p-i-n (HTL-Perovskite-ETL) [102]and an inverted n-i-p (b).[103]

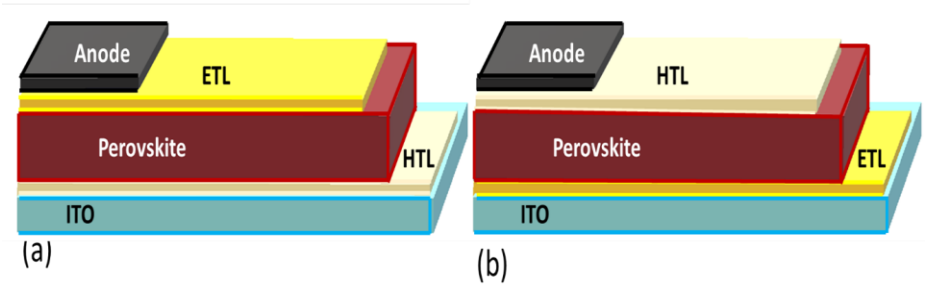

Figure 6.3.Commonly used configurations for perovskite solar cell device. (a) regular p-i-n (ETL-Perovskite-HTL) (b) inverted n-i-p (HTL-Perovskite-ETL).

In my experimentation, I used the inverted n-i-p structure, which is shown in Figure 6.4 (a), (b) with its energy band diagram. The process flow chart I used for the cell fabrication is shown in Figure 6.5.

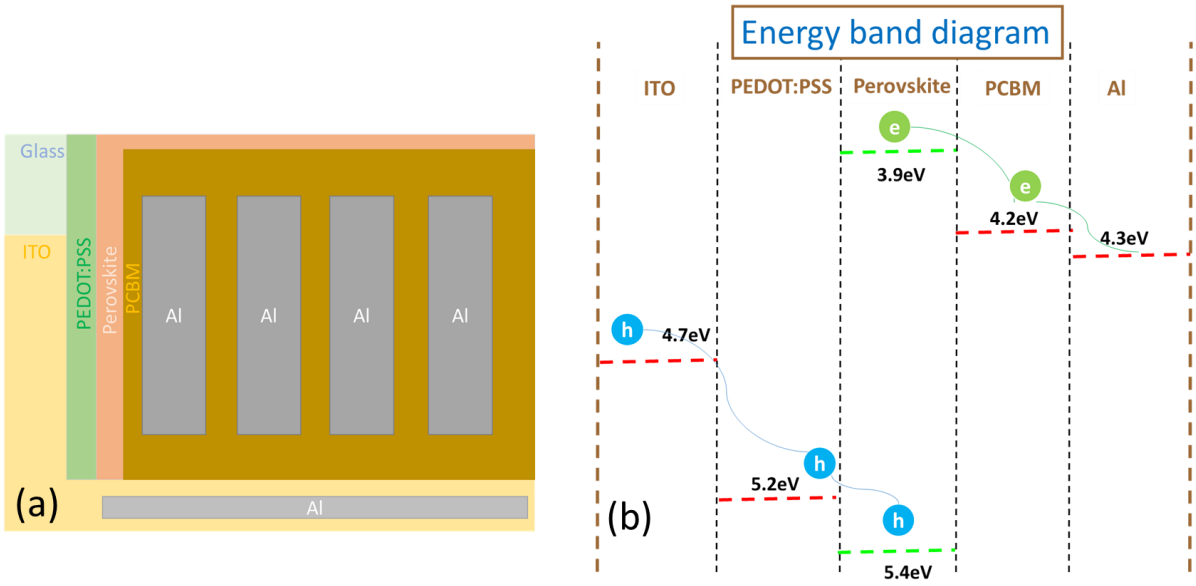

Figure 6.4. Top view of perovskite solar cell; (a) perovskite absorber layer deposited between PEDOT:PSS (HTL) and the PCBM (ETL) according to the inverted n-i-p geometry. (b) Energy band diagram.

6.1.1.1 Materials:

An aqueous dispersion of PEDOT: PSS - AI 4083; 1:6 (1.3 to 1.7 wt. %) in water from Ossila Ltd. was purchased and PCBM (99%) was obtained from Solenne Netherlands. CH_3NH_3I and PbI_2 precursors with 99.999% purity were purchased from Sigma Aldrich Co.

6.1.1.2 *Fabrication of device:*

The layer deposition sequence for perovskite solar cell structure, is shown in Figure 6.5. I used a glass substrate with a transparent ITO layer as an electrode. Unpatterned ITO-coated glass substrates were also purchased from Ossila Ltd. with a sheet resistance value of 20 Ω/□, thickness of 100 nm and sample dimension of (1.5*2) cm^2. These substrates were patterned by etching away ITO layer in our laboratory. For this I used chemical etching with HCl and

Zn powder which removes ITO on the unmasked area. The etched substrates were then cleaned with Acetone, Isopropanol and rinsed with boiling distilled water then blow-dried in N_2. Finally, a plasma oxidation process is performed; this step serves to make the surface hydrophilic in order to obtain a uniform spin-coat.

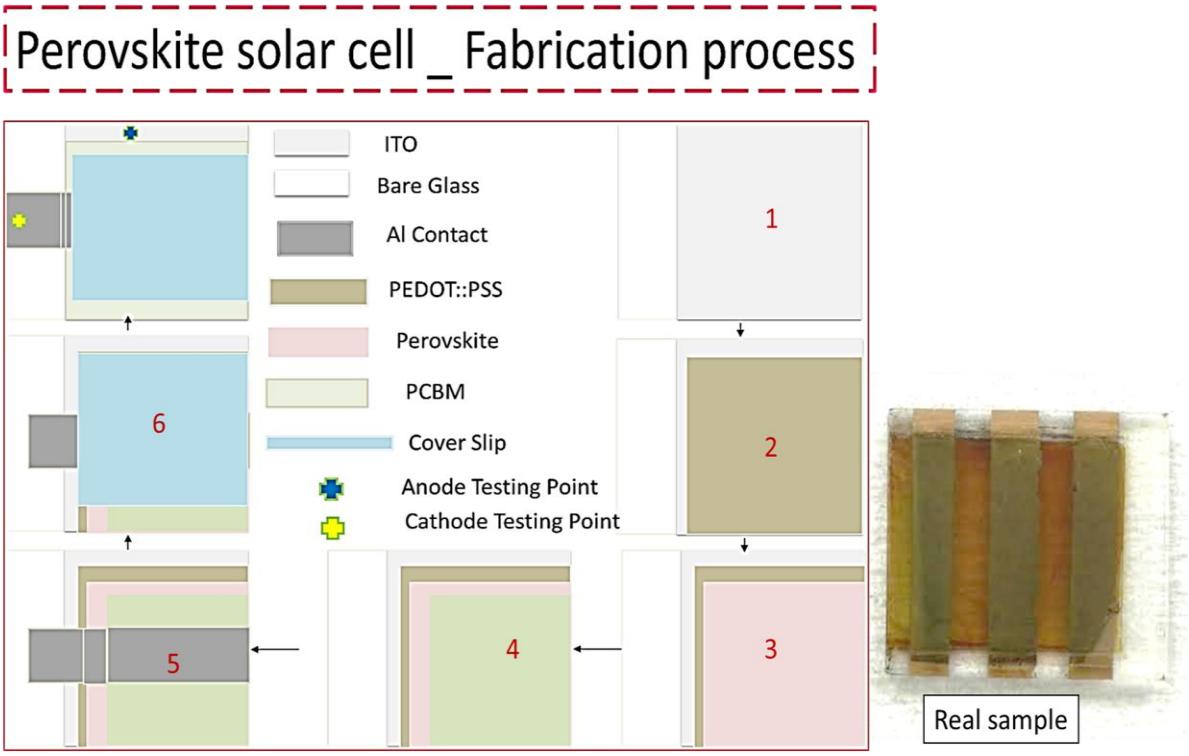

Figure 6.5. Schematic illustration (top view) of a perovskite solar cell during fabrication process; along with the picture of a fabricated device.

The oxidized substrates are preheated at 120 °C temperature and then spin coated with PEDOT (HTL) at 6000 rpm for 30 sec, targeting a thickness of 40 nm, then annealed at 180 °C 15 minutes. Next, the substrates are transferred to a glove box for the perovskite film deposition. As the perovskite synthesis is sensitive to the external environment the deposition is performed in a glove box. The glove box achieves a very low oxygen and water concentration, i.e. O_2<0.5 ppm and H_2O<0.5 ppm (Figure 6 (a)). The details of perovskites fabrication process are detailed in next section 6.12. Finally, samples are annealed for 24 hours in an inert atmosphere before the contact deposition process. I use aluminium (Al) with

a thickness of 50 nm for the contacts. After contact deposition, devices are encapsulated with glass cover slips using UV-curable epoxy.

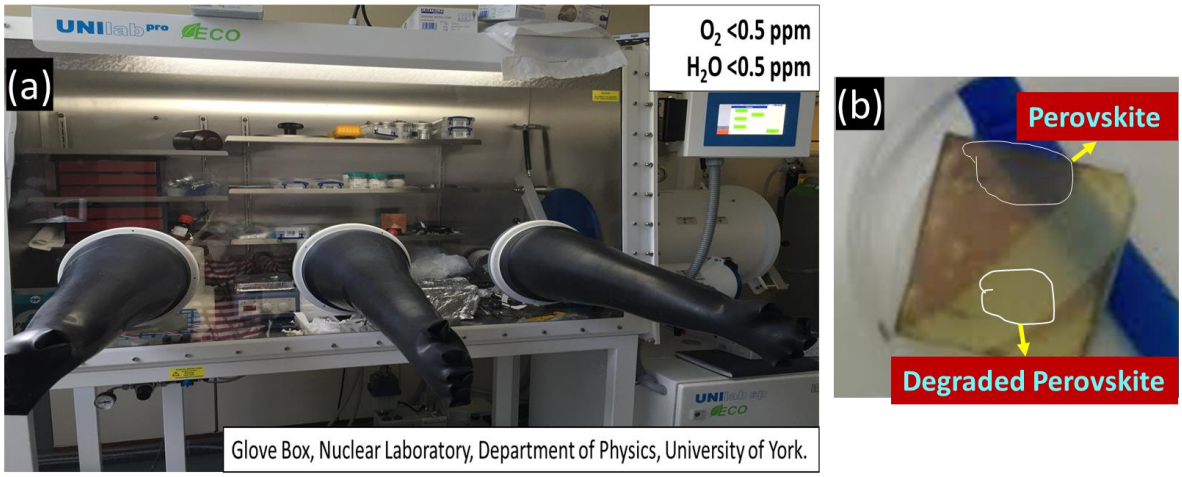

Figure 6.6. Perovskite films fabrication (a) in the available glovebox facility for controlled atm. (b) degraded film view fabricated in open air atm.; yellow film area shows PbI_2 crystals whereas brown film area is for perovskite crystals.

6.1.2 Perovskite layer fabrication

The literature describes a number of different methods for the preparation of perovskite thin films. I identified the following two methods for obtaining good quality films:

Method A: Double deposition sequential (DDS) method

Method B: Wet solvent extraction (WSE) method

The double deposition solution (DDS) [104] method targets thick perovskite films while the wet solvent extraction (WSE) is preferred for thin perovskite films [105]. I used the published recipes of both methods as a starting point and varied processing conditions such as molar concentration and spin parameters.

a) DDS method. The following two solutions are deposited consecutively by spin coating and dipping: 1. PbI_2 in dimethylformamide (DMF) 2. CH_3NH_3I. First, a layer of PbI_2 solution is spin coated at 2000 rpm for 60 sec and then annealed at 70 °C for 30 minutes. Once the film is dry, a solution of CH_3NH_3I (10 mg/ml) in 2-propanol (IPA) is spin coated at 1000 rpm for

20 seconds, followed by a final anneal at 100 °C for 1 hour. The process schematic is shown in Figure 6.7.

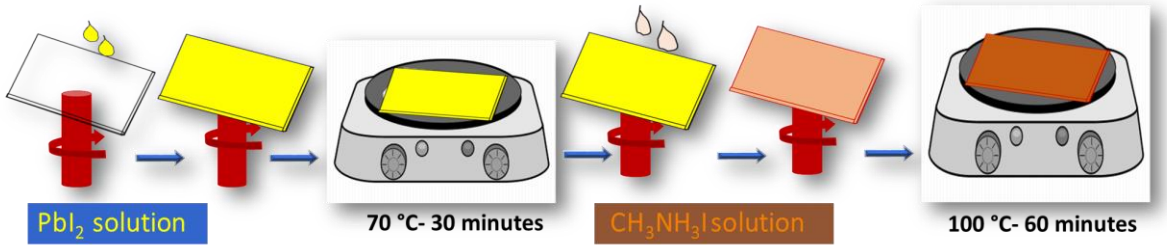

Figure 6.7. Fabrication process illustration of DDS method for perovskite films deposition.

b) WSE method, as reported by Zhou et al [105], used to produce thin films on glass. Thin films are the key to achieving strong optical confinement and the high carrier densities required for high luminescence efficiency. The WSE method consists of a single-solution deposition step by spin-coating followed by an anti-solvent dip step for drying of the film.

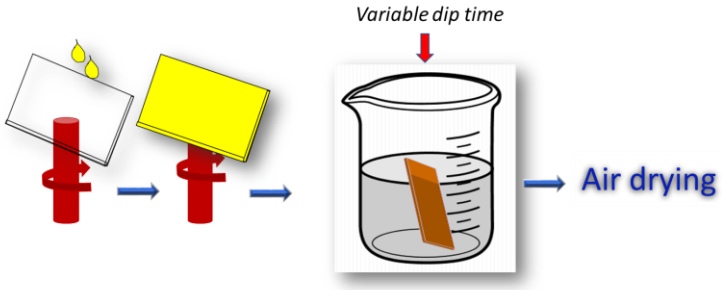

Figure 6.8. Fabrication process illustration of WSE method for perovskite films deposition.

A single precursor solution of lead iodide (PbI_2) and methylammonium iodide (CH_3NH_3I), mixed in a 1:1 molar ratio, is prepared in N-Methyl-2-pyrrolidone (NMP) solvent. The concentrations of the precursor solutions are kept at 1 M to obtain the desired film thickness and good surface coverage. The solution is spin-coated on to the glass substrate (1.5 x 1.5 mm^2) and the solvent is then extracted by dipping the sample in a diethyl ether (DEE) bath, without the need for a high-temperature annealing step, as shown in Figure 6.8. The appearance of the final perovskite film is both uniform and shiny.

6.2 Analysis:

6.2.1 Structural analysis:

A Raman setup (Horiba XPLORA) with a 532nm laser is used. The CCD detector has 1650x200 pixels with a spectral resolution of 1-1.5 cm^{-1}/pixel. Raman spectroscopy is mainly used in order to confirm the phase purity of the perovskite films. The Raman spectra were collected for encapsulated films in order to avoid atmospheric exposure and degradation. The laser power used is ~1 mW to account for the photosensitivity of the material (recommended ≈10 μW). For higher powers, degradation of the film can be observed, e.g. at the exposed spot position in Figure 6.9 (a) referred with the red marked circle. The orange colour in the circle indicates the PbI_2 phase and gives rise to high background bands for glass, indicating that after deterioration, the perovskite layer gets transparent [106]. It is therefore clear that great care must be exercised when taking these spectra, and that the exposure dose should be kept to a minimum. Two example spectra for samples processed with the DDS and WSE methods shown in Figure 6.9 (b). The spectra exhibit peaks at 97, 110 and 250 cm^{-1}, which are attributed to the lead Iodide based perovskite. [106] The bump at position 250 cm^{-1} is related to the methyl amine torsional mode while the broadened band at position 110 cm^{-1} correspond to the lead Iodide stretching mode and the methyl amine liberation mode.[107] The band position at 215 cm^{-1} represents the presence of PbI_2 (impuring phase) and can be observed with intense peak at 215 cm^{-1}[108]. Absence of this peak in our samples indicates a good degree of phase purity. The absolute intensity magnitude difference comes from the thickness of the films. The relative intensity of the band at 110 cm^{-1}, shows some film thickness dependence. This shows inhomogeneity on a micro scale, related to degradation for thin film (WSE). This effect gets significant when the same area is exposed over a long time where the background noise increases due to the transparency of degraded perovskite film. The next structural analysis method is X-ray diffraction (XRD), which provides information on the

crystal structure. I used a diffractometer made by SmartLab 9 kW Thin Film type F, Rigaku). The indexed peaks in Figure 6.10 confirm that all four methods produce perovskite crystals of tetragonal phase. Here, it is important that the characteristic Bragg peak for PbI_2 is typically depicted at 12.1 degrees (001), and its absence confirms the perovskite phase purity. The strong characteristic peaks at 14.08°, 28.41°, 31.85°, and 43.19° indicates the (110), (220), (222), and (330) planes in $CH_3NH_3PbI_3$.

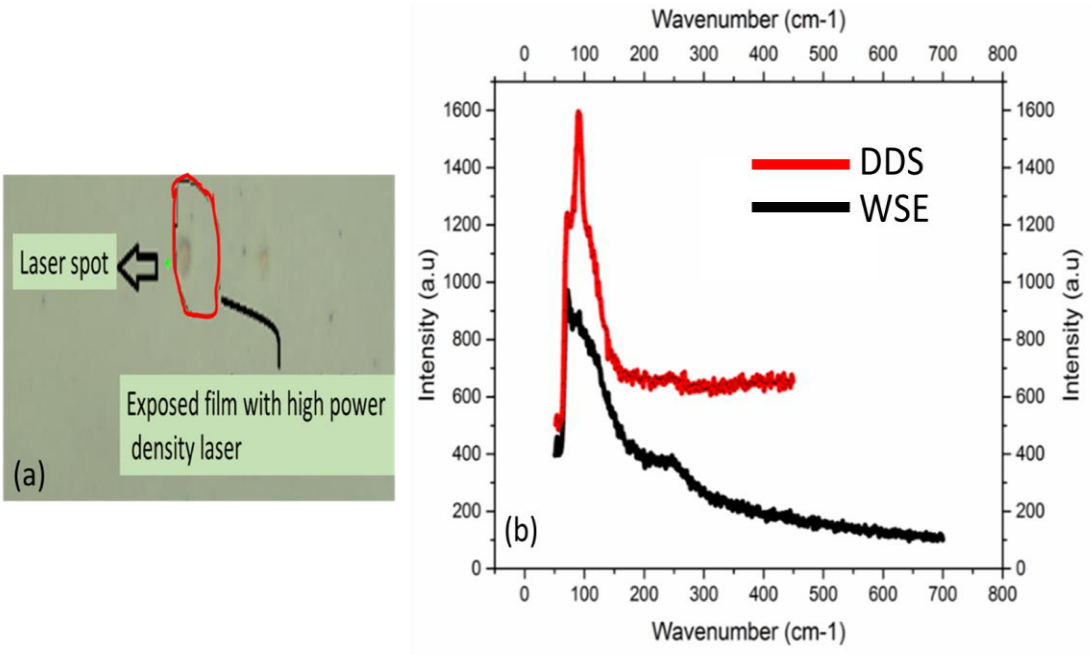

Figure 6.9. (a) Evidence of laser power deterioration on perovskite film under RAMAN testing. (b) Raman spectra for perovskite films processed using sequential solution deposition (SSD) and wet solvent extraction (WSE) methods.

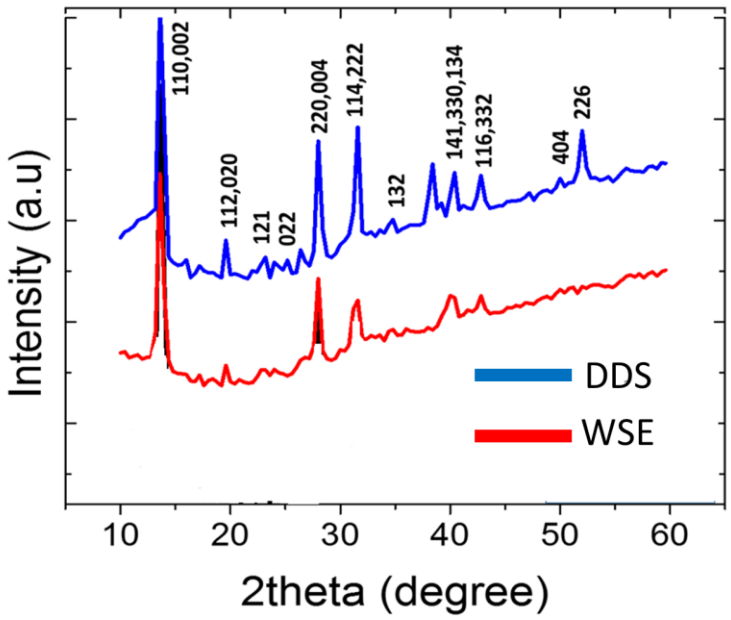

Figure 6.10. X-ray diffraction patterns of tetragonal-phase iodide based perovskite films synthesized by DDS and WSE.

6.2.2 Morphological Analysis

The morphological analysis was carried out by scanning electron microscopy, using a JEOL JSM7800F instrument. The voltage was kept below 2 kV to avoid charge accumulation on the sample. For the DDS method shown in Figure 6.11 films are fabricated using different concentrations to study film coverage. Of the three chosen concentrations, only 1 M showed a relatively high fill factor, while the 0.75 M and 0.5 M showed gaps in the packing density, which are not desired. Once electrical contacts are added to these films, such gaps would cause shunt paths, hence a highly packed film is favourable. Clearly, higher packing density also increases optical absorption.

SEM micrographs for WSE fabricated thin films are shown at low and high magnification in Figure 6.12. The films are unifom and densely packed with ≈100 nm average grain size. The small grain size is key to control thin film formation compared to other methods involving heat annealed films.

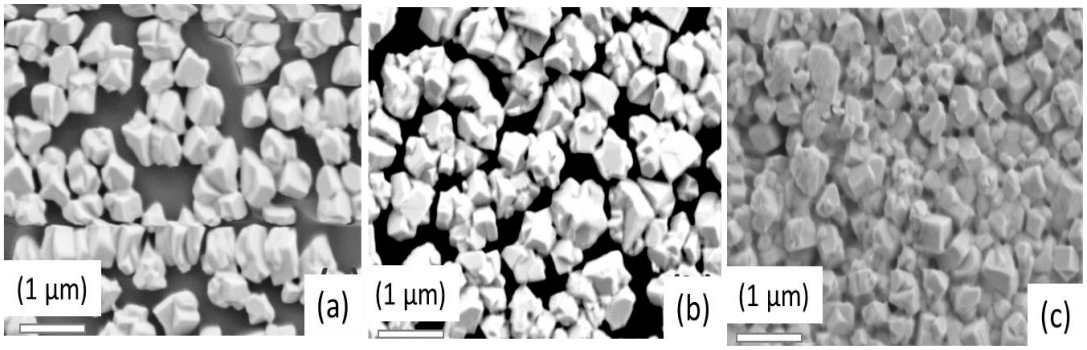

Figure 6.11. Scanning electron micrographs for DDS processed films at different molar concentrations. (a) 0.5 M (b) 0.75 M (c) 1 M.

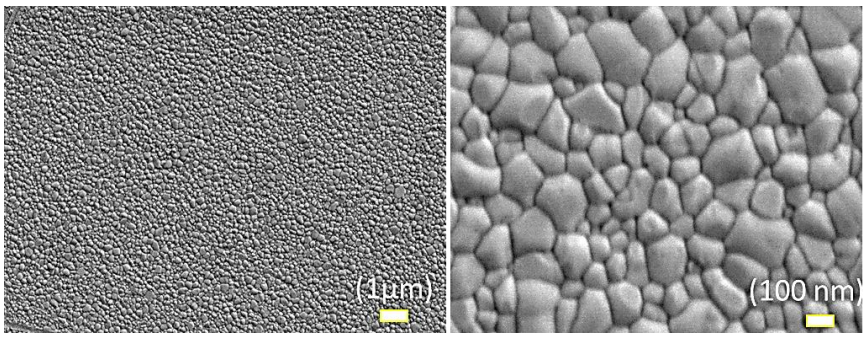

Figure 6.12. SEM micrographs for WSE processed thin films at different magnifications. Left:1µmscaleBottom:100nm scale

6.2.3 Electrical measurements

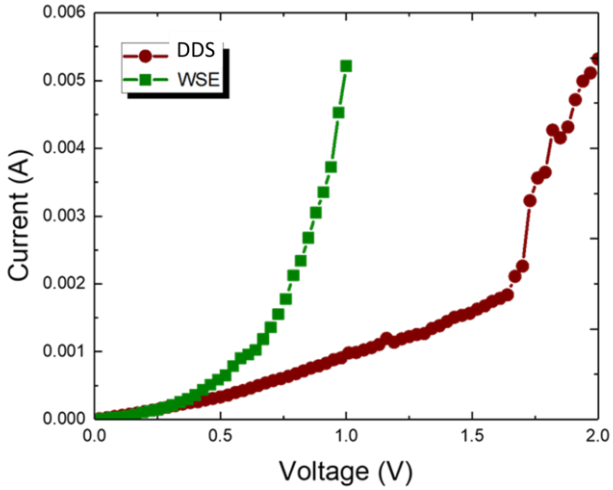

Figure 6.13. Diode characteristics of perovskite films sandwiched structure between HTL and ETL, fabricated using SSD and WSE methods.

In Figure 6.13, perovskite films fabricated using SSD and WSE method are characterized in solar cell structure under dark. The curves show non-ideal character which may be attributed to the lower shunt resistance in the devices. In the literature, the highest perovskite solar cell has an efficiency of 22.1% [109] is reported. A precise detailed study is required here to individually characterize each layer in the solar cell to determine chemical carrier's dynamics. Also, solution processed solar cells require interfacial study analysis which are crucial for high efficiency. Given the difficulties with constructing high quality solar cells over the short time of my project, I decided to explore the optoelectronic properties of perovskites. I conducted photoluminescence (PL) as well as gain and loss measurements, all performed with a pulsed, frequency-doubled YAG laser (pulse length 400 ps, repetition rate 500 Hz) at 532 nm (PhotonicSolutions PowerChip NanoLaser). The setup is shown in Figure 6.14. The pump intensity was controlled by a selection of calibrated neutral density filters. The excitation energy was measured with a ThorLABs powermeter (PM100D) and the emission spectra were recorded on a Thorlabs spectrometer (CCS175/M).

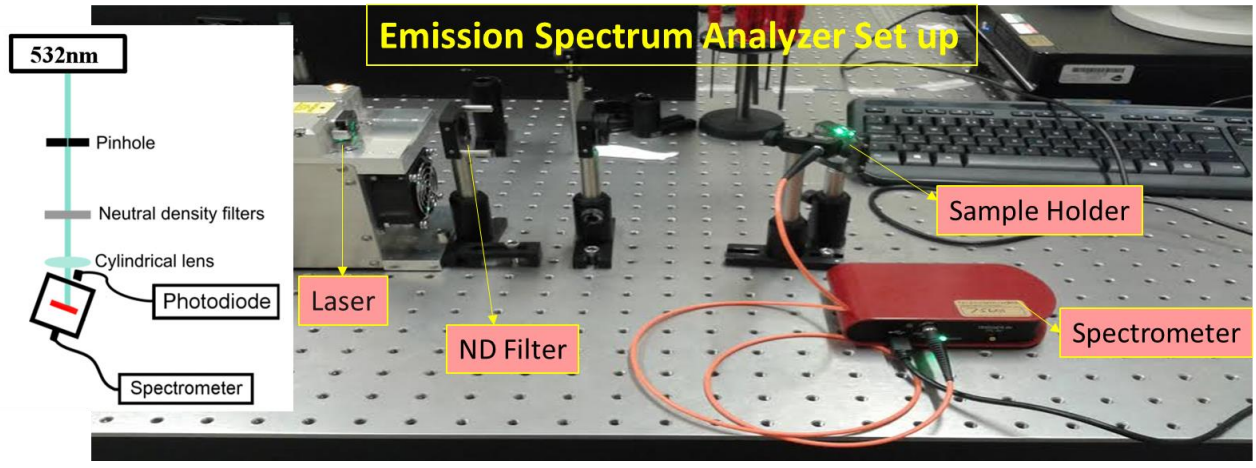

Figure 6.14. Optical characterization setup for photoluminescence, gain and loss measurements for perovskite films.

A comparison of emission spectra for films made by the SSD and WSE methods is shown in Figure 6.15. The SSD film shows a broad PL spectrum of 30-40 nm width, as expected, while

the WSE film showed a much sharper spectrum. This narrow spectrum is quite remarkable and was not expected, so I decided to investigate it further.

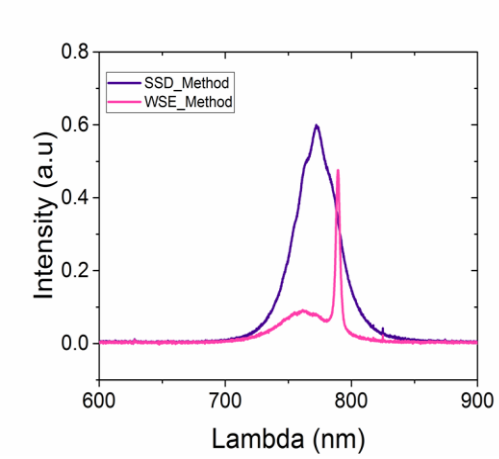

Figure 6.15. PL spectra comparison for DDS and WSE processed films.

In the WSE method, the film thickness and quality are well controlled by varying two parameters: (a) spin speed and (b) dip time in anti-solvent.

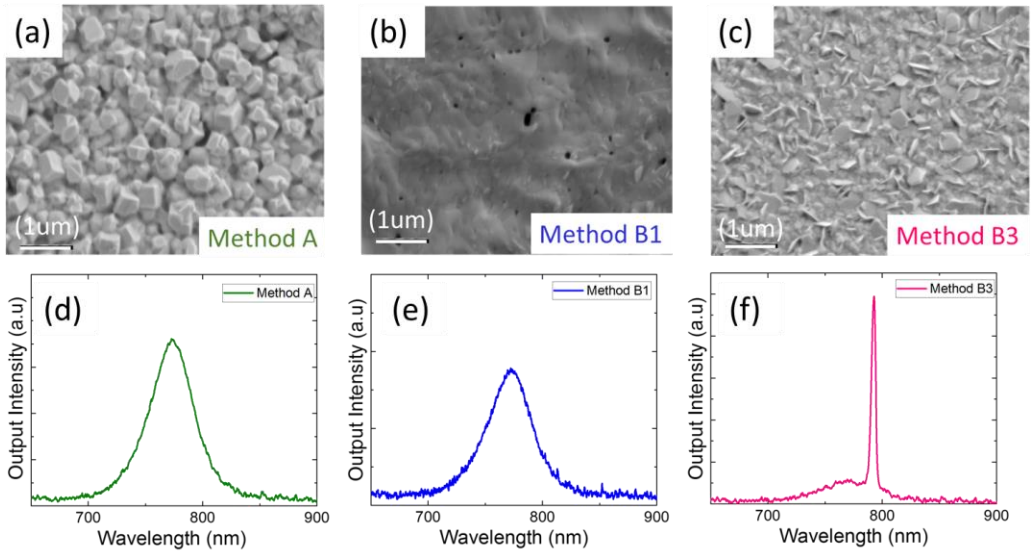

Figure 6.16. Perovskite films, fabricated on bare glass substrates using three different methods, Method A (DDS), Method B1 (WSE, 0 sec) and Method B3 (WSE, 120 sec). (a), (b), (c) Morphology comparison. (d), (e), (f) PL spectra comparison.

The dip time is a very important parameter as it impacts on the crystallization of the film. I noted that by increasing the dip time from 0 to 120 seconds, a better coverage on the glass

surface can be achieved, which is a primary challenge in the synthesis of thin perovskite films. I also noted that the dip time critically determines the PL linewidth. So, to investigate further, I introduced the dip time as a parameter of study.

In the following, I refer to DDS as method A and to WSE as method B, with B1, B2 and B3 referring to different dip times. Films for a dip time of 0 sec are referred to as B1, 3 sec as B2 and 120 sec as method B3, respectively, detailed in Table 6.1. The morphology and PL spectra are compared in Figure 6.16.

6.3 Random lasing in uniform perovskite thin films

As a result of the dip time study, I realised that the observed narrow peaks may be due to laseing action, which is investigated next. Lasing in perovskite materials has already been observed both in engineered and in self-assembled resonator structures, such as microcrystal networks, with the low cost and the simple solution-based process being a particular attraction. The ultimate in simplicity, however, would be to observe lasing from a continuous thin film, which has not been reported yet and will now be investigated.

6.3.1 Lasing: Introduction

The word laser is an acronym of Light Amplification by Stimulated Emission of Radiation. Laser devices are used for the amplified emission of light beam at a narrow with a well-defined wavelength of the electromagnetic spectrum. In a laser device, two fundamental elements are considered as follow:

1. A gain material is used where the energy levels of the atoms are used to increase the output power of the incident light as it propagates with in the material and encourages stimulated emission.
2. Energy is pumped to the gain material to excite the atomic states to the higher energy levels to create a population inversion using a pumping system. This

system typically is optical and electrical. Stimulated emission process dominates over light absorption process if the atomic system has a large population of atoms in an appropriate excited state.

A simple laser is typically constructed by placing a gain material with the gain coefficient $\alpha_> 0$ between two parallel mirrors as shown in Figure 6.17. For $\alpha_> 0$, the material must have a higher population of excited atoms where cavity is formed by two parallel mirrors. One of the mirrors has 100 percent reflectivity (R = 1), whereas the other mirror has lower reflectivity (R < 1) to allow output from the formed cavity. The light is reflected back and forth through the gain material by exciting more and more atoms to the higher energy level where the decay of these atoms results in light amplification[110].

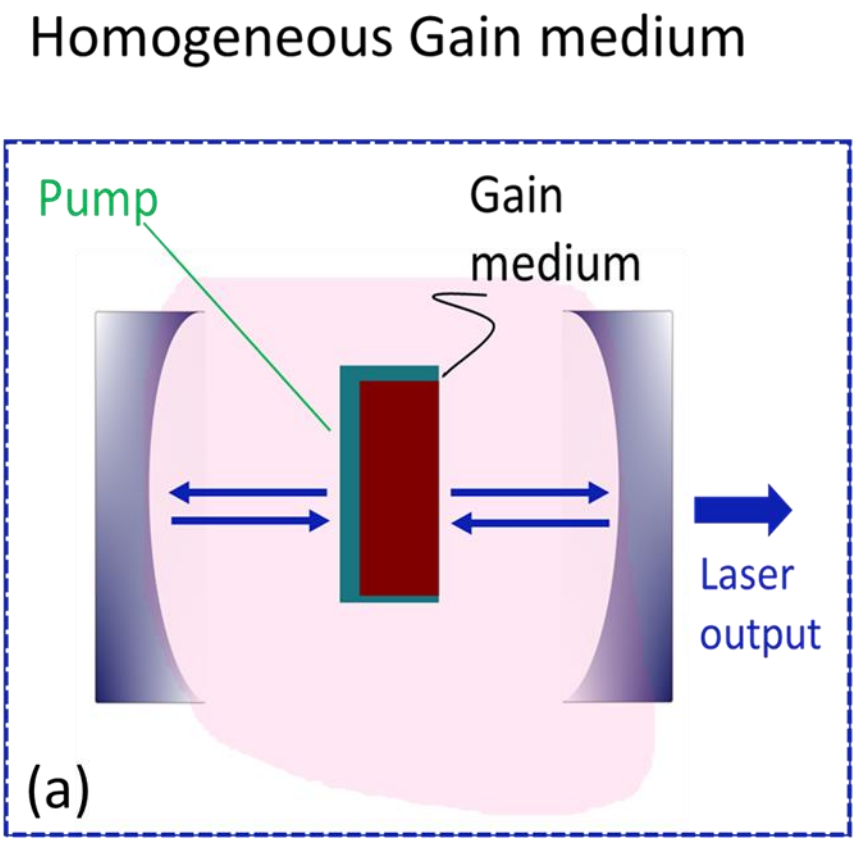

Figure 6.17. A simple laser cavity.

6.3.2 Perovskite as a gain material

LED [100,111] and laser operation[112] in perovskites has already been observed over a broad wavelength range. The processing flexibility, simplicity and low-cost of the precursor materials are major drivers with a view towards ultra-low cost applications, such as wearable electronics or single-use devices for medical diagnostics or therapeutics. The ultimate in simplicity for a laser device, naturally, is a laser that creates its own feedback through scattering in the gain medium, i.e. a random laser. We now investigate whether such a random laser can be created by simply controlling the solution-processing conditions of the perovskite material. It is now well established that the family of lead triiodides, i.e. materials with the PbI_3 ion at the core of its crystal unit cell and a bandgap around 1.6 eV, forms the most efficient and stable material for optoelectronic applications.[113,114]An approximately 500 nm thick film of this material is sufficient to absorb light over the entire visible spectrum, with very low sub-gap absorption. Bipolar charge is transported in solid-state films with good ambipolar charge carrier mobility (5-10) $cm^2V^{-1}s^{-1}$ for electrons and 1-5 $cm^2V^{-1}s^{-1}$ for hole carriers[115,116] long carrier lifetime (10 ns) and sufficiently large diffusion length (micrometer-scale),[117] which leads to low non-radiative recombination in the bulk.[118] The perovskite material family also provides attractive optoelectronic properties, including strong photopumped light emission,[119,120]bright electroluminescence,[121,122] and the observation of optically pumped lasing, along with wide wavelength tuneability. [100,123,124]

The laser configurations demonstrated so far[125] include triangular or hexagonal platelet structures utilising whispering gallery modes (WGM) [126] or planar wire configurations that form Fabry-Perot cavities [127]. Similarly, self-organised microcrystalline rod-shaped structures have been used as resonators.[123] Perovskite distributed feedback laser (DFB) lasers have also been studied recently, with gratings made by electron beam, UV and holographic lithography techniques.[128–130] Typical laser thresholds are in the 100 $\mu J/cm^2$

regime.[131] The lowest threshold, to our knowledge, has been observed from a vertical cavity surface emitting laser (VCSEL) configuration, where perovskite thin films have been sandwiched in a layered structure with a minimum threshold at below 1 μJ/cm^2.[132]

All of these observations require carefully engineered nanostructures, the addition of external layers or very controlled crystal growth conditions to achieve a desired configuration that can act as a laser resonator. In order to meet the requirements of a true low-cost technology, it would be preferable to keep the process steps as simple as possible. We now show a possible route towards such an inexpensive technology by demonstrating high-performance (threshold ≈ 10 μJ/cm^2) random lasing from a uniform perovskite film. We study perovskite materials of the methylammonium lead triiodode ($CH_3NH_3PbI_3$) family by investigating systematically the conditions required for achieving (and avoiding) random lasing and using optical gain and loss measurements to explain the different operating regimes.

6.3.3 Fabrication and analysis of lasing/nonlasing perovskites films

As detailed above, I used the WSE method for methods B1, B2 and B3 with 0 sec, 3 sec, and 120 sec dip time, respectively. I compared these methods to films made using DDS (Method A). The details of methods used are summarized in Table 6.1. Following the initial PL comparison shown in Figure 6.16, I now show a comparison of the photoluminescence characteristics of all four methods, together with their surface morphology, in Figures 6.17 and Figure 6.18. We note that films produced by methods A and B1 only show photoluminescence, while films produced by methods B2 and B3 films exhibit lasing/multimode lasing, all using the same excitation energy of 212 μJ/cm^2. From the SEM images, I note that method A produces films with grains of large size (~500 nm), while method B1 produces very smooth films and method B2 and B3 produce films of intermediate roughness (Rrms); the respective values given in Table 6.1.

Table 6.1. Synthesis parameters for four methods illustrated in Figure 6.20 and 6.21.

Method ID	Precursor solvent	Deposition method	Dip time /sec	Spin speed /rpm	Annealing time /min	Film roughness/nm	Film thickness /nm
Method A (DDS)	Dimethylfo-rmamide	Double step	N/A	2000	60 @100 °C	80	275 ± 12
Method B1	N-Methyl-2-pyrrolidone	Single step	0	2000	0	18	230 ± 20
Method B2	N-Methyl-2-pyrrolidone	Single step	3	2000	0	24	81 ± 5
Method B3	N-Methyl-2-pyrrolidone	Single step	120	2000	0	26	56 ± 10

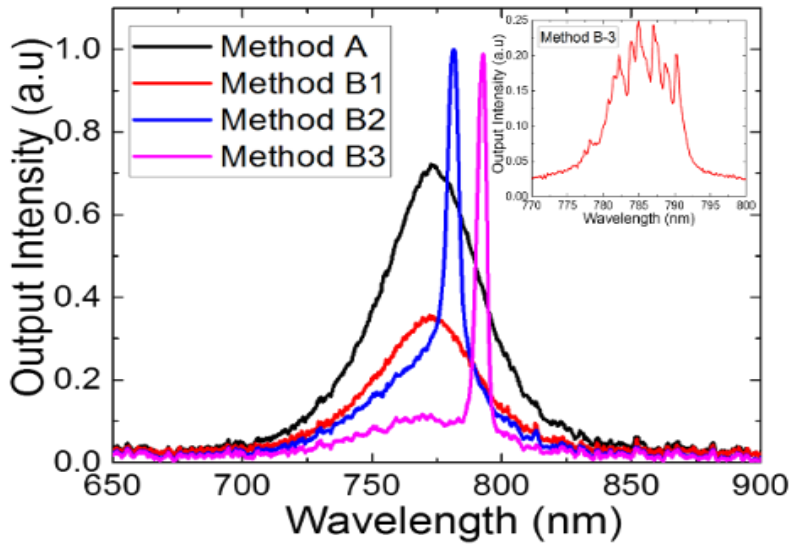

Figure 6.18. Output emission spectra of perovskite films produced by the four methods, collected at an excitation energy of 212 μJ/cm^2. The inset shows multimode lasing observed for a higher resolution scan with a film prepared using method B3.

The uniformity of surface coverage is shown in the cross-sectional view of films for method A and method B3 as an inset in Figure 6.18 (i), (j).

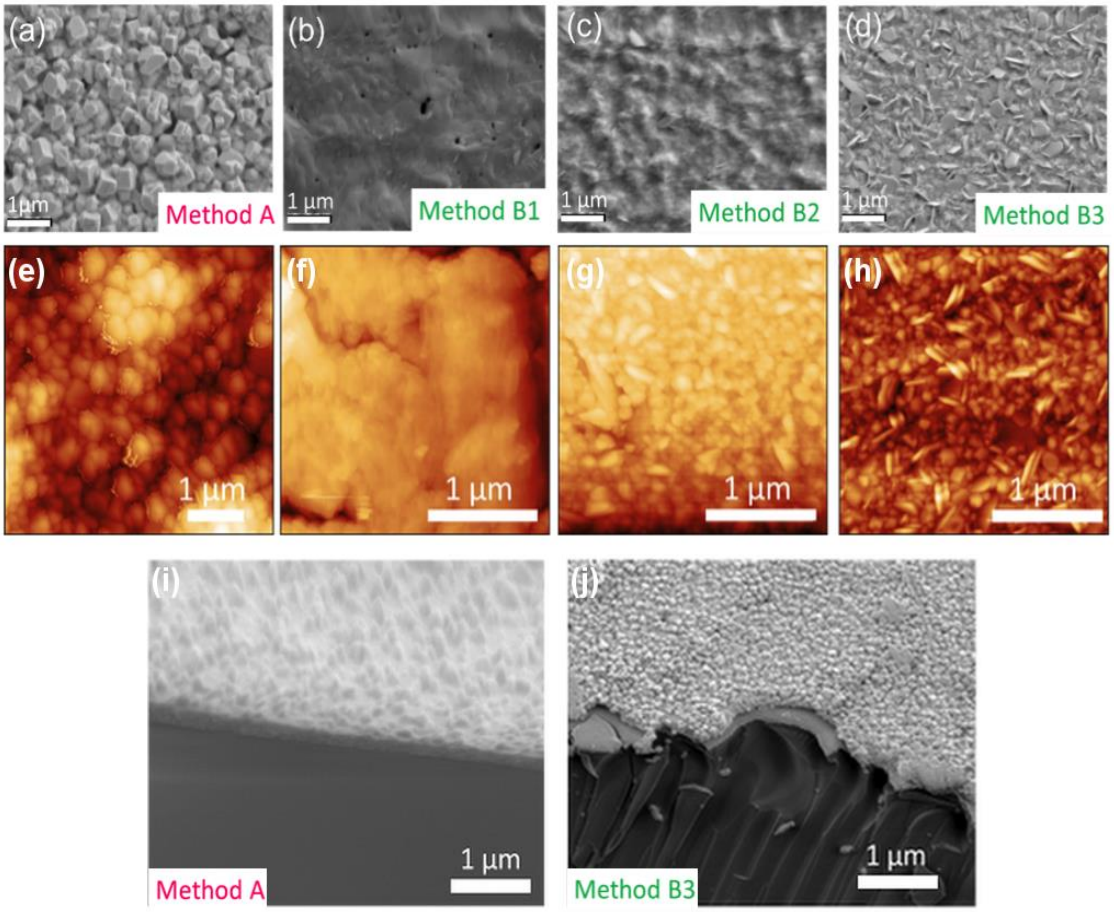

Figure 6.19. Morphology comparison for the four different methods. (a): SEM image of perovskite film synthesized by the double deposition step method (DDS, method A). (b): SEM image of perovskite film synthesized via solvent extraction method with 0 sec dip time. (WSE, method B1). (c) and (d): SEM images of perovskite films synthesized via solvent extraction method with 3 second (Method B2) and 120 second (Method B3) dip time; (e-h): AFM images of films produced by Method A, B1, B2 and B3; (i-j): cross-sectional SEM images of films produced by method A and method B3, viewed at an angle of 45°.

The existence of a crystalline phase is indicated by indexed X-ray diffraction patterns as shown in Figure 6.19. The X-ray analysis confirms that all four methods produce perovskite crystals. The 14.1°, 24.4° and 28.4° diffraction peaks are associated with the (110), (202) and (220) planes of the tetragonal phase of $CH_3NH_3PbI_3$ perovskite. Next, I study the luminescence behaviour of the films in more detail, using pump intensities up to 100 µJ/cm^2.

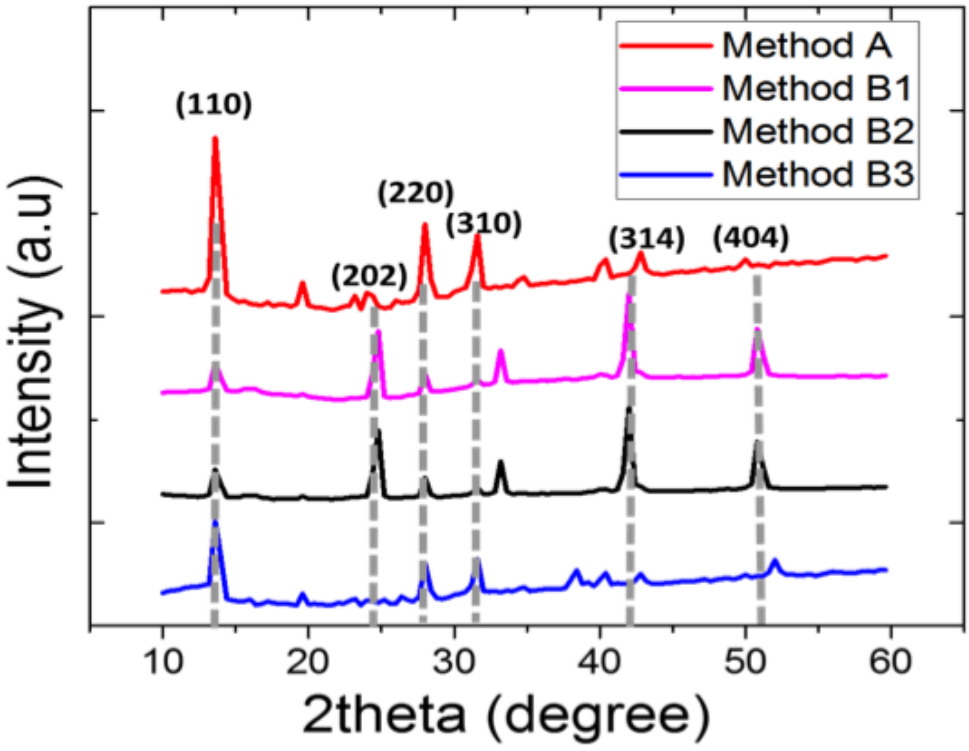

Figure 6.20. X-ray diffraction patterns of tetragonal-phase iodide based perovskite films synthesized by four methods.

A lens was used to shape the excitation beam into a spot of 1.33 mm in diameter and the emission spectra were collected by a Thorlabs spectrometer (CCS175/M) at normal incidence. The difference between the films made by method B1, B2 and B3 is particularly striking, as they only differ in a single fabrication parameter, namely the dip time in the anti-solvent. For method B1, with 0 second dip time, I observe broadband photoluminescence for all pump intensities, which is typical for lead iodide perovskite films, shown in Figure 6.20. The PL intensity increases linearly and the linewidth remains constant near 45 nm (FWHM). In contrast, Figure 6.21 (a) and (b) show films prepared by method B2 (3 sec) and method B3 (120 sec) excited at different pump intensities, with a laser threshold of 33 $\mu J/cm^2$ and 10 $\mu J/cm^2$, respectively.

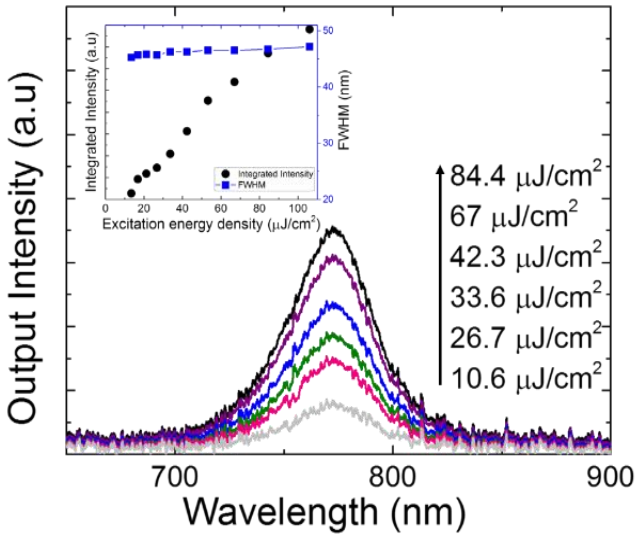

Figure 6.21. Emission spectra of film prepared by Method B1 excited with intensities as shown. Inset: integrated emission intensities and the FWHM of the PL spectra as a function of excitation energy density.

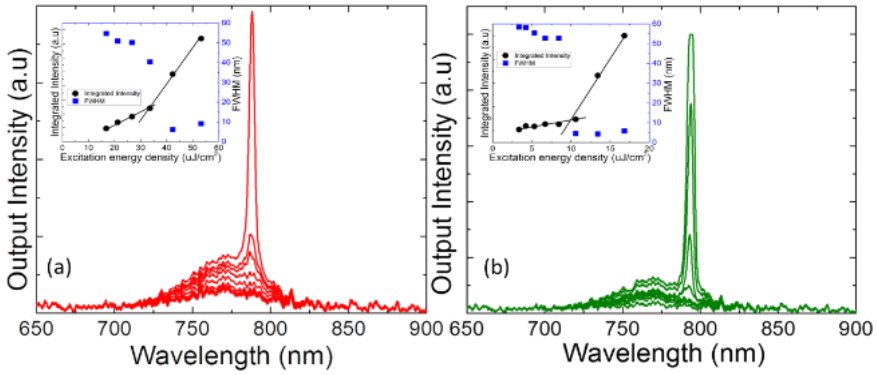

Figure 6.22. Top emission spectra of (a) Method B2 (3 sec) and (b) Method B3 (120 sec) films excited with a circular excitation beam with a diameter of 1.33 mm. Laser thresholds are shown in the inset along with the FWHM.

Further evidence for random lasing action is shown in Figure 6.22 where I observe (a) single mode, (b) dual mode and (c) multimode lasing. The multimode lasing in Figure 6.22c is commonly observed for random lasers, while the single and dual mode lasing is rather unique. These spectra were taken for the same film made from method B3 under a pump intensity of 13.4 μJ/cm^2 at different positions on the film.

Moreover, the emission from the films prepared by method B3 is further investigated with different pumping geometries, as well as checking for amplified spontaneous emission (ASE). The dual mode lasing behaviour as a function of pump intensity, observed in Method B3, is shown in Figure 6.23 a and 6.23 b. Mode 1 and Mode 2 lasing occurs when the pump intensity is increased to 11 μJ/cm^2 and 13 μJ/cm^2 respectively, when the sample is excited with a circular beam with a diameter of 1.33 mm.

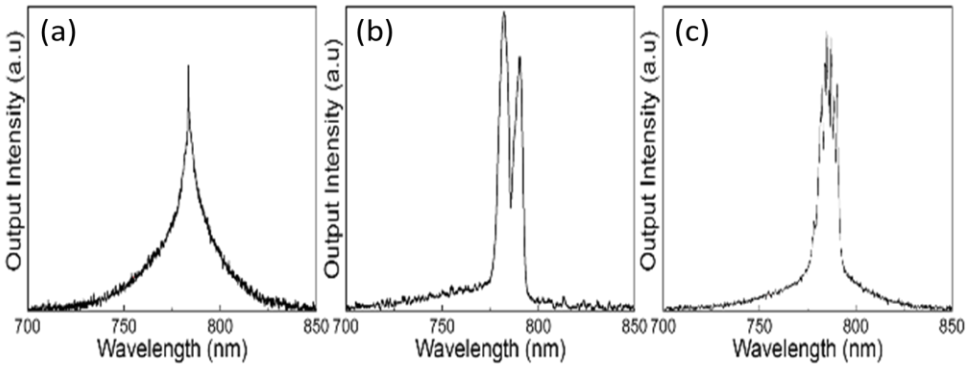

Figure 6.23. Random lasing observed in a perovskite uniform thin film: (a) Single mode lasing; (b) Dual mode lasing; and (c) Multimode lasing. All spectra were taken from the same film prepared by method B3, but by pumping in different positions using a fixed excitation intensity of 13.4 μJ/cm.

It is worth noticing that the lasing modes include background PL, both when collected from the surface and from the edge; one may observe ASE or lasing, with the difference not always being obvious. In order to verify that we are indeed observing lasing action, I also studied the ASE, as ASE provides a similar step-change that can easily be mistaken for lasing. One typically expects the ASE threshold to be higher than the lasing threshold and its FWHM broader than the lasing peak. The presence of an ASE threshold also determines the film's compatibility as a gain medium and allows us to measure the gain and loss coefficients. For the ASE measurements, I follow the procedure commonly used for examining organic semiconducting gain materials, whereby we excited the film with a stripe-shaped beam in 1.6 x 0.4 mm^2 dimension and detect the emission from the edge of the film.

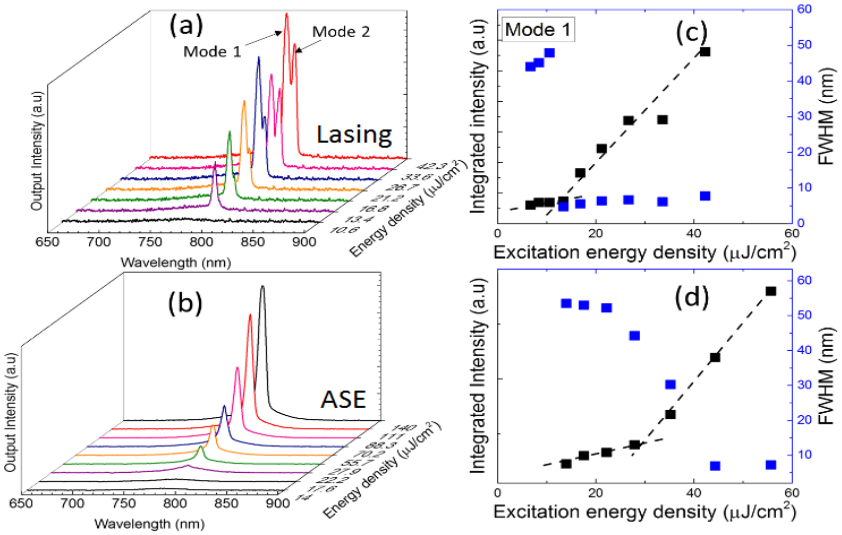

Figure 6.24. All spectra collected are from method B3 (120 sec) films. (a) Surface emission spectra for a film excited with a circular excitation spot with a diameter of 1.33 mm, with a laser threshold of 11 μJ/cm^2 shown in (c) along with its Full Width Half Maximum (FWHM); (b) Amplified spontaneous emission spectra of films excited with a narrow stripe in 1.6 x 0.4 mm^2 dimension and detected from the edge of the sample. The ASE threshold of 39 μJ/cm^2 is shown in (d).

The long axis of the beam is oriented perpendicular to the edge of the sample where the emission is monitored, thereby forming a gain-guide which transports the spontaneously emitted light to the edge of the film while getting amplified along the way. I measure an ASE threshold of 39 μJ/cm^2 for Method B3 (Fig. 6.23b and 6.23d), which is significantly higher than the lasing threshold of 12 μJ/cm^2 for the same film excited with the same stripe-shaped beam. To understand the mechanism of the random lasing behaviour, an interplay is considered between gain and scattering, as compared to a regular lasing cavity in Figure 6.24. Random lasing can be understood as a random walk that forms an open or a closed loop. Alternatively, one can think of it as constructive interference between multiple scattering events, which is sharpened by the gain. In either case, it is essential to have multiple scattering events N in the thin film, separated by the mean free path length $L_{scatter,}$ such that the total pathlength before the light is scattered out is longer than the gain length L_{gain}, i.e. N

$L_{scatter} > L_{gain}$. If the scattering is too weak, N is too small even though $L_{scatter}$ may be large; on the other hand, if the scattering is too strong, the mean free path $L_{scatter}$ is too short and the light may be scattered out before experiencing significant gain; note that $L_{scatter}$ here refers to in-plane scattering. Therefore, it is essential that a certain amount of scattering occurs and that scattering and gain interplay correctly.

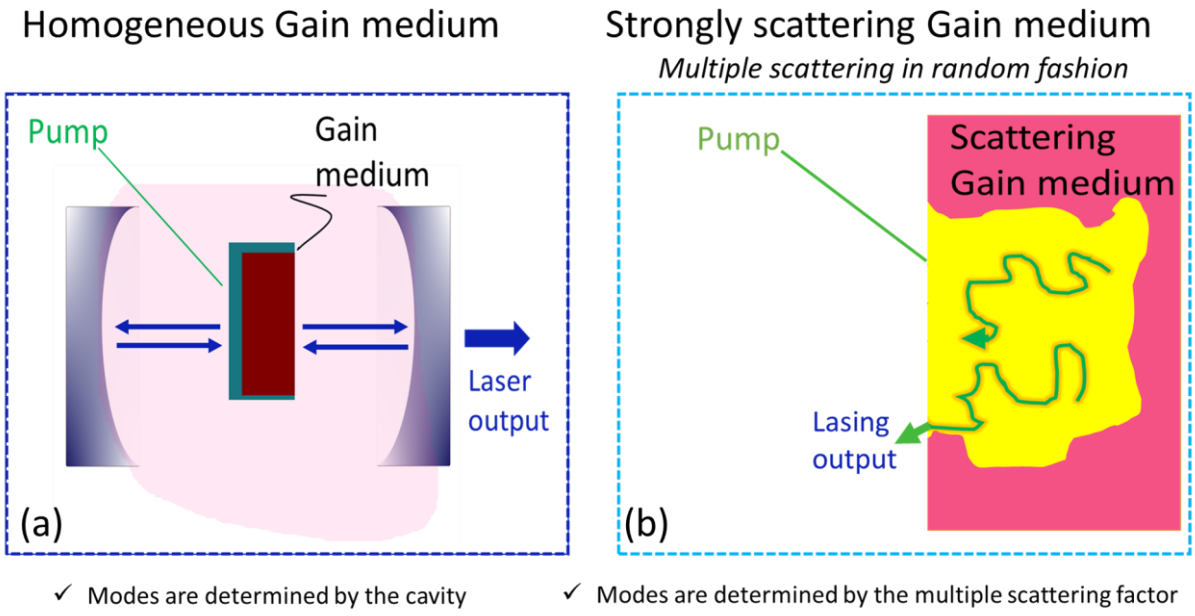

Figure 6.25. Comparison of regular lasing vs random lasing cavities (a) Homogeneous gain medium is used for lasing phenomenon. (b) Scattering gain material used for random lasing phenomenon.

To determine the gain of the films, the variable stripe length method is used whereby the output intensity, $I(\lambda)$ is related to the gain coefficient of the material by following relation:

$$I(\lambda) = \frac{AI_{\circ}}{g(\lambda)}(exp^{g(\lambda)L} - 1) \qquad (6.1)$$

where L is the length of the stripe incident on the film, A is a cross-section constant, I_o is the pump intensity and $g(\lambda)$ is the net gain coefficient of the material. I then use a log-linear plot for the experimental data and place a linear fit to extract the gain values for the three films made using Method A, B2 and B3 (see Figure 6.25). The length of the excitation stripe is

varied between 0 to 3 mm with an excitation energy density of 500 μJ/cm^2. The resulting gain values for Materials A, B2 and B3 are shown in Table 6.2. It is clear that the gain value is highest for Method B3, as expected from its low lasing threshold. We also note that the gain values of our films are comparable to other solution -processed perovskite thin-films reported in the literature.

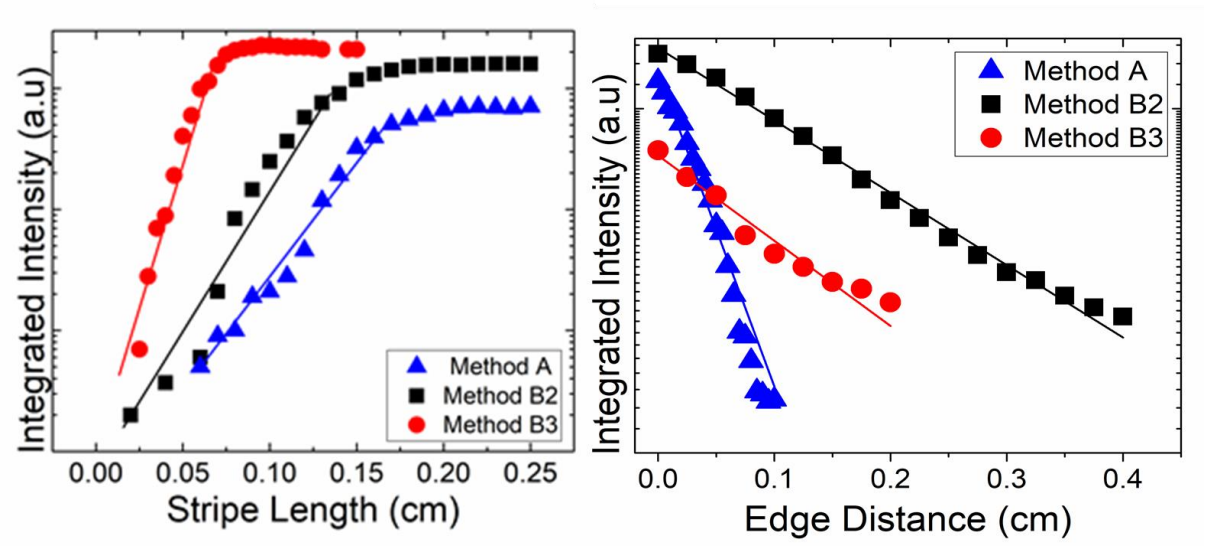

Figure 6.26. Variable stripe length method based measurements for gain coefficient in perovskite films; (b) output emission intensity as a function of un-pumped region distant from the edge of the sample to determine loss coefficients in samples prepared by Method A, B2 and B3.

For the loss coefficient measurements, a similar method is used, whereby the pumped length is held constant at 2 mm, and the stripe is moved away from the edge of the film to increase the un-pumped area where the amplified light travel through. The net loss then follows the simple Beer-Lambert law,

$$I = I_{\circ} e^{(-\alpha x)} \qquad (6.1)$$

where x is the distance between the film edge to the end of the stripe and α is the loss coefficient. Please note that this method measures the out of plane scattering loss including

self-absorption loss. The experimental data is again plotted log-linearly. From the fit to the linear section of the graphs, we extract the loss values as shown in Table 6.2.

6.3.4 Semi-quantitative explanation for the observed lasing/nonlasing phenomena

Now a semi-quantitative explanation can be provided for the observed lasing/nonlasing phenomena also illustrated in Figure 6.26. Intuitively, one would expect Material A to be the best candidate for random lasing, as the SEM image shows a very "blocky" appearance, which suggests strong scattering. Correspondingly, we measure a high scattering loss of 19.8 cm^{-1}. Nevertheless, as Material A exhibits less gain than Material B3, it is concluded that the effective pathlength $NL_{scatter}$ is shorter than the gain length L_{gain}, so lasing does not occur.

Table 6.2. Gain and loss coefficient values.

Method ID	Gain coefficient (cm^{-1})	Loss coefficient (cm^{-1})
Method A	28.9 ± 1.0	19.8 ± 1.0
Method B2	16.8 ± 1.5	2.9 ± 0.1
Method B3	70.1 ± 2.6	4.6 ± 0.3

It may also be the case that the out-of-plane scattering component is too strong compared to the in-plane scattering component. For Material B1, the opposite is true: the scattering is weak and the gain is too low, which again precludes lasing. Materials B2 and B3, however, exhibit a good balance between gain and scattering such that the $NL_{scatter} > L_{gain}$ condition is met and lasing can occur. The lifetime of the perovskite films is relatively short, as the films are not encapsulated in any way. Therefore, the lasing threshold increased by approximately 20% after 48-hour exposure to air and light. For pumping at 500 Hz (17 μJ/cm^2) in air, the random laser output decreased to 80% of its initial maximum after 105 pulses as shown in Figure 27.

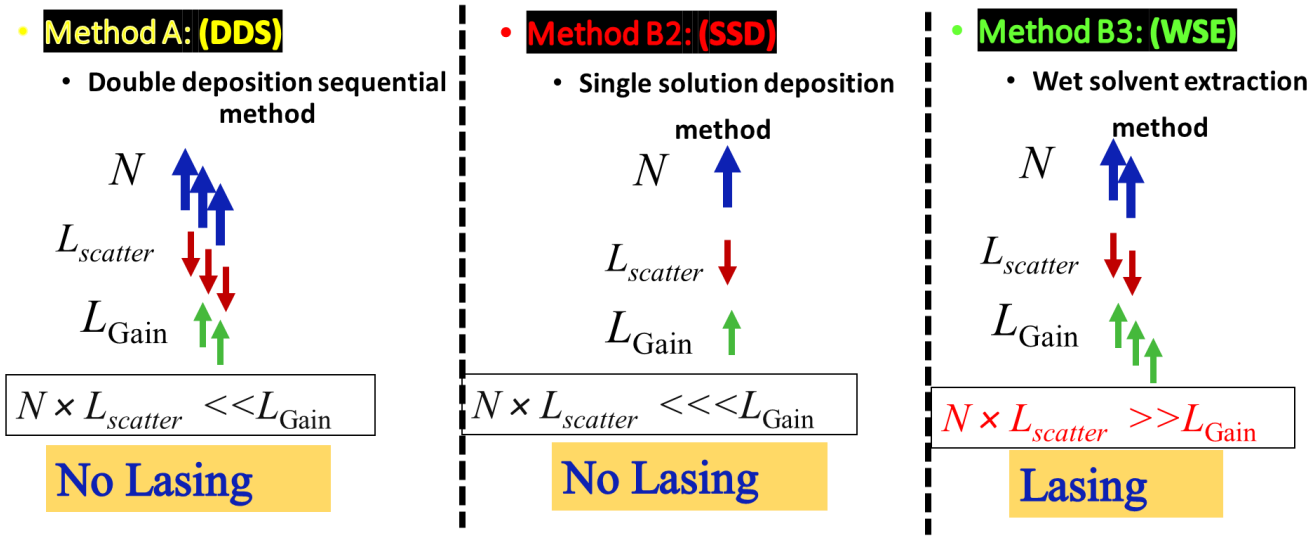

Figure 6.27. Semi-quantitative explanation for the observed lasing/nonlasing phenomena in all three methods.

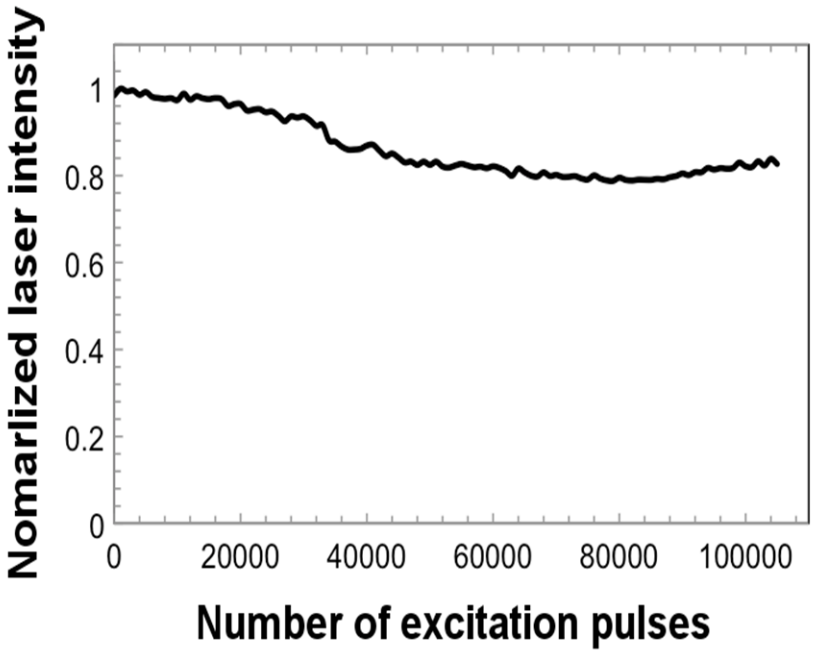

Figure 6.28. Lasing stability of random laser under 500 Hz pumping rate.

In summary, I have found a simple room temperature method for depositing uniform perovskite films that exhibit random lasing action. The films show strong amplification as well as all the features expected from a random laser, e.g. nonlinear output curve, linewidth narrowing and ASE threshold for higher pump intensity. A rather special and rarely observed feature is that some of the films exhibit

single and dual mode lasing action. I also show how to control the random lasing action by varying the dip time in the anti-solvent, as this step controls the nature of the film crystallization, which has a significant affect on optical gain, thereby determining the difference between lasing and no lasing action.

7 Chapter 7: Conclusion and outlook

I will start my concluding thoughts by reminding the reader of the main objective of this study, summarised in Figure 7.1, which is to increase the efficiency of solar cells. Solar cells are ultimately limited by the Shockley-Queisser limit which is caused by the thermalization in semiconductors. One approach to overcome this limit is to increase the efficiency by combining multiple materials with different bandgaps, e.g. in a tandem architecture. Tandem technology is already mature, e.g. in III-V materials, but much less so in low-cost materials; the question is then whether we can manipulate light to improve the efficiency. Belonging to a Photonics group, the motivation was to introduce advanced light manipulating structures into the intermediate layer of a tandem cell.

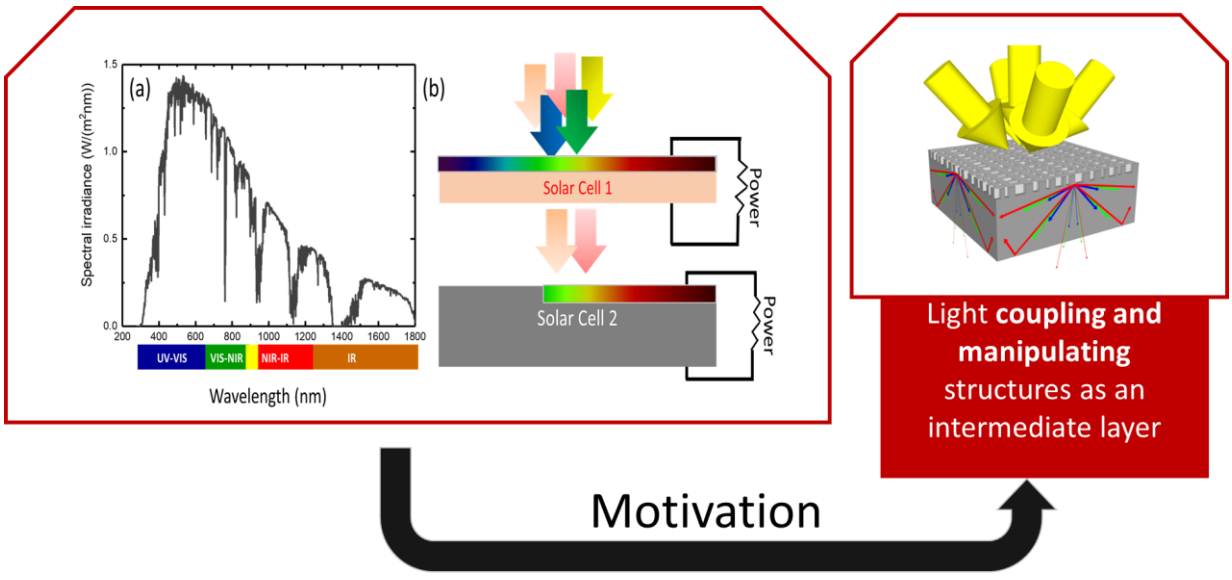

Figure 7.1. Integrating nanophotonic light management structures into a tandem solar cell.

. The light is coupled in (trapping in) and out (to transmit to the next bandgap layer) of the top and bottom cell depending on their energy band gaps. The intermediate light couplers have the potential to improve the effectiveness of the spectral absorption in each respective

solar cell. Unfortunately, due to the limited time, this goal could not be completed, yet I made progress and developed key steps towards it.

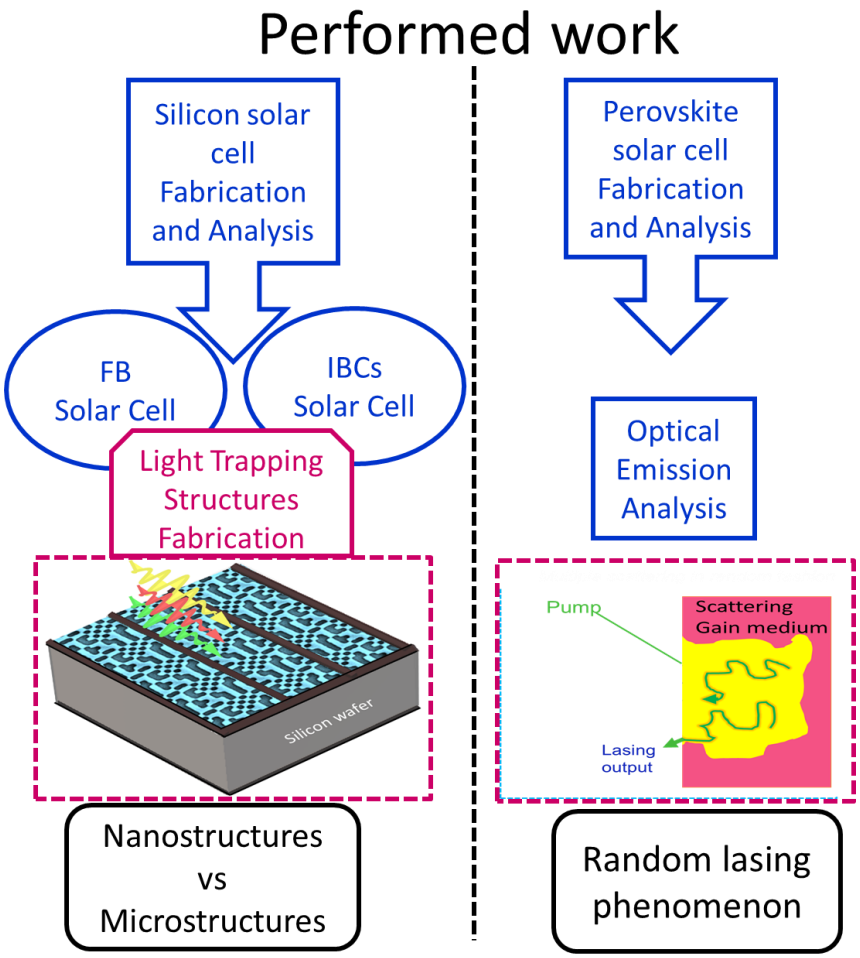

Figure 7.2. Schematic illustration of the work performed during the course of this thesis. [I would spell it as “FB, IBC Solar Cell” and “Light Trapping Structure Fabrication”]

Accordingly, I have conducted the following studies:

- Fabrication processes were developed for two silicon solar cell structures (FB, IBC) in the cleanroom facility at the York Jeol Nanocentre.
- Quasi-random light trapping nanostructures were optimized and compared with State-of-the-Art pyramid microstructures.

- The comparison of nanostructures vs microstructures was realized in real silicon solar cell devices, with the surprise outcome that dry etched quasi-random nanostructures perform better than microstructures in terms of photocurrent and overall efficiency.
- The optoelectronic properties of different morphologies of halide-based perovskites was investigated. I discovered unique random lasing action from a simple solution-processed perovskite film on glass.

7.1. Concluding remarks

Silicon is the most pervasive solar cell material in the world, and it is also the second most efficient single bandgap material available with 25.6% having been demonstrated to date; only single layer GaAs offers a higher efficiency, but it is much more expensive, so hardly used in terrestrial applications. Silicon dominates the solar panel market and currently represents a 92% share of the market capacity. To continue this progress, research and development efforts are aimed at enhancing the efficiency of silicon solar cells. One method is to thin down the silicon wafer in order to lower the bulk recombination losses and achieve a higher V_{oc} while maintaining a high photocurrent (J_{sc}) by applying efficient light trapping schemes. Light trapping schemes have mainly been developed for thin film devices where larger structures such as micron-scale pyramids cannot be applied because they would exceed the film thickness. Therefore, light-trapping nanostructures have been developed that operate on a sub-wavelength size. Many different types of structure have been studied on this premise. The novelty of my work has been to apply these nanostructures to thick film, i.e. wafer-scale devices, of thickness 180µm. The application of nanostructures to thick silicon solar cells turned out to be an interesting and important study which has surprisingly concluded their superiority compared to standard wet etched pyramids.

I will now discuss the main insights of my work chapter by chapter.

Chapter 7: Conclusion and outlook

In Chapter 1, I started with the physics of semiconductor materials to explain the working principles of a silicon solar cells, including the details of the main recombination mechanisms. The solar spectrum utilization as a function of the semiconductor bandgap material was explained including the thermodynamic limit and the Shockley-Queisser limit.

In Chapter 2, since silicon is a high refractive index material and a weak infra-red absorber due to its indirect bandgap, I introduced the importance of antireflection coating (ARC) and light trapping. The phenomena of reflection, refraction, interference and diffraction were discussed in a ray optics framework. Subsequently, nanoscale light trapping structures were introduced in the wave optics regime.

In Chapter 3, Light trapping structures were reviewed with respect to their scale and periodicity. The current State-of-the-Art light trapping nanostructures was introduced in detail. Then nanostructures were reviewed based on their anti-reflection and light trapping character in thin and thick silicon solar cell applications. The lab-scale and mass-scale status of high efficiency silicon solar devices was described with their integrated light trapping technologies.

In Chapter 4, A detailed description of the recipes for Front back (FB) and interdigitated back contact (IBC) solar cell devices was presented. I also presented a thorough characterization of solar cell devices both in the optical and in the electrical regime. I built my own setups for following measurement techniques: current-voltage characteristics, absorption and external quantum efficiency (EQE). The details given by the end of the chapter.

FB devices were developed in the course of this thesis and they were used to demonstrate the effects of light trapping in different types of nanostructure. A number of IBC devices was fabricated to develop a good recipe. While this recipe has been successfully used to make solar cells of competitive efficiency, it also provides a good template for future studies:

The main scope for improvement is the passivation technique used for lowering the recombination losses. As V_{oc} critically depends on recombination losses, a future student may want to work on passivation schemes to improve this parameter. As the doping concentration in the BSF and the FSF is critical for determining the V_{oc} of the final device, such a study may improve the passivation and yield higher efficiency devices. Since we have sputtering capability in our cleanroom, dielectric layers (Al_2O_3 and SiO_2 of various compositions may be tried. I assume that in addition to passivation, a separate study could be conducted whereby the resistivity of the metal material and the contact/silicon interface would be studied. Passivation and contacts optimization can significantly improve the efficiency, particularly in IBC solar cells.

In Chapter 5, the optimized fabrication of pyramids, wet and dry quasi-random nanostructures was presented together with their optical characterization.

I also presented a detailed electrical analysis of FB and IBC solar devices including doping profiles and passivation schemes. Later, the integration of light trapping structures integrated with solar cells was analysed in both in the optical and the electronic regime. I discussed how the open circuit voltage V_{oc} represents the recombination loss and the short circuit current J_{sc} the light trapping properties for a comparison of these structures.

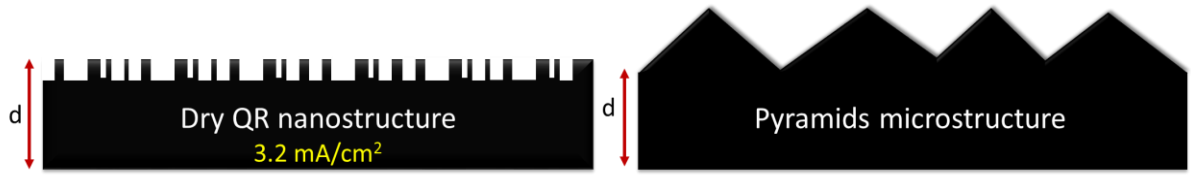

Figure 7.3. Short- circuit current (J_{sc}) improvement in a device integrated with QR nanostructures vs a device with pyramid microstructures.

The results of this study conclude that diffractive nanostructures have the potential to be used in wafer-based silicon technology. The fact that dry etched QR nanostructures perform better

than pyramid microstructures was surprising and it highlights the importance of efficient light trapping even for thick wafer-based devices.

In Chapter 6, I introduced halide perovskites as possible contenders for a tandem solar cell structure, together with silicon. Given that it was too difficult to construct high quality perovskite solar cells, I explored the optoelectronic properties of perovskites instead. The objectives achieved were as follows:

- Perovskite film fabrication methods were developed for a variety of parameters for thick or thin layers.
- Random lasing is observed in uniform perovskite films. Random lasing had not been reported before in uniform films so I investigated the phenomenon.
- A number of parameters were studied to distinguish random lasing from the general emission properties that had already been reported in the literature.
- A semi-quantitative analysis of random lasing was provided in the course of this thesis as a result.

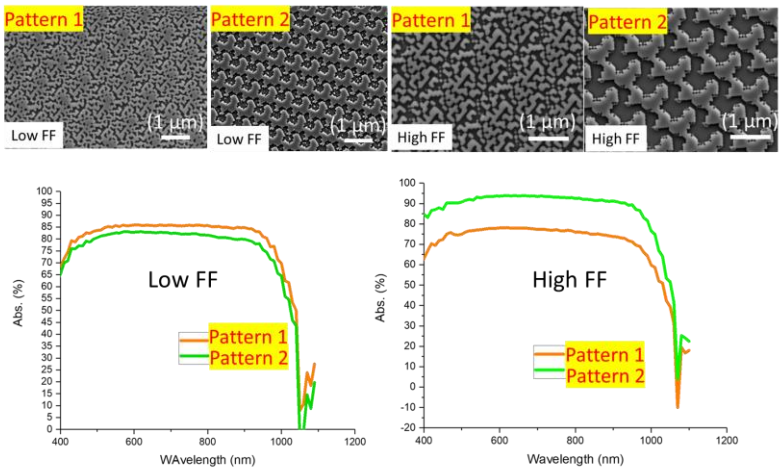

Figure 7.4. Two QR patterns patterns, i.e. Pattern 1 (32-bit) and Pattern 2 (16- bit) are shown in SEM images for low and high FF for a comparison of their corresponding absorption spectra.

The work presented in this thesis can be extended as a comparison between “black silicon” nanostructures and “quasirandom” nanostructures. Black silicon is a pronounced isotexture that provides excellent anti-reflection character based on its index gradient property. I have investigated the absorption properties of different QR patterns, as shown in Figure 4. Two QR patterns are shown in the SEM images where two etch times, i.e 30 sec and 90 sec were used to attain low and high fioll factors, respectively. This comparison highlights that the FF, together with the etch depth and feature size are important parameters which may significantly change the absorption properties. So, a detailed future simulation and experimentation study is required.

From the QR absorption spectrum in Figure 7.4, we assume that it has potential to compete with Black Silicon. By comparing these structures, it may be possible to understand which aspect of Black Silicon is responsible for its excellent AR Coating properties.

Overall, light trapping nanostructures can considerably improve the light absorption in silicon solar cells. The application of these structures results in a reduced absorber layer thickness, yet provides a high conversion efficiency. These are important considerations for reducing the cost of power generation from renewable energy sources. The application of QR light trapping structures on thin silicon (50 μm) substrates may be another interesting future study in the scope of this thesis. In terms of the tandem approach, future work aiming for high efficiency perovskite solar cells are an important requirement for realising such tandem geometries.

Chapter 7: Conclusion and outlook

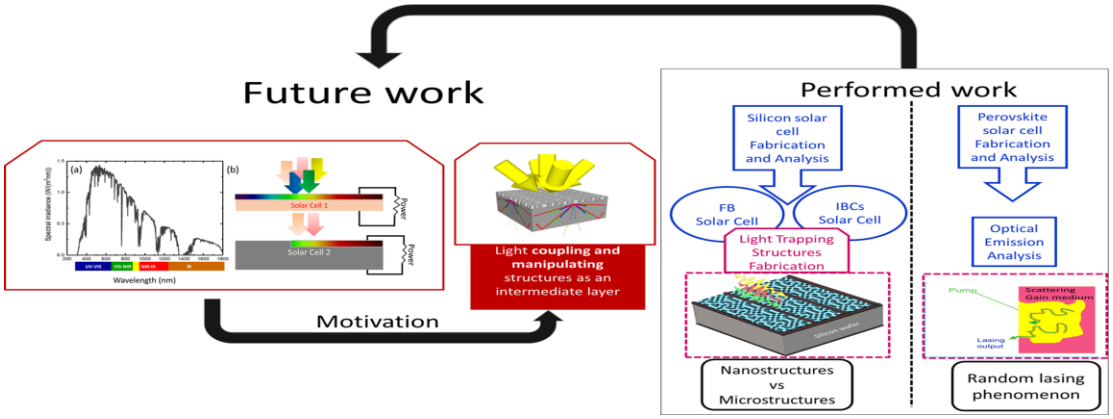

8 Bibliography

[1] M. Riordan, L. Hoddeson, *IEEE Spectr.* **1997**, *34*, 46.

[2] R. S. Ohl, *Light- Sensitive Electric Device Including Silicon*, **1948**.

[3] R. M. Swanson, *IEEE J. Photovoltaics* **2005**, *31*, 889.

[4] D. M. Chapin, C. S. Fuller, G. L. Pearson, *J. Appl. Phys.* **1954**, *25*, 29.

[5] P. Würfel, *Physics of Solar Cells: From Principles to New Concepts*, Wiley-VCH Verlag, **2005**.

[6] M. Suri, T. A. Huld, E. D. Dunlop, O. H.A, *Sol. Energy* **2007**, *81*, 1295.

[7] A. H. Almasoud, H. M. Gandayh, *J. King Saud Univ. - Eng. Sci.* **2015**, *27*, 153.

[8] N. Kazmi, in *FOSS4G Conf. Portland, Oregon USA.*, **2014**.

[9] P. Kubecka, *Weather* **2001**, *56*, 218.

[10] "http://rredc.nrel.gov/solar/spectra/am1.5/astmg173/astmg173.html," **n.d.**

[11] T. Ishii, R. Sato, S. Choi, Y. Chiba, A. Masud, *Jpn. J. Appl. Phys.* **2017**, *56*, 1.

[12] O. Semonin, J. Luther, M. Beard, *SPIE Newsroom* **2012**, 1.

[13] M. A. Green, M. J. Keevers, *Prog. Photovoltaics Res. Appl.* **1995**, *3*, 189.

[14] S. M. Sze, *Semiconductor Devices: Physics and Technology*, John Wiley & Sons, **2006**.

[15] A. Smets, J. Klaus, O. Isabella, S. R. Van, M. Zeman, *Solar Enrergy The Physics and Engineering of PV Conversion Technologies and Systems*, UIT Cambridge Ltd, **2016**.

[16] M. Ruff, M. Fick, R. Lindner, U. Rössler, R. Helbig, A. Physik, W. Erlangen, *J. Appl. Phys.* **1993**, *74*, 267.

[17] H. T. Nguyen, S. C. Baker-finch, D. Macdonald, *Appl. Phys. Lett.* **2014**, *104*, 88.

[18] Y. Wan, **2003**, pp. 1–4.

[19] M. Kerr, P. Campbell, A. Cuevas, *29th IEEE Photovolt. Spec. Conf.* **2002**, 438.

[20] A. Richter, S. W. Glunz, F. Werner, J. Schmidt, A. Cuevas, *Phys. Rev. B - Condens. Matter Mater. Phys.* **2012**, *86*, 1.

[21] A. A. Lopez, *Phys. Rev.* **1968**, *175*, 823.

[22] W. Shockley, W. T. Read, *Phys. Rev.* **1952**, *87*, 835.

[23] A. G. Aberle, S. W. Glunz, W. Warta, *J. Appl. Phys.* **1992**, *71*, 4422.

[24] A. G. Aberle, *Prog. Photovoltaics Res. Appl.* **2000**, *8*, 473.

[25] A. Smets, K. Jäger, O. Isabella, M. Zeman, in *Sol. Energy Phys. Eng. Photovolt. Conversion, Technol. Syst.*, UIT Cambridge Ltd, **2016**, pp. 136–137.

[26] A. Smets, K. Jäger, O. Isabella, R. Van Swaaij, M. Zeman, *Sol. Energy Phys. Eng. Photovolt. conversion, Technol. Syst.* **2016**, 111.

[27] F.-H. Chen, S. Pathreeker, J. Kaur, I. D. Hosein, *Opt. Express* **2016**, *24*, 419.

[28] R. Brendel, J. H. Werner, H. J. Queisser, *Sol. Energy Mater. Sol. Cells* **1996**, *41–42*, 419.

[29] S. C. Baker-finch, K. Mcintosh, *Prog. Photovolt Res. Appl.* **2012**, *15*, 659.

[30] A. Richter, M. Hermle, S. W. Glunz, *IEEE J. Photovoltaics* **2013**, *3*, 1184.

[31] T. Couteau, M. Carcasi, *Proc. SPIE* **2006**, *6153*, 1.

[32] H. W. Deckman, C. R. Wronski, H. Witzke, E. Yablonovitch, *Appl. Phys. Lett.* **1983**, *42*, DOI 10.1063/1.2336629.

[33] A. Goetzberger, in *15th Photovolt. Spec. Conf.*, **1981**, pp. 867–870.

[34] J. Cotter, *J. Appl. Phys.* **1998**, *84*, 618.

[35] J. E. Cotter, R. B. Hall, M. G. Mauk, A. M. Barnett, *Prog. Photovoltaics Res. Appl.* **1999**, *7*, 261.

[36] A. Lin, S. M. Fu, Y. K. Zhong, C. W. Tseng, P. Y. Chen, N. P. Ju, *J. Appl. Phys.* **2014**, *115*, DOI 10.1063/1.4872140.

[37] E. Yablonovitch, *J. Opt. Soc. Am.* **1982**, *72*, 899.

[38] T. Tiedje, E. Yablonovitch, G. D. Cody, B. G. Brooks, *IEEE Trans. Electron Devices* **1984**, *31*, 711.

[39] B. S. Eastwood, *"Francesco Maria Grimaldi," Dictionary of Scientific Biography*, New York: Charles Scribner And Sons, **1972**.

[40] P. Sheng, A. N. Bloch, R. S. Stepleman, *Appl. Phys. Lett.* **1983**, *43*, 579.

[41] B. P. Rand, J. Genoe, P. Heremans, J. Poortmans, *Prog. Photovolt Res. Appl.* **2007**, *15*, 659.

[42] F. Institute, *Photovoltaics Report:Annual Energy Outlook*, **2016**.

[43] P. Kowalczewski, L. C. Andreani, *Sol. Energy Mater. Sol. Cells* **2015**, *143*, 260.

[44] N. W. Ashcroft, N. D. Mermin, *Phys. unserer Zeit* **1978**, *9*, 33.

[45] R. A. Wind, M. A. Hines, *Surf. Sci.* **2000**, *460*, 21.

[46] B. Tang, M. Shikida, K. Sato, P. Pal, H. Amakawa, H. Hida, K. Fukuzawa, *J. Micromechanics Microengineering* **2010**, *20*, DOI 10.1088/0960-1317/20/6/065008.

[47] C. R. Yang, C. H. Yang, P. Y. Chen, *J. Micromechanics Microengineering* **2005**, *15*, 2028.

[48] B. P. Rand, J. Genoe, P. Heremans, J. Poortmans, *Prog. Photovolt Res. Appl.* **2007**, *15*, 659.

[49] J. Zhao, A. Wang, M. A. Green, F. Ferrazza, V. A. D. Andrea, *Appl. Phys. Lett.* **1998**, *73*, 1991.

[50] M. Halbwax, T. Sarnet, P. Delaporte, M. Sentis, H. Etienne, F. Torregrosa, V. Vervisch, I. Perichaud, S. Martinuzzi, *Thin Solid Films* **2008**, *516*, 6791.

[51] Y. Xia, B. Liu, J. Liu, Z. Shen, C. Li, *Sol. Energy* **2011**, *85*, 1574.

[52] K. M. Guenther, A. L. Baumann, T. Gimpel, S. Kontermann, W. Schade, *Energy Procedia* **2012**, *27*, 555.

[53] H. Savin, P. Repo, G. von Gastrow, P. Ortega, E. Calle, M. Garín, R. Alcubilla, *Nat. Nanotechnol.* **2015**, *10*, 1.

[54] P. Pathi, A. Peer, R. Biswas, *Nanomaterials* **2017**, *7*, 1.

[55] E. Garnett, P. Yang, *Nano Lett.* **2010**, *10*, 1082.

[56] A. Mavrokefalos, S. E. Han, S. Yerci, M. S. Branham, G. Chen, *Nano Lett.* **2012**, *12*,

2792.

[57] Z. Fan, R. Kapadia, P. W. Leu, X. Zhang, Y. L. Chueh, K. Takei, K. Yu, A. Jamshidi, A. A. Rathore, D. J. Ruebusch, M. Wu, A. Javey, *Nano Lett.* **2010**, *10*, 3823.

[58] Q. Lin, S. F. Leung, L. Lu, X. Chen, Z. Chen, H. Tang, W. Su, D. Li, Z. Fan, *ACS Nano* **2014**, *8*, 6484.

[59] K. X. Wang, Z. Yu, V. Liu, Y. Cui, S. Fan, *Nano Lett.* **2012**, *12*, 1616.

[60] S. W. Glunz, R. Preu, D. Biro, *Comprehensive Renewable Energy*, Elsevier, **2012**.

[61] Z. Shi, S. Wenham, J. Ji, *Conf. Rec. IEEE Photovolt. Spec. Conf.* **2009**, 001922.

[62] N. Horiuchi, S. Wenham, *Nat. Photonics* **2012**, *6*, 136.

[63] P. J. Cousins, D. D. Smith, H. C. Luan, J. Manning, T. D. Dennis, A. Waldhauer, K. E. Wilson, G. Harley, W. P. Mulligan, in *2010 35th IEEE Photovolt. Spec. Conf.*, **2010**, pp. 275–278.

[64] D. D. Smith, P. Cousins, S. Westerberg, R. D. Jesus-Tabajonda, G. Aniero, Y. C. Shen, *IEEE J. Photovoltaics* **2014**, *4*, 1465.

[65] P. Bronsveld, M. Stodolny, L. Duval, P. Manshanden, B. Geerligs, **2015**.

[66] M. F. Abdullah, M. A. Alghoul, H. Naser, N. Asim, S. Ahmadi, B. Yatim, K. Sopian, *Renew. Sustain. Energy Rev.* **2016**, *66*, 380.

[67] P. Corporation, *Panasonic Photovoltaic Module Achieves World Highest Energyconversion Efficiency of 23.8% at Research Level*, **2016**.

[68] M. A. Green, *IEEE Trans. Electron Devices* **1984**, *ED-31*, 671.

[69] J. Oh, H. C. Yuan, H. M. Branz, *Nat. Nanotechnol.* **2012**, *7*, 743.

[70] D. Ariza-Flores, J. S. Pérez-Huerta, Y. Kumar, A. Encinas, V. Agarwal, *Sol. Energy Mater. Sol. Cells* **2014**, *123*, 144.

[71] **n.d.**

[72] S. Zhong, B. Liu, Y. Xia, J. Liu, J. Liu, Z. Shen, Z. Xu, C. Li, *Energy Procedia* **2012**, *14*, 505.

[73] **2000**, pp. 1552–1555.

[74] J. S. Yoo, I. O. Parm, U. Gangopadhyay, K. Kim, S. K. Dhungel, D. Mangalaraj, J. Yi, *Sol. Energy Mater. Sol. Cells* **2006**, *90*, 3085.

[75] S. H. Zaidi, D. S. Ruby, J. M. Gee, *IEEE Trans. Electron Devices* **2001**, *48*, 1200.

[76] Y. Inomata, K. Fukui, K. Shirasawa, *Sol. Energy Mater. Sol. Cells* **1997**, *48*, 237.

[77] M. Algasinger, J. Paye, F. Werner, J. Schmidt, M. S. Brandt, M. Stutzmann, S. Koynov, *Adv. Energy Mater.* **2013**, *3*, 1068.

[78] G. Kumaravelu, M. M. Alkaisi, A. Bittar, D. Macdonald, J. Zhao, *Curr. Appl. Phys.* **2004**, *4*, 108.

[79] M. Otto, M. Kroll, T. Käsebier, R. Salzer, A. Tünnermann, R. B. Wehrspohn, *Appl. Phys. Lett.* **2012**, *100*, 1.

[80] Z. Huang, N. Geyer, P. Werner, J. de Boor, U. Gösele, *Adv. Mater.* **2011**, *23*, 285.

[81] J. Yoo, G. Yu, J. Yi, *Mater. Sci. Eng. B* **2009**, *159–160*, 333.

[82] Y. Chen, Z. Xu, M. R. Gartia, D. Whitlock, Y. Lian, G. L. Liu, *ACS Nano* **2011**, *5*, 8002.

[83] P. Repo, J. Benick, V. Vähänissi, J. Schön, G. von Gastrow, B. Steinhauser, M. C. Schubert, M. Hermle, H. Savin, *Energy Procedia* **2013**, *38*, 866.

[84] W. Kern, J. E. Soc, *J. Electrochem. Soc.* **1990**, *137*, 1887.

[85] B.Jayant Baliga, in *Foundamentals Power Semicond. Devices*, City University Of Hong Kong, **2010**, pp. 1–30.

[86] W. . Smith, *Foundations of Materials Sciences and Engineering*, McGraw Hill, **2004**.

[87] M. D. Lammert, R. J. Schwartz, *IEEE Trans. Electron Devices* **1977**, *24*, 334.

[88] J. Nijs, J. Szlufcik, *IEEE Trans. Electron Devices* **1999**, *46*, 1948.

[89] K. Masuko, M. Shigematsu, T. Hashiguchi, D. Fujishima, M. Kai, N. Yoshimura, T. Yamaguchi, Y. Ichihashi, T. Mishima, N. Matsubara, T. Yamanishi, T. Takahama, M. Taguchi, E. Maruyama, S. Okamoto, *IEEE J. Photovoltaics* **2014**, *4*, 1433.

[90] D. D. Smith, P. Cousins, S. Westerberg, R. De Jesus-tabajonda, G. Aniero, *Boron* **1999**, *4*, 1465.

[91] K. McIntosh, M. J. Cudzinovic, D. D. Smith, W. P. Mulligan, R. M. Swanson, in *World Conf. Photovolt. Energy Convers.*, **2003**, pp. 971–974.

[92] E. R. Martins, J. Li, Y. Liu, V. Depauw, Z. Chen, J. Zhou, T. F. Krauss, *Nat. Commun.* **2013**, *4*, 2665.

[93] M. Padilla, B. Michl, C. Reichel, N. Hagedorn, S. Kluska, S. T. Haag, R. Keding, A. Fell, M. Kasemann, W. Warta, M. C. Schubert, in *Eur. Photovolt. Sol. Energy Conf. Exhib.*, **n.d.**, pp. 1138–1142.

[94] E. R. Martins, J. Li, Y. Liu, J. Zhou, T. F. Krauss, *Phys. Rev. B - Condens. Matter Mater. Phys.* **2012**, *86*, 1.

[95] J. Li, K. Li, C. Schuster, R. Su, X. Wang, B. H. V Borges, T. F. Krauss, E. R. Martins, *Sci. Rep.* **2015**, *5*, 1.

[96] A. De Vos, *J. Phys. D. Appl. Phys.* **1980**, *13*, 839.

[97] A. Polman, M. Knight, E. C. Garnett, B. Ehrler, W. C. Sinke, *Science* **2016**, *352*, 307.

[98] A. Belghachi, in *Sol. Cells - New Approaches Rev.*, Intech, **2015**, pp. 47–76.

[99] L. Yalçin, R. Öztürk, *J. Optoelectron. Adv. Mater.* **2013**, *15*, 326.

[100] L. Protesescu, S. Yakunin, M. I. Bodnarchuk, F. Krieg, R. Caputo, C. H. Hendon, R. X. Yang, A. Walsh, M. V. Kovalenko, *Nano Lett.* **2015**, *15*, 3692.

[101] N. K. Noel, S. D. Stranks, A. Abate, C. Wehrenfennig, S. Guarnera, A. A. Haghighirad, A. Sadhanala, G. E. Eperon, S. K. Pathak, M. B. Johnston, A. Petrozza, L. M. Herz, H. J. Snaith, *Energy Environ. Sci.* **2014**, *7*, 3061.

[102] J. Fan, B. Jia, M. Gu, *Photonics Res.* **2014**, *2*, 111.

[103] C. C. Chen, S. H. Bae, W. H. Chang, Z. Hong, G. Li, Q. Chen, H. Zhou, Y. Yang, *Mater. Horiz.* **2015**, *2*, 203.

[104] C. H. Chiang, C. G. Wu, *Nat. Photonics* **2016**, *10*, 196.

[105] Y. Zhou, M. Yang, W. Wu, A. L. Vasiliev, K. Zhu, N. P. Padture, *J. Mater. Chem. A* **2015**, *3*, 8178.

[106] M. Sun, S. Wang, Y. Xiao, Z. Song, X. Li, *J. Energy Chem.* **2015**, *24*, 756.

[107] Z. Liang, J. Ding, S.-H. Zhang, X. Xu, N. Wang, J. Wang, X. Wang, Z. Bi, G. Xu, N. Yuan, *RSC Adv.* **2015**, *5*, 60562.

[108] M. Ledinsk, P. Loper, B. Niesen, J. Holovsky, S. J. Moon, J. H. Yum, S. De Wolf, A. Fejfar, C. Ballif, *J. Phys. Chem. Lett.* **2015**, *6*, 401.

[109] **n.d.**

[110] G. Tallents, *Phys. Today* **1956**, *9*, 44.

[111] Z. Tan, R. S. Moghaddam, M. L. Lai, P. Docampo, R. Higler, F. Deschler, M. Price, A. Sadhanala, L. M. Pazos, D. Credgington, F. Hanusch, T. Bein, H. J. Snaith, R. H. Friend, *Nat. Nanotechnol.* **2014**, *9*, 687.

[112] G. Xing, N. Mathews, S. S. Lim, N. Yantara, X. Liu, D. Sabba, M. Grätzel, S. Mhaisalkar, T. C. Sum, *Nat. Mater.* **2014**, *13*, 476.

[113] L. Etgar, P. Gao, Z. Xue, Q. Peng, A. K. Chandiran, B. Liu, *J. Am. Chem. Soc.* **2012**, *134*, 17396.

[114] J. Burschka, N. Pellet, S.-J. Moon, R. Humphry-Baker, P. Gao, M. K. Nazeeruddin, M. Grätzel, *Nature* **2013**, *499*, 316.

[115] C. Motta, F. El-Mellouhi, S. Sanvito, *Sci. Rep.* **2015**, *5*, 1.

[116] T. S. Kao, Y. H. Chou, C. H. Chou, F. C. Chen, T. C. Lu, *Appl. Phys. Lett.* **2014**, *105*, 231108.

[117] P. Docampo, T. Bein, *Acc. Chem. Res.* **2016**, *49*, 339.

[118] S. D. Stranks, H. J. Snaith, *Nat. Nanotechnol.* **2015**, *10*, 391.

[119] Y. Tian, A. Merdasa, E. Unger, M. Abdellah, K. Zheng, S. Mckibbin, A. Mikkelsen, T. Pullerits, A. Yartsev, V. Sundstro, I. G. Scheblykin, *J. Phys. Chem. Lett.* **2015**, *6*, 4171.

[120] S. Yakunin, L. Protesescu, F. Krieg, M. I. Bodnarchuk, G. Nedelcu, M. Humer, G. De Luca, M. Fiebig, W. Heiss, M. V Kovalenko, *Nat. Commun.* **2015**, *6*, 1.

[121] J. Xing, F. Yan, Y. Zhao, S. Chen, H. Yu, Q. Zhang, R. Zeng, H. V. Demir, X. Sun, A. Huan, Q. Xiong, *ACS Nano* **2016**, *10*, 6623.

[122] N. Yantara, S. Bhaumik, F. Yan, D. Sabba, H. A. Dewi, N. Mathews, P. P. Boix, H. V.

Demir, S. Mhaisalkar, *J. Phys. Chem. Lett.* **2015**, *6*, 4360.

[123] R. Dhanker, A. N. Brigeman, A. V Larsen, R. J. Stewart, J. B. Asbury, N. C. Giebink, *Appl. Phys. Lett.* **2014**, *105*, 1.

[124] F. Deschler, M. Price, S. Pathak, L. E. Klintberg, D. D. Jarausch, R. Higler, S. Hüttner, T. Leijtens, S. D. Stranks, H. J. Snaith, M. Atatüre, R. T. Phillips, R. H. Friend, *J. Phys. Chem. Lett.* **2014**, *5*, 1421.

[125] B. R. Sutherland, E. H. Sargent, *Nat. Photonics* **2016**, *10*, 295.

[126] Q. Zhang, S. T. Ha, X. Liu, T. C. Sum, Q. Xiong, *ACS Nano* **2014**, *14*, 5995.

[127] H. Zhu, Y. Fu, F. Meng, X. Wu, Z. Gong, Q. Ding, G. M. V., M. T. Tuan, J. Song, X.-Y. Zhu, *Nat. Mater.* **2015**, *14*, 636.

[128] T. C. Sum, A. Nurmikko, *ACS Nano* **2016**, *10*, 3959.

[129] G. L. W. Hitworth, R. J. HArwell, D. N. Miller, G. J. Hedley, W. Zhang, H. J. Snaith, A. T. Graham, I. D. W. Samuel, *Opt. Express* **2016**, *24*, 23677.

[130] G. L. Whitworth, J. R. Harwell, D. N. Miller, G. J. Hedley, W. Zhang, H. J. Snaith, G. A. Turnbull, I. D. W. Samuel, *Opt. Express* **2016**, *24*, 23677.

[131] S. A. Veldhuis, P. P. Boix, N. Yantara, M. Li, T. C. Sum, N. Mathews, S. G. Mhaisalkar, *Adv. Mater.* **2016**, *28*, 6804.

[132] M. Saliba, S. M. Wood, J. B. Patel, P. K. Nayak, J. Huang, J. A. Alexander-Webber, B. Wenger, S. D. Stranks, M. T. Hörantner, J. T. W. Wang, R. J. Nicholas, L. M. Herz, M. B. Johnston, S. M. Morris, H. J. Snaith, M. K. Riede, *Adv. Mater.* **2016**, *28*, 923.